Arctic Oceanic and Sea Ice Heat Fluxes from the CCSM versions 3 and 4

Louis Renaud-Desjardins

Atmospheric and Ocean Sciences

McGill University, Montréal, Québec

12 December 2019

A memoir submitted to McGill University in partial fulfillment of the requirements of the Master's degree.

Abstract

This thesis furthers the understanding of thermal interactions between the ocean and the sea ice using the Community Climate System Model (CCSM). It focuses on the results from the six simulations under the Special Report on Emissions Scenarios (SRES) A1B from the CCSM version 3 (CCSM3) and the five simulations under the Representative Concentration Pathways (RCP) 6.0 scenario from the CCSM version 4 (CCSM4). Rapid losses of September sea ice extent were simulated through all the A1B simulations from the CCSM3. A rapid loss event is recorded when the derivative of the five-year running mean of September sea ice extent is inferior to -0.5 million km^2 per year. These events are preceded by pulses of warm water toward the Arctic Ocean one to two years beforehand. The presented analysis includes all the physical processes affecting sea ice in connection with the years of rapid September sea ice extent loss. Every melt process increases until the years of rapid sea ice extent loss. At the same time, the sea ice formation processes stagnate and the sea ice transport through the gates of the Arctic Ocean decreases. Therefore, we conclude that the rapid losses of September sea ice extent are caused by increased melt – especially bottom melt. In the A1B simulations, the sea ice receives from the ocean 20 W/m^2 of heat in 1900 up to 120 W/m^2 in 2100. This is significantly more than the conventional 2 W/m^2 found in the literature. This important increase in heat transfer is caused by a combination of multiplicative of a significant increase in sea surface temperature and currents all over the Arctic Ocean. The heat sources causing the significant increase in sea surface temperature can be uncovered through a temperature-heat ocean budget. The temperature-heat ocean budget proved impossible to close satisfactorily. This was the case for both versions 3 and 4. In particular, for version 4 which has extended output variables, we found an error for the vertically integrated budget exceeding 50 W/m^2. Nevertheless, the study of advective heat transport through the gateways of the Arctic Ocean can provide insight on the warming of the Arctic Ocean and its impact on sea ice melt. The heat transport through the gateways of the Arctic Ocean is studied for both the CCSM versions 3 and 4. Both models forecast very different Arctic conditions. The CCSM3 advective heat transport is dominated by the heat fluxes through the Barents Sea Opening. Its total advective heat transfer to the Arctic

Ocean is positive, warming the Arctic Ocean, from 35 W/m^2 in 1900 up to 13 W/m^2 in 2100. The CCSM4 advective heat transport is not dominated by the advective heat flux from one of its gateways. Indeed, in this case, the heat transport gets important contributions from all the gateways. Its total advective heat transfer starts from 19 W/m^2 in 1900 up to 60 W/m^2 in 2100. The CCSM3 advective heat transfer is more than twice as important than the one simulated by the CCSM4.

Résumé

Cette thèse décrit les interactions thermodynamiques entre l'océan Arctique et sa glace de mer. Pour ce faire, les résultats des six simulations du *Community Climate System Model version 3* (CCSM3) soumises au futur scénario *Special Results on Emission Scenario* (SRES) A1B sont étudiés. Toutes ces simulations présentes des pertes abruptes de superficie de glace en septembre. Une perte de glace abrupte est enregistrée quand la dérivée de la moyenne mobile quinquennale de la superficie de glace en septembre est inférieure à -0.5 million de km^2 par année. Ces pertes abruptes sont précédées par des maximums de transport de chaleur océanique une ou deux années auparavent. L'analyse présentée ici considère tous les mécanismes physiques influençant la glace de mer en lien avec les années de perte abrupte de glace. La fonte de glace s'accentue jusqu'aux pertes abruptes de glace tandis que la création de glace stagne et que l'expulsion de glace diminue. La fonte de glace est donc responsable des pertes abruptes de superficie de glace. La fonte à la base de la glace est le procédé de fonte le plus important et est celui qui augmente le plus. En moyenne, l'océan transfère à la glace 20 W/m^2 de chaleur en 1900 et 120 W/m^2 en 2100. Ces flux de chaleur sont considérablement plus élevés que ceux habituellement mentionnée dans la littérature de 2 W/m^2. Cette hausse de transfert thermique est générée par la hausse exponentielle de la température de surface de l'océan Arctique. Les sources de chaleur qui influencent la température de surface de l'océan Arctique peuvent être étudiées en complétant un bilan de chaleur océanique. Dans cette thèse, nous argumentons que ce bilan ne peut pas être complété sans une erreur substantielle de 50 W/m^2 même en utilisant des variables manquantes grâce aux résultats du CCSM4. Néanmoins, l'étude des flux de chaleur advectifs à travers les divers accès à l'océan Arctique est possible et permet d'identifier leurs impacts sur l'océan Arctique et sa glace de mer. Cinq simulations du CCSM4 sous le scénario *Representative Concentration Pathways* (RCP) 6.0 sont ajoutées aux six simulations précédemment nommées pour cette analyse. Pour le CCSM3, le flux de chaleur total à l'océan Arctique est dominé par le flux passant par l'ouverture de la mer de Barents. Le flux de chaleur advectif total augmente la température océanique de l'Arctique à force de 35 W/m^2 en 1900 et 130 W/m^2 en 2100. Pour le CCSM4, les flux de chaleur advectifs passant par toutes les voies d'accès sont importants. Le flux de

chaleur total du CCSM4 réchauffe l'océan Arctique à force de 19 W/m^2 en 1900 et 60 W/m^2 en 2100. Le CCSM3 prévoit un réchauffement océanique, causé par les flux advectifs de chaleur, deux fois plus important que ceux du CCSM4.

Table of Abbreviations

CCSM	Community Climate System Model
GCM	Global Climate Model
GFDL	Geophysical Fluid Dynamics Laboratory
IMB	Ice-Mass-Balance
NSIDC	National Sea & Ice Data Center
RCP	Representative Concentration Pathway
SHEBA	Surface HEat Budget of the Arctic
SIA	Sea Ice Area
SIE	Sea Ice Extent
SIV	Sea Ice Volume
SIVT	Sea Ice Volume Transport
SRES	Special Report on Emission Scenario
	A1B the reasonable scenario
	B1 the optimistic scenario
	A2 the pessimistic scenario

Contribution of Authors

Data analysis and presentation of results are Louis' own work. Bruno Tremblay provided guidance.

Statement of Originality

The following elements of the thesis show original scholarship and represent distinct contributions to knowledge:

- Holland et al. (2006a) observed rapid loss of September sea ice extent in all of the CCSM3 SRES A1B simulations. They notice that the ocean heat transport to the Arctic precedes the mean Arctic sea ice thickness by two years. The work presented in chapter 3, investigates the role of all the sources of melt, growth and transport for the CCSM3 simulations under the SRES A1B. Holland et al. (2010) analyzed the total melt, total growth and total transport of several GCMs and reanalysis including the CCSM3. This thesis distinguishes (1) the total melt from its locations (bottom, top and lateral), (2) the sea ice creation from its two processes (basal and frazil), (3) the sea ice transport through the gates of the Arctic Ocean (the Fram Strait, the Barents Sea Opening, the CAA and the Bering Strait). This level of analysis has never been done before. The ocean heat transport considered in Holland et al. (2006a) includes all heat transport at 55° North. The region north of the 55^{th} parallel encloses more than just the Arctic. This thesis works with a region enclosing the Arctic Ocean tightly in the hope of a better correlation between the heat transport and the sea ice. In addition, inspired by the work of Winton (2011) which observed linear trends between the Arctic sea ice extent and the global temperature in the GFDL simulations, a decreasing exponential relationship between the sea ice volume and the extra forcing from the SRES A1B scenario is presented.

- Chapter 4 began as a study of vertical heat fluxes of the CCSM3 simulations. Since the vertical diffusion is not part of the standard output, Professor Bruno Tremblay hired an NCAR employee, Laura Landrum, to provide a code calculating vertical heat diffusion as a residual of the temperature-heat equation. This work was accomplished with the help of Marika Holland. The code was finished when I started my PhD. I decided to test it by using all the heat components included and tried to reconstruct the temperature-heat equation. This work proved to be more complicated than I antic-

ipated. Reconstructing the temperature-heat equation became the subject of chapter 4 and the appendices of this thesis. While the reconstruction of the temperature/heat equation is not original in itself - it is already known that the CCSM solves it -, it is an important tool to possess. With a complete and closing temperature-heat budget, any study of oceanic heat fluxes can be exact. Without it, there is always the possibility of a miscalculation or misinterpretation of some of the terms. No indications on how it should be done are published. Many scholars I met would have greatly appreciated the presence of such a tool for their own research.

- Despite the inconclusive results of chapter 4, I analyzed the heat transport through the gateways of the Arctic Ocean of the CCSM versions 3 and 4. The location of the gateways is based on the region enclosing the Arctic Ocean tightly introduced in the first paragraph. Woodgate et al. (2010) showed that the heat transport through the Bering Strait has an important impact on the sea ice thickness and cover in the proximity of the strait using observations. Even though the heat transports have a notable impact on the Arctic sea ice, they are not thoroughly studied utilizing GCMs results. Chapter 5 tackles the neglect of the model community toward the heat transport through the gateways of the Arctic Ocean.

Contents

List of Figures

List of Tables

1 Introduction

The Arctic is undergoing a rapid and critical transformation (Thomas, 2016). Sea ice has been decreasing both in extent and thickness since 1979 (Overland and Wang, 2013). That year was in fact the first year sea ice extent and thickness were recorded. Since then, the Arctic has lost 50% of its sea ice extent and 75% of its sea ice volume and this is showing no signs of slowing. All wildlife living on sea ice must adapt causing a major mutation of the ecosystems (Pfirman and Tremblay, 2009; Laidre et al., 2008). The marine ecosystems are also adjusting to the new warmer waters entering the Arctic Ocean (Beszczynska-Moller et al., 2011; Wassmann et al., 2011). The Inuit infrastructure and health are vulnerable to climate changes. Harvesting is now more dangerous and access to hunting areas is increasingly difficult (Ford et al., 2006; Ford, 2009). There is also the threat of permafrost melt releasing trapped green house gases enhancing global warming (Schaefer et al., 2012). On the other hand, the melt of sea ice is opening new, quicker, marine routes (Johannessen et al., 2000). Those new routes could lead to a decrease in fuel consumption in comparison with the usual longer paths which can be seen as a positive aspect of sea ice melt.

Holland et al. (2006a) presented the results of six simulations under the Special Report on Emission Scenario (SRES) A1B from the Community Climate System Model version 3 (CCSM3). The simulations are characterized by a summer ice-free Arctic Ocean as early as 2040 preceded by a rapid loss of September sea ice extent. Holland et al. (2006a) hypothesize that the ocean could precondition the rapid loss of sea ice after observing a pulse of warm water entering the Arctic Ocean one or two years prior the rapid losses. The goals of this thesis are: (1) to characterize the exchanges of heat between the sea ice and ocean, (2) to assess their impact on the rapid sea ice losses, (3) to understand what drives the heat exchanges between the ocean and the sea ice. The ocean heat transfer to the sea ice has been theorized to be between 2 and $4\,W/m^2$ constant throughout the year (Maykut and Untersteiner, 1971). Measurements showed that the thermal interactions between the ocean and the sea ice follow a seasonal cycle and that there are large spatial differences (McPhee and Untersteiner, 1982; McPhee et al., 2003; Perovich et al., 1989; Perovich and Elder, 2002).

This thesis offers a thorough description of the oceanic and sea ice heat fluxes in the

Arctic. More specifically, we focus on the six simulations of the CCSM3 under the SRES A1B presented in Holland et al. (2006a). In chapter 2, we present a literature review of the Arctic Ocean and its sea ice. For the Arctic Ocean, its geography, bathymetry, circulation and temperature-salinity profile are described. How sea ice is measured is presented along the concept of sea ice extent, sea ice area, sea ice thickness and sea ice volume. The sea ice is subject to positive and negative feedback. The most notable ones are presented in this chapter. Since we extensively study the results from the CCSM versions 3 and 4, we judged necessary to introduce the equations and the grids of the ocean and sea-ice components of the CCSM. In chapter 3, we investigate all the processes affecting the sea ice. We want to compare the relative strength of the oceanic heat flux and others. We also want to explore the different variables behind the ocean to sea ice heat flux. In chapter 4, we scrutinize all the ocean heat fluxes by investigating the ocean temperature-heat budget. It should give insight on the different ocean variables affecting the exchanges of heat between the ocean and the sea ice. Finally, in chapter 5, we study the ocean advective heat fluxes through the gateways of the Arctic Ocean for both the CCSM version 3 and version 4. The gateways include Fram Strait, Barents Sea Opening, the Canadian Arctic Archipelago, Bering Strait. This analysis gives an understanding of the oceanic heat fluxes impact on the Arctic scale.

2 The Arctic

This chapter introduces the basic notions used by the scientific community to characterise the Arctic Ocean. The covered concepts include (1) a definition of the Arctic, (2) a definition of the Arctic Ocean, circulation of the Arctic Ocean, temperature and salinity profile of the Arctic Ocean and its halocline in section 2.1, (3) a definition of sea ice, sea ice concentration measured by satellites, definition of sea ice extent and sea ice thickness measurements in section 2.2, (4) Arctic sea ice feedbacks in section 2.3, (5) ocean modelling, sea ice modelling and future projection forcing in section 2.4. While the present introduction is succinct, the curious reader is invited to read the references.

The Arctic is widely understood as the northern region of planet Earth. It comes from the Greek word *arktitos* which means *near the Bear* or *northern* referring to the Ursa constellations and Polaris, the North Star. The Arctic has two scientific definitions: (1) everything north of the polar circle and (2) where the average temperature of the warmest month, July, is below $10°C$ [1]. Both Arctic definitions are shown in figure 2.1. The polar circle marks the northernmost point at which the noon sun is barely visible on the winter solstice - no daylight - and southernmost point at which the midnight sun is barely visible on a summer solstice - no night time. A winter solstice occurs the day with the least sunlight while the summer solstice occurs the day with the most sunlight. The polar circle changes due to planet Earth axial tilt oscillation between 22.1° and 24.5° over 40 000 years. Right now the polar circle is moving northward at around $15\,m/y$. The second definition follows the tree line, the line separating where trees can still grow and where they cannot grow (Smithson et al., 2002). By that definition, the Arctic is the region where no trees can grow. It is bound to decrease with global warming.

[1] NSIDC, *https://nsidc.org/cryosphere/arctic-meteorology/arctic.html, last visited December 2017*

Figure 2.1: The two definitions of the Arctic domain: 1) by the polar circle in dashed blues, and 2) by the $10°C$ July average isotherm. This map was contributed by the United States Central Intelligence Agency, published in 2002. The map can be retrieve at the Library of Congress Geography and Map Division, Washington, D.C. or at the web site *https://www.loc.gov/resource/g3270.ct001717/*.

2.1 Arctic Ocean

The Arctic Ocean is bordered by land from the United States (Alaska), Canada (Canadian Arctic Archipelago or CAA), Finland, Denmark (Greenland), Iceland, Norway (Svalbard), Russia and Sweden, as can be seen in figure 2.1 or 2.2. It is composed of two major basins:

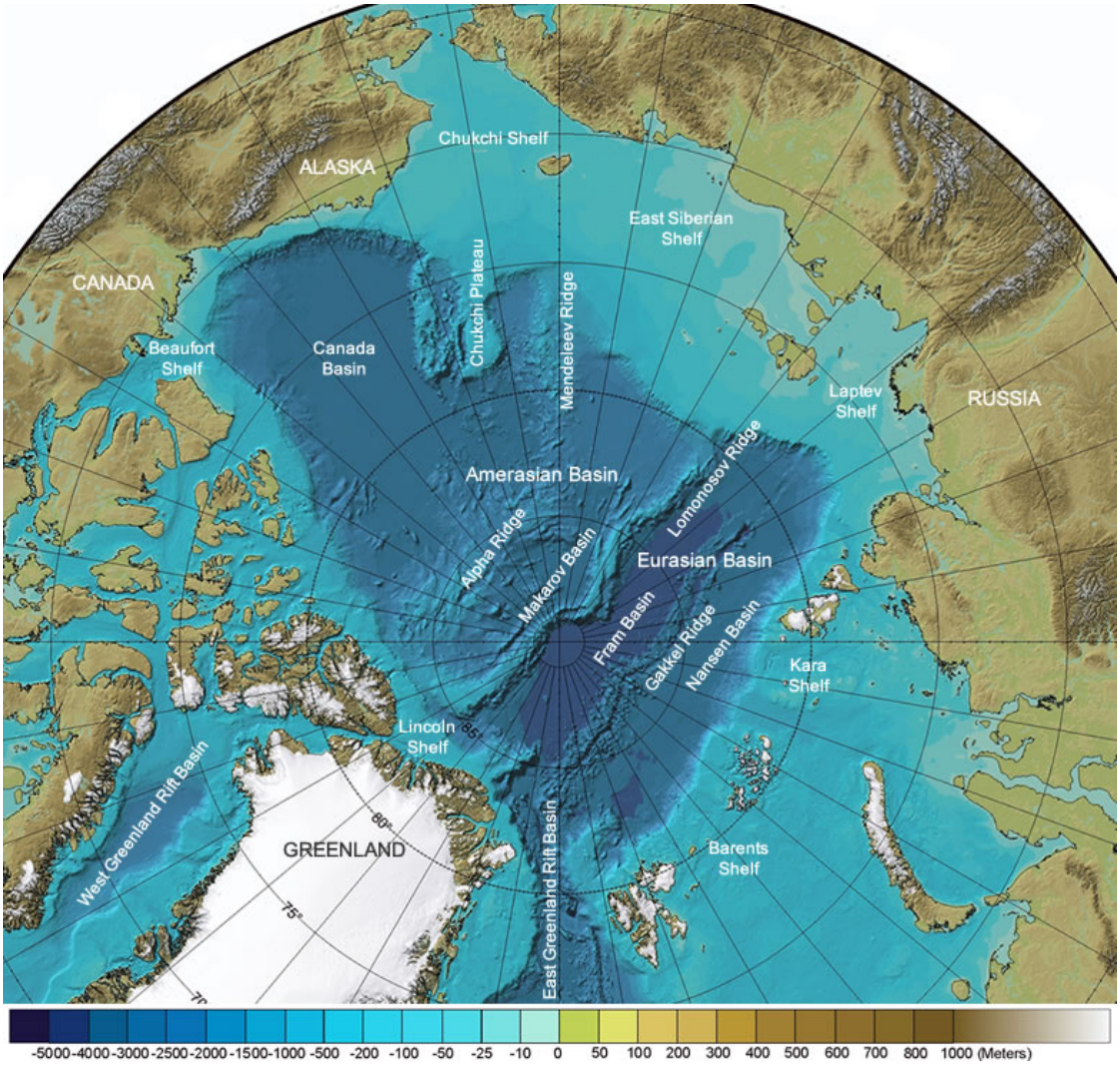

Figure 2.2: International Bathymetric Chart of the Arctic Ocean annotated with the names of basins, ridges and shelves (Jakobsson et al., 2012).

the Eurasian basin northeast of Greenland and the Amerasian basin northwest of Greenland divided by the Lomonosov Ridge. The Eurasian Basin is composed of the Amundsen or Fram Basin and the Nansen Basin. They are separated by the Gakkel Ridge. The Amerasian Basin is composed of the Beauford Basin and the Makarov basin that are divided by the Alpha ridge. Seven seas share the Arctic Ocean: the Greenland sea that lies east of Greenland, the Beaufort Sea between Canada and Alaska and fives seas that border Russia. From east to west they are the Barents Sea, Kara Sea, Laptev Sea, East Siberian Sea and the Chukchi Sea which also borders Alaska. The Arctic Ocean has the highest ratio by far of continental shelf area over ocean area with a ratio of one third, making it unique. The mean depth of the Arctic Ocean is about one kilometre with a maximum depth of 5.5 km.

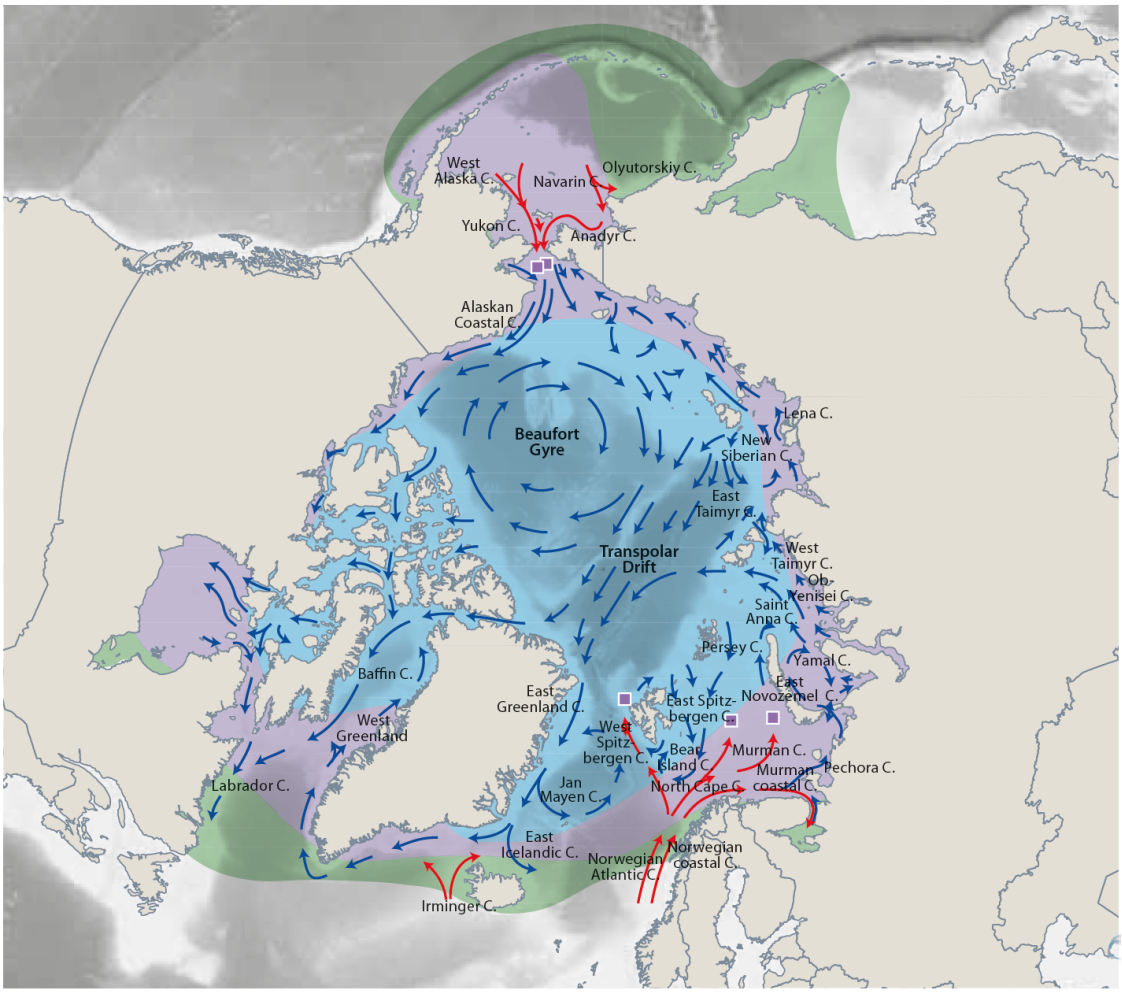

Figure 2.3: Circulation map of the Arctic Ocean. Red arrows show warm currents and blue arrows cold currents. The green region is for the Sub-Arctic, the purple region is for the Low Arctic and the blue region is for the High Arctic (AMAP, 2013).

The Arctic Ocean circulation is depicted in figure 2.3. Warm Atlantic waters enter the Arctic Ocean by the West Spitzbergen current west of Svalbard and by the North Cape current in the Barents Sea. The Atlantic waters are heavier than the Arctic Ocean surface waters being saltier though warmer. They sink and turn counterclockwise at the edge of the Arctic Ocean. The Pacific waters enter the Chukchi Sea through the Bering Strait and follow the Alaskan and Canadian coast into the Canadian Arctic Archipelago. The interior of the Amerasian Basin is dominated by the Beaufort Gyre turning clockwise. The transpolar drift takes waters through the Arctic Ocean following the Lomonosov Ridge through the Fram Basin exiting the Arctic Ocean as the East Greenland current through the Fram Strait.

The vertical temperature-salinity structure of the Arctic Ocean exhibits the presence of a cold halocline layer, see figure 2.4. The observed temperature-salinity profile is constant at

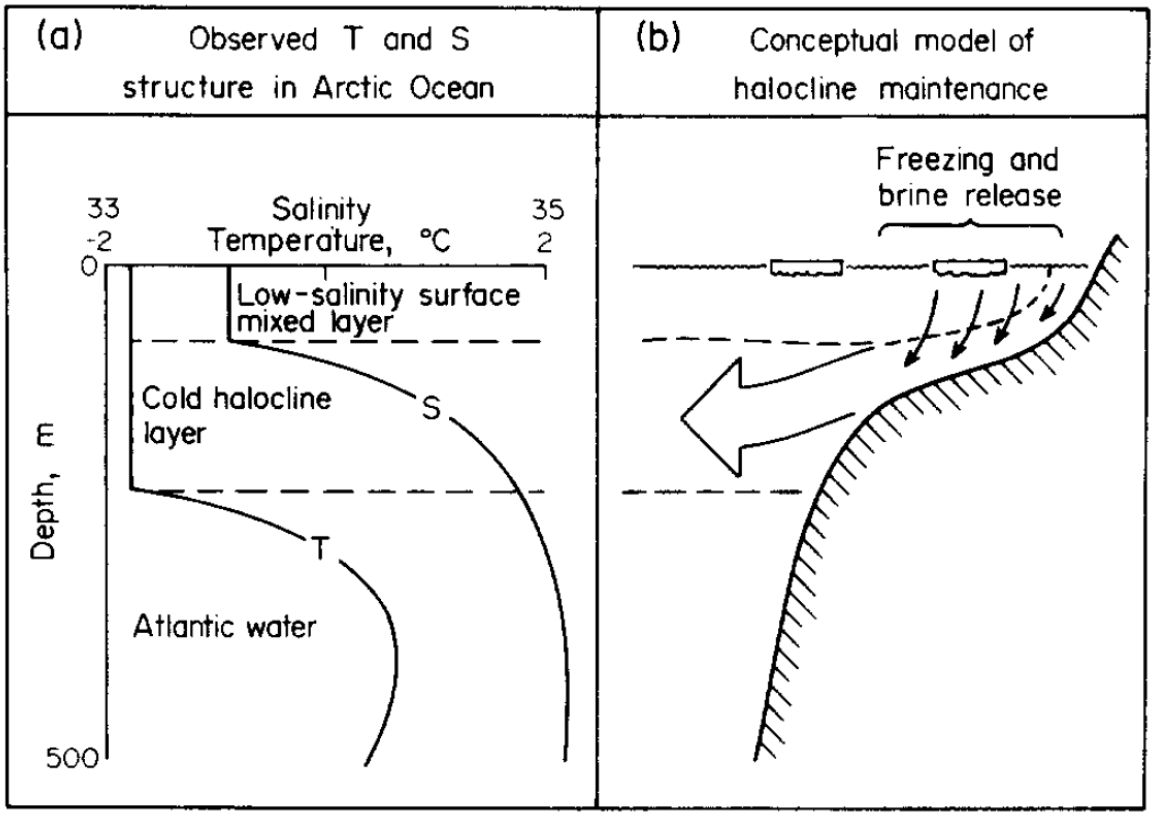

Figure 2.4: Schematic representation of the temperature and salinity structure in the upper Arctic Ocean and its maintenance. Taken from Aagaard et al. (1981).

$-1.8°C$ and 33.5 PSU over the first 50 meters. This continuity arises from mechanical surface forcings such as wind or ice motion causing turmoil and mixing over the first 50 meters. It is called the surface mixed layer. Between 50 and 200 metres, the ocean temperature stays at freezing point but the salinity increases. This vertical region is the halocline layer. The increased salinity makes the water denser, stabilizing the water column which diminishes the vertical mixing insulating the sea ice from the warm Atlantic waters between 200 and 500 metres at $1°C$ and 35 PSU (Steele and Boyd, 1998). Aagaard et al. (1981) showed that the halocline is created by the salt rejection during ice formation. This salt rejection increases the salinity of cold already saline surface waters causing its density to increase and sink between 50 and 200 metres.

2.2 Sea ice

Ice formed from sea water contains salt therefore sea ice is a complex material. In this section, a brief introduction of sea ice as a material is presented. Section 2.2.1 defines sea ice extent

and presents measurements of it. Section 2.2.2 presents sea ice thickness measurements.

Sea ice is a mixture of freshwater solid ice crystals and interstitial liquid salty brine (Petrich and Eicken, 2010). Brine trapped in sea ice can escape and reach the ocean by five processes: initial salt rejection, salt diffusion, brine expulsion, gravity drainage and flushing. Notz and Worster (2009) explored all five options using analytical solutions from a mushy layer (Feltham et al., 2006), numerical solutions from a one-dimensional enthalpy model (Notz and Grae Worster, 2006) and observations (Shirtcliffe et al., 1991; Notz, 2005). They found that only gravity drainage during winter and flushing during summer contributed to salt rejection. During winter, as the sea ice surface temperature decreases, the interstitial liquid brine becomes denser creating a brine-density unstable profile. This heavier brine will push down resulting in convection replacing salty sea ice brine by ocean water. The flushing happens in summer when the ice becomes permeable. Golden et al. (1998) found that the ice becomes permeable at a brine volume fraction of 5%, temperature of $-5°C$ and salinity of 5 parts per thousand. This is known as the law of fives. When the sea ice becomes permeable, all water inside and over the ice is flushed down into the ocean leaving the ice brine free.

The Arctic Ocean is covered by sea ice. Sea ice concentration (SIC) is measured by satellite equipped with a microwave radiometer (Markus et al., 2012). The radiometer records the intensity (or brightness temperature T_B) of electromagnetic radiation for a specified frequency ν. The brightness temperature is given by

$$T_B = \epsilon T_S e^{-\tau} + \int_0^\tau T(z)\zeta(z)e^{-\tau+\tau'(z)}d\tau' + (1-\epsilon)\kappa e^{-\tau}\int_0^\tau T(z)\zeta(z)e^{-\tau'(z)}d\tau'(z), \qquad (2.1)$$

where ϵ is the emissivity of the surface, T_S is the surface temperature, τ is the atmospheric opacity from the surface to the satellite, $T(z)$ is the temperature at height z, $\zeta(z)$ is the emittance at height z, $\tau'(z)$ is the atmospheric opacity from the surface to height z, κ is an estimate of the diffusiveness of the surface reflection. The first term of the right-hand side of the equation is the surface emission for frequency ν reaching the satellite which is often the dominant source. The second term is the emission from the atmospheric column reaching the satellite. The third term represents the downwelling atmospheric column radiation reflected at the surface and travelling back up to the satellite. For a studied region, the brightness

temperature can be rewritten as the linear sum of ice emission and ocean emission,

$$T_B = T_O C_O + T_I C_I, \tag{2.2}$$

where T_O is the brightness temperature of the ocean, C_O is the fraction of the region covered by ocean, T_I is the brightness temperature of the ice, C_I is the fraction of the region covered by sea ice or sea ice concentration. The studied region is covered by ocean and sea ice only. Therefore, $C_O + C_I = 1$. Using this equality, we can rewrite the the last equation as

$$C_I = \frac{T_B - T_O}{T_I - T_O}. \tag{2.3}$$

Measuring T_B, T_O and T_I is challenging since all the terms depends on surface temperature, atmospheric opacities and emissivity. To do so, one usually analyze three different frequencies. During winter or when the weather is dry, changes in emissivity and surface temperature can be taken into account effectively leaving only a 5%[2] error on the sea ice concentration under optimal conditions. When the ice is scattered, the many types of surfaces - ocean, snow, first year ice, older ice - over the studied region increases the error up to 15%. During summer time, the emissivity of snow and ice is unpredictable and melt ponds are seen as ocean resulting in an error that can reach 25%. The error can be higher than 25% during severe storms and harsh weather. At the time of writing this thesis, the interior of the Arctic Ocean is still covered by highly concentrated sea ice allowing a satisfying level of confidence in satellite measurements. The National Snow and Ice Data Center (NSIDC) provides the satellite observations for the sea ice concentration.

2.2.1 Sea ice extent

To quantify how sea ice evolves, Arctic scientists prefers to study sea ice extent (SIE) over sea ice area (SIA). Sea ice extent is defined as the sum of all the studied region or grid cell area with more than 15% sea ice concentration while the sea ice area is the product of sea ice concentration and area. The value of 15% has been chosen based on the seven measures of

[2]The uncertainties on sea ice extent are provided by the National Snow and Ice Data Center (NSIDC). https://nsidc.org/data/amsre/data-quality/data-uncertainty.html,verifiedOctober2019

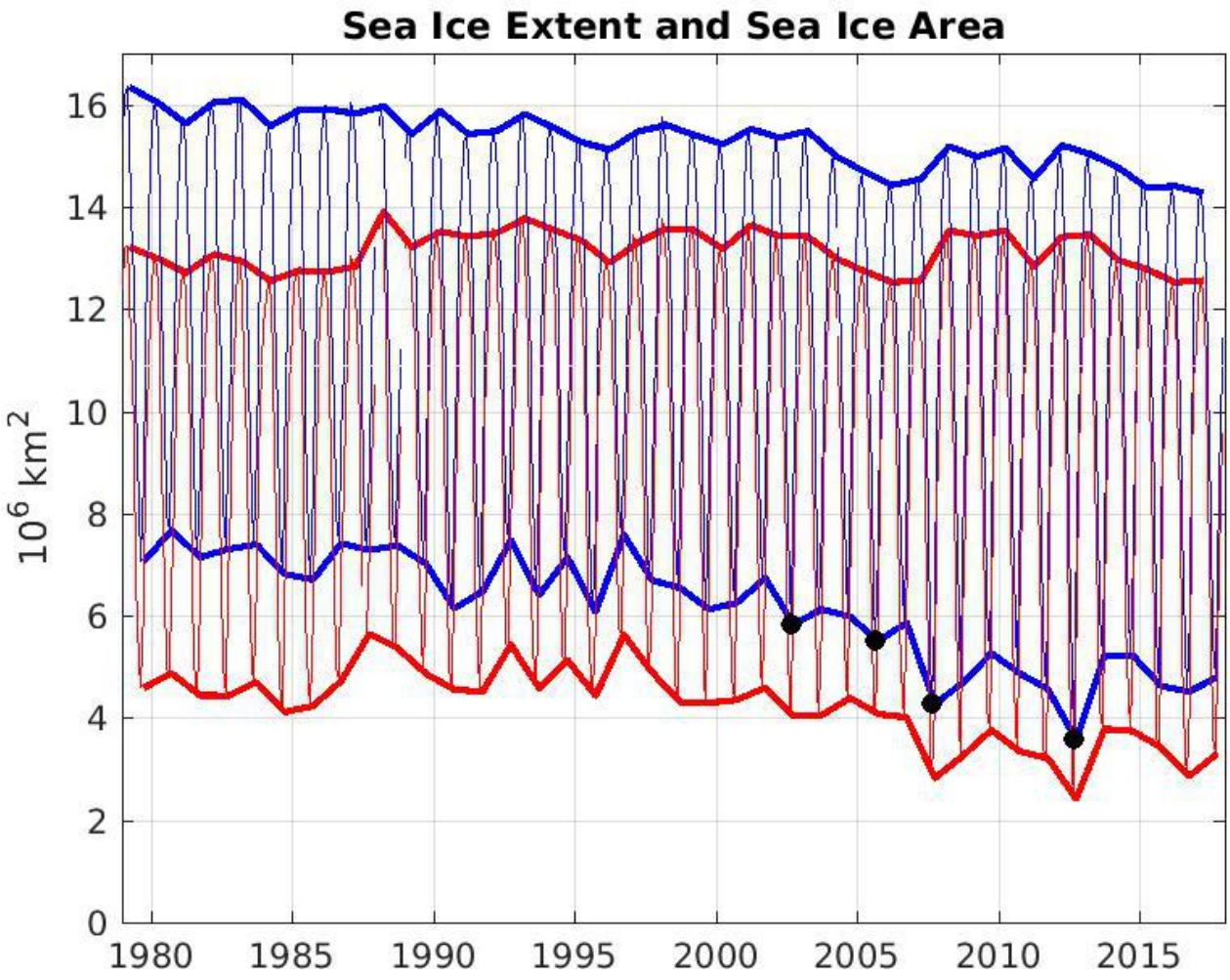

Figure 2.5: Sea ice extent in blue and sea ice area in red. Both curves are bound by their maximum or March area and minimum or September area. The four black dots display the four sea ice extent minima, 2002, 2005, 2007 and 2012. Data provided by the NSIDC (Fetterer et al., 2017).

ice-edge features by aircraft carrier reported in Cavalieri et al. (1991). They measured 11%, 20%, 20%, 13%, 15%, 15%, 15% sea ice concentration which averages at 15%. Studying sea ice extent is useful during summer where the surface melt and melt ponds appear as water even if sea ice is still present under a thin liquid layer. Because sea ice extent does not discard those regions unlike sea ice area, it gives a more reliable measurement of the total coverage of Arctic sea ice. Sea ice extent always covers a larger area than sea ice area, see figure 2.5. The four black dots display the four sea ice extent minimums of the 21^{st} century: 2002 (Serreze et al., 2003), 2005, 2007(Stroeve et al., 2008) and 2012 (Parkinson and Comiso, 2013).

2.2.2 Sea ice thickness

Sea ice thickness can be measured from different methods: (1) Upward Looking Sonar (ULS), (2) ElectroMagnetic (EM) sounding, (3) satellites or (4) direct measurement. The ULS can be attached to a submarine or moored on the sea bed. It calculates its own depth from the ambiant pressure and the distance to ice from sonar reflection on the ice base (Fissel et al., 2004). The EM sounding device - called an EM bird - is towed by a helicopter and measures its distance to the sea ice by a laser altimeter and its distance to the ocean using a frequency unaffected by sea ice (Haas et al., 2009). The resulting ice thickness has an error of $\pm 0.1\,m$. The main satellites investigating sea ice are CRYOsat and ICESat. CRYOsat is developed by the European Space Agency (ESA) and ICESat by the NASA (United States of America). They both calculate the distance from the first solid or liquid surface to the satellite, respectively Laxon et al. (2013) and Zwally et al. (2002). By using sea surface height measurement from the satellite, it is possible to transform the sea ice height in sea ice thickness. Lindsay and Schweiger (2015) combined the results from ULS, EM sounding and satellites. They found that most measurements were in acceptable agreement. The annual mean sea ice thickness between 2000 and 2012 is roughly about 5 metres at the Northern part of Canada and decreases toward Russia down to one metre. They also found a rapid decrease in ice thickness. From 2000 to 2012, the yearly averaged ice thickness has declined by $0.58 \pm 0.07\,m/decade$ which represents a loss of 34% while the September thickness declined by 50%. Using data from 1975 to 2012, the yearly averaged thickness decreased by 65% and the September thickness by 85%.

The worrying decay of ice in the Arctic inspired Andy Lee Robinson from Climate State to plot the dramatic Arctic Death Spiral, see figure 2.6. It shows the decrease in monthly mean Arctic sea ice volume for each month from 1979 to 2017. Every month, approximately $15 \cdot 10^3 km^3$ of sea ice volume is lost over the time span. The Pan-Arctic Ice Ocean Modelling and Assimilation System (PIOMAS) provided the data. It consists of a coupled ocean-ice climate model. The ocean part is the Parallel Ocean Program (POP) model developed at Los Alamos (Smith et al., 2010). The ice model is a thickness-enthalpy distribution (TED) sea ice model using viscous plastic rheology (Zhang and Rothrock, 2003). The atmospheric forcing

is derived from NCEP-NCAR reanalysis (Kalnay et al., 1996). PIOMAS showed reasonable agreement with observations.

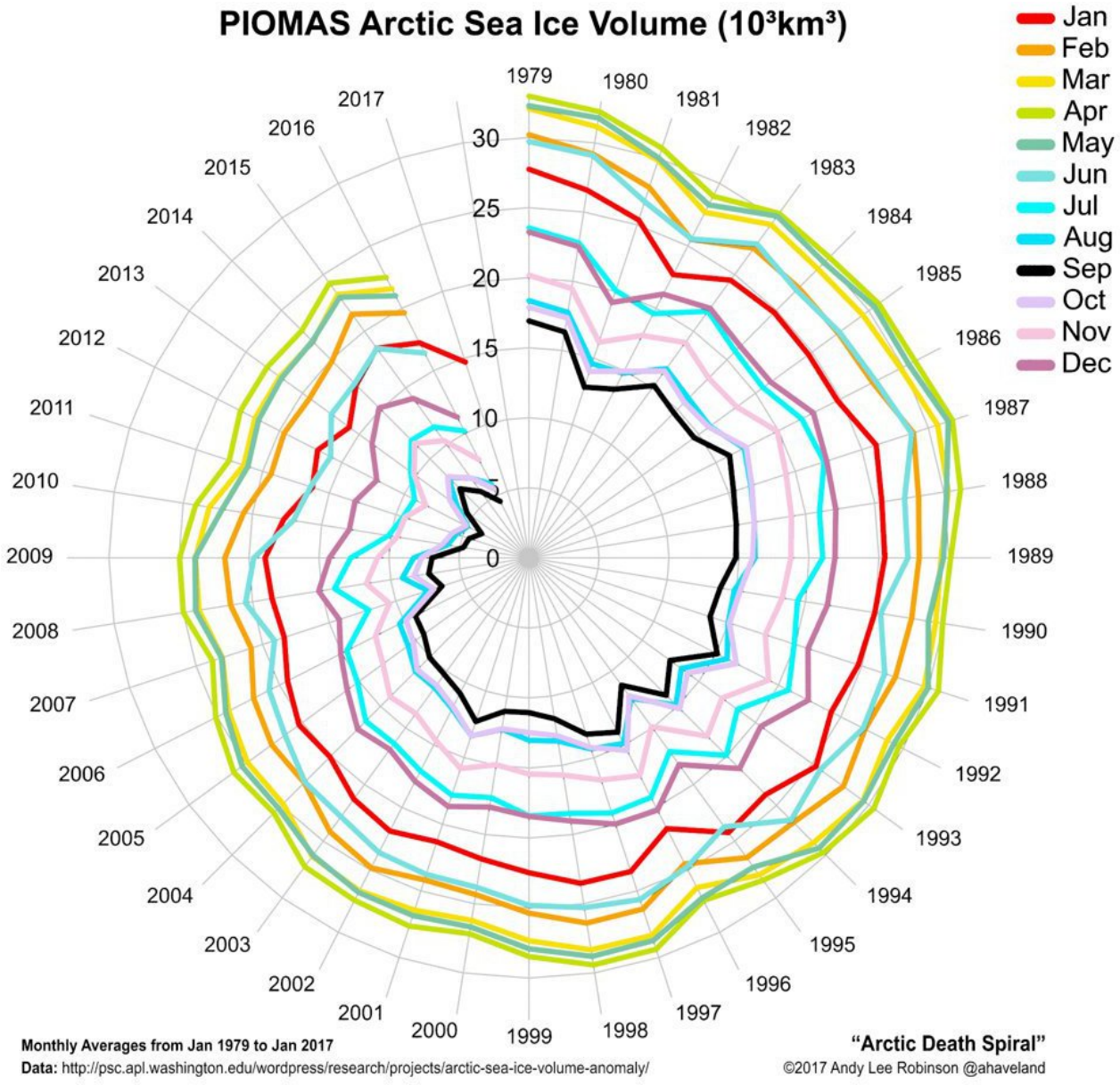

Figure 2.6: Arctic death spiral showing the evolution for each monthly sea ice volume between 1979 and 2017.

2.3 Feedback

The Arctic reacts more than the rest of the world to global warming because of overwhelming positive feedback processes (ACIA, 2005; Holland and Bitz, 2003). A positive feedback

happens when a change in a system amplifies itself. For example, sea ice loss brings more sea ice loss. A negative feedback happens when a change in a system erodes itself. Four of the most important feedback are presented in this section: the ice-albedo feedback, thinner ice feedback, cloud-ice feedback and the thermohaline feedback.

The ice-albedo feedback is the most important feedback. Sea ice is highly reflective to shortwave solar radiation whereas ocean is a good absorber of solar radiation. The albedo or reflectivity of ocean water is 0.1, between $0.3 - 0.4$ for land ice, between $0.5 - 0.7$ for sea ice and between $0.75 - 0.95$ for snow (Ahrens, 2009; NSIDC, 2013). If the area of open water increases, the total absorption of solar radiation by the Arctic Ocean will be higher. This energy will lead to an increase in ocean surface temperature. A warmer ocean melts more sea ice, and therefore creates more open water.

A thinner sea-ice cover is weaker, deforms more easily and drifts faster for a given wind forcing. Sea-ice deformations primarily occur along leads where large gradient in the sea-ice velocity (shear) and some divergence or convergence are present. Divergence in the ice pack leads to more open water, more evaporation, and consequently more storms. Therefore, a stormier Arctic leads to more sea-ice deformation and faster drift. Rigor et al. (2002) showed that when the large-scale atmospheric circulation is cyclonic with storms penetrating farther into the eastern Arctic, the wind pattern are such that it advects readily thick multi-year ice from the central Arctic through the Fram Strait. This was the case in the eighties and early nineties when a dramatic loss of multi-year ice was recorded (Johannessen et al., 1999).

The next mechanism is the cloud-ice feedback. If there are more clouds, there is less solar energy income during the summer. This leads to less summer melt and generally to a thicker sea-ice cover. However, liquid water clouds have a strong greenhouse effect and lead to an increase in the downwelling surface longwave radiation and this, during the whole year (Shupe and Intrieri, 2004; Gorodetskaya et al., 2008). The resulting cloud-ice reaction is overall a positive feedback.

The last feedback is linked with the thermal insulation of the ocean. When the ice is thin, it is easier to form ice hence a negative feedback. New formed ice rejects brine. This extra brine builds a stronger cold halocline layer which insulates the top part of the Arctic Ocean

and its sea ice from the warm Atlantic waters just as discussed earlier.

When global climate models include all the feedback processes, they predict the largest change of surface air temperature at high latitudes (Holland and Bitz, 2003). The ice-albedo feedback is likely to account for much of the warming. The Arctic is a magnifying glass for global warming. This is called polar amplification.

With this amplification, the Arctic Ocean could become seasonally ice free by 2050 (Holland et al., 2006b; Stroeve et al., 2007, 2012; Wang and Overland, 2012). All this occurs to the detriment of any ice-dependent species such as narwhal, seal, polar bear, etc. (Laidre et al., 2008; Stirling and Derocher, 2012; TheCircle, 2012; Norris et al., 2002) A seasonal ice-free Arctic will lead to local warming of adjacent land and likely to an acceleration of permafrost melting which will release more greenhouse gas (Schaefer et al., 2012; Lawrence et al., 2008). Since the density of melted ice is not the same as the ocean, a fully melted Arctic would increase the sea level by and extra $47\,mm$ (Noerdlinger and Brower, 2007) compared to $7\,m$ for a fully melted Greenland and $60\,m$ for a fully melted Antarctica estimated by Vaughan et al. (2013). Vulnerabilities will strengthen and develop in Inuit communities (Ford et al., 2006; Ford, 2009). On a more positive side, the maritime shipping routes through the Arctic Ocean will open reducing transport time, cost and hopefully pollution (Melia et al., 2016).

2.4 Community Climate System Model

In order to understand and anticipate the adversities of climate change over the Arctic, the scientific community uses Global Climate Models (GCMs). GCMs modelise the equations of climate on a global scale. Simulations start in the past up to present time and then uses predictions for the greenhouse gases future evolution in order to estimate future climate. This thesis will focus on the results of the Community Climate System Model (CCSM) versions 3 and 4. The CCSM is a coupled climate model consisting of four modules, one for atmosphere, one for ocean, one for land, one for sea ice, and a coupler assuring communication between each module. The general results of the CCSM3 are described in Collins et al. (2006a) and in Gent et al. (2011) for the CCSM4. The CCSM3 uses the Community Atmospheric Model version 3 (CAM3) (Collins et al., 2004, 2006b), the Parallel Ocean Program (POP1) (Smith

and Gent, 2004a), the Community Sea-Ice Model version 5 (CSIM5) (Briegleb et al., 2004) and the Community Land Model version 3 (CLM3) (Oleson et al., 2004; Dickinson et al., 2006; Bonan et al., 2002). The CCSM4 uses the Community Atmospheric Model version 4 (CAM4) (Neale et al., 2010), the Parallel Ocean Program version 2 (POP2) (Smith et al., 2010; Danabasoglu et al., 2012), the Los Alamos sea ice model version 4 (CICE4) (Hunke and Lipscomb, 2010) and the Community Land Model version 4 (CLM4) (Oleson et al., 2008; Stoeckli et al., 2008; Lawrence et al., 2011).

We will narrow our attention to the ocean and sea ice components of the models in sections 2.4.1 and 2.4.2 respectively. For each component, the basic equations used in both versions 3 and 4 as well as their differences are presented. A succinct presentation of the future scenarios used by the CCSM to forecast the climate up to 2100 follows in section 2.4.3. The following model discussion is technical and might be difficult to follow for beginners. It is more informative than explicative.

2.4.1 CCSM ocean component - POP model

A derivation of the fluid equations and approximations can be found in Vallis (2006). The POP model solves the Navier-Stokes equations for u, the eastward velocity, and v, the northward velocity, on a sphere for a thin stratified fluid under the hydrostatic and Boussinesq ($\rho = \rho_0$) approximations (Smith et al., 2010):

$$\frac{\partial}{\partial t}u + \mathcal{L}(u) - (uv\tan\phi)/a - fv = -\frac{1}{\rho_0 a\cos\phi}\frac{\partial P}{\partial\lambda} + \mathcal{F}_{Hx}(u,v) + \mathcal{F}_V(u) \tag{2.4}$$

$$\frac{\partial}{\partial t}v + \mathcal{L}(v) - (u^2\tan\phi)/a + fu = -\frac{1}{\rho_0 a}\frac{\partial P}{\partial\phi} + \mathcal{F}_{Hy}(u,v) + \mathcal{F}_V(v) \tag{2.5}$$

$$\mathcal{L}(\alpha) = \frac{1}{a\cos\phi}\Big[\frac{\partial}{\partial\lambda}(u\alpha) + \frac{\partial}{\partial\phi}(cos\phi v\alpha)\Big] + \frac{\partial}{\partial z}(w\alpha) \tag{2.6}$$

$$\mathcal{F}_{Hx}(u,v) = A_M\big\{\nabla^2 u + u(1-\tan^2\phi)/a^2 - \frac{2\sin\phi}{a^2\cos^2\phi}\frac{\partial v}{\partial\lambda}\big\} \tag{2.7}$$

$$\mathcal{F}_{Hy}(u,v) = A_M\big\{\nabla^2 v + v(1-\tan^2\phi)/a^2 + \frac{2\sin\phi}{a^2\cos^2\phi}\frac{\partial u}{\partial\lambda}\big\} \tag{2.8}$$

$$\nabla^2\alpha = \frac{1}{a^2\cos^2\phi}\frac{\partial^2\alpha}{\partial\lambda^2} + \frac{1}{a^2\cos^2\phi}\frac{\partial}{\partial\phi}\big(\cos\phi\frac{\partial\alpha}{\partial\phi}\big) \tag{2.9}$$

$$\mathcal{F}_V(\alpha) = \frac{\partial}{\partial z}\mu\frac{\partial}{\partial z}\alpha, \tag{2.10}$$

where λ is the longitude, ϕ is the latitude, $z = r - a$ is the depth relative to mean sea level with $a = 6.37122 \cdot 10^6\, m$ being the Earth's radius, $g = 9.80616\, m^2/s$ is the acceleration due to gravity, $f = 2 \cdot \sin\phi$ is the Coriolis parameter, $\rho_0 = 1.026 g/cm^3$ is the background density of seawater, w is the vertical or radial velocity, P is the pressure, Θ is the potential temperature, S is the salinity, A_M is the horizontal diffusion coefficient and μ is the vertical mixing coefficient. The first terms on the left-hand side of equations (2.5) and (2.6), $\frac{\partial}{\partial t}u$ and $\frac{\partial}{\partial t}v$, are the temporal evolution of the horizontal velocities. The second and third terms on the left-hand side represent the advection of the velocities. The fourth and last term on the left-hand side represents the Coriolis force. The first terms of the right-hand side of (2.5) and (2.6) take into account the pressure driven circulation. The second and third terms of the right-hand side contains velocity diffusion, both horizontal and vertical respectively. The second and third terms in brackets in equations (2.7) and (2.8) ensure that no stresses are generated due to solid-body rotation in a shallow layer (Williams, 1972). Wind forcing is applied as a boundary condition of the vertical diffusion. Bottom and lateral boundary conditions applied in POP are no-flux for tracers (zero tracer gradient normal to boundaries) and no-slip for velocities ($u = v = w = 0$). The main parameterizations added are a mesoscale (sub-grid) eddy parameterization (Gent and Mcwilliams, 1990) and a vertical mixing K-profile parameterization (KPP) (Large et al., 1994)

The Boussinesq approximation stipulates that density changes has no effect on the circulation. Therefore, the continuity equation can be used to calculate the vertical velocity as a residual only after the horizontal velocities has been solved,

$$\mathcal{L}(1) = \frac{1}{a\cos\phi}\Big[\frac{\partial}{\partial\lambda}(u) + \frac{\partial}{\partial\phi}(\cos\phi v)\Big] + \frac{\partial}{\partial z}(w) = \nabla\cdot\vec{u} = 0. \tag{2.11}$$

The hydrostatic approximation states that the pressure gradient is balanced by buoyancy only,

$$\frac{\partial p}{\partial z} = -\rho g. \tag{2.12}$$

The scalar variables or tracers such as potential temperature and salinity are calculated

Figure 2.7: CCSM grid with the North Pole displaced over Greenland.

using the tracer transport equation,

$$\frac{\partial}{\partial t}\varphi + \mathcal{L}(\varphi) = D_H(\varphi) + D_V(\varphi) \tag{2.13}$$

$$D_H(\varphi) = A_H \nabla^2 \varphi \tag{2.14}$$

$$D_V(\varphi) = \frac{\partial}{\partial z}\kappa\frac{\partial}{\partial z}\varphi, \tag{2.15}$$

where A_H is the horizontal diffusion coefficients and κ is the vertical mixing coefficients. The surface heat fluxes or fresh water fluxes are applied as surface boundary conditions to the vertical diffusive terms. The first term of the left-hand side of the tracer equation is the temporal evolution of the tracer. The second term represents the tracer advection. The right-hand side contains the horizontal and vertical tracer diffusion.

Once the potential temperature and the salinity are solved, the CCSM calculates the density as a state function depending on potential temperature, salinity and depth. The resulting density field is used to calculate instabilities which can induce motion.

At the North Pole, $\phi = 90°$, every term with a $\frac{1}{cos\phi}$ diverges. At the North Pole, latitudes and longitudes do not have defined derivatives. To avoid any problem with divergent terms, the CCSM chooses a grid with a displaced North Pole over Greenland, see figure 2.7, with a nominal 1° resolution. It is also possible to choose a displaced pole over Canada or a tri-pole grid. To modify the POP model basic equations on a sphere to a different grid, we must use results from differential geometry (Pressley, 2010). Without going into details, the goal is to start with the equations using coordinates (λ, ϕ, z) and end with the equations written with the new coordinates (q_x, q_y, z). The differential length element, ds, is given by:

$$ds^2 = \xi_\lambda^2 + \xi_\phi^2 + dz^2 = \sum_{i,j=1}^{2} h_{ij}^2 dq_i dq_j + dz^2 \tag{2.16}$$

$$h_{ij} = \sum_{k=1}^{2} \frac{\partial \xi_k}{\partial q_i} \frac{\partial \xi_k}{\partial q_j}, \tag{2.17}$$

where ξ_k is the infinitesimal distance given by an infinitesimal change in λ $(k = 1)$ or ϕ $(k = 2)$, h_{ij} is the metric coefficient of the new grid which depends on the local curvature of the new set of coordinates. This metric holds all the required information to rewrite the terms and operators of the equations.

The POP model uses a staggered Arakawa B-grid with tracers (scalar variables) at the centre of a cell and velocities u_x and u_y at the corners of the cell mid height as one can see on the left picture of figure 2.8. From this grid, two sub grid are considered: the T-grid

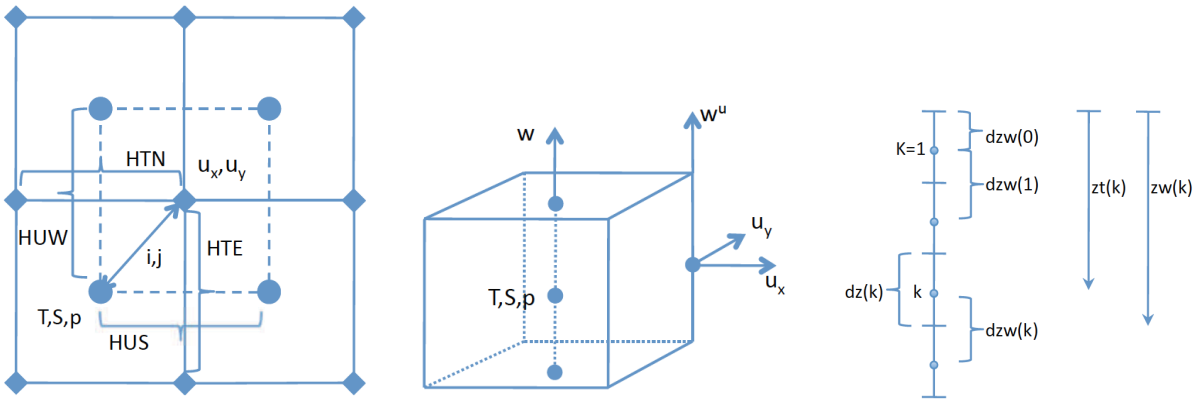

Figure 2.8: Left) Horizontal discretization of the grid showing the locations of tracers, velocities and lengths. Center) Vertical locations of tracers and velocities. Right) Vertical discretization. Taken from Smith et al. (2010).

(tracer-grid) and the U-grid (velocity grid). The T-grid has the tracers at the centre of the cell with velocities at its corners. The U-grid has velocities u_x and u_y at the centre of the grid and tracers at its corners. The vertical velocity, w, can be found at two locations. The first location is at the highest north-east corner of the cell and the second location is mid height on the north-east corner where the horizontal velocities are as one can see on the central panel of figure 2.8. The first location facilitates the advection calculation of the tracers while the second location facilitates the advection calculation of the velocities hence its superscript, w^u. The vertical discretization is illustrated in the right panel of figure 2.8. It increases with depth.

The main improvements between the POP and the POP2 models are the increase of 40 vertical levels to 60 with a new bottom topography, the inclusion of the opening of Nares Strait, a near-surface eddy flux parameterization (Ferrari et al., 2008), vertically varying diffusive coefficients (Ferreira and Marshall, 2006), a submesoscale parameterization (Fox-Kemper et al., 2008; Fox-Kemper and Ferrari, 2008; Fox-Kemper et al., 2011), a deep overflow parameterization (Briegleb et al., 2010), and an abyssal tidally driven mixing parameterization (Jayne, 2009). Jahn et al. (2012) showed that the temperature-salinity profile of the CCSM4 worsens comparatively to the CCSM3 when compared to observations. The CCSM3 temperature-salinity profile agrees satisfactorily with observations. The CCSM4 has issues at all depth. The surface waters are too cold and too saline. Between 50 and 300 metres, the salinity is too low compared to observations while the temperature profile agrees with the observations. From 400 metres until the ocean floor, the temperature is too high and stays $1°C$ too high until the ocean floor with a salinity profile slightly too high. The observed warm Atlantic waters are located at 400 metres while the simulations place them at 750 meters. The simulated Atlantic waters in the Arctic Ocean are too deep and too warm. The CCSM3 temperature-salinity profile agreed better with observations. The general shape of the ocean circulation agrees with observations specially the inflow from the Fram Strait and the Barents and Kara seas, the cyclonic boundary current around the marginal seas, the Canadian Basin gyre, the return flow along the Lomonosov Ridge and the return current west and north of Svalbard. The velocities are too low at the gates of the Arctic Ocean but the temperature

agrees with observations leading to wrong heat fluxes entering and exiting the Arctic Ocean.

2.4.2 CCSM sea ice component - CICE model and CSIM

From Hunke and Lipscomb (2010), the fundamental equation solved by CICE is (Thorndike et al., 1975)

$$\frac{\partial g}{\partial t} = -\nabla \cdot (g\vec{u}) - \frac{\partial}{\partial t}(fg) + \psi, \tag{2.18}$$

where g is the ice thickness distribution function defined as $g(\vec{x}, h, t)dh$ being the fractional area covered by ice in the thickness range $(h; h + dh)$ at a given time and location, $\vec{u}$ is the horizontal ice velocity vector, f is the rate of thermodynamic ice growth and ψ is a ridging redistribution function.

This equation is discretized horizontally on the same horizontal grid as the ocean model and in discrete thickness categories. The thickness does not become discrete, the ice still changes continuously inside its thickness category. As an example, consider a two thickness category model where the first category ranges from 0 to $1\,m$ and the second category includes any ice thicker than $1\,m$. This model allows a cell with a section with sea ice less thick than $1\,m$ and another section with ice thicker than $1\,m$. At the beginning of winter, the first category could start with 30% of $50\,cm$ and 70% of $2\,m$ sea ice. Through the cold season, both category will grow, possibly at different rate. When the first category grows up to $1\,m$, its sea ice will be transferred to the next category. The thickness discretization allows a number of different thicknesses inside a same cell. Without it, a cell would have only one thickness, its averaged thickness.

The CICE models follow three steps to solve the fundamental equation (2.18): 1) calculation of the sea ice velocities, u and v, 2) calculation of the sea-ice and tracer transports and calculation of the ridging of sea ice, 3) calculation of thermodynamic processes, such as growing and melting, affecting the temperature and salinity profiles. This *modus operandi* is repeated at every time increment. Each step is explained more thoroughly in the next paragraphs.

The CICE model starts by solving ice dynamics using an elastic-viscous-plastic (EVP) model (Hunke and Dukowicz, 1997). The EVP models treats the ice pack as a plastic material

under typical stress conditions but behaves as an elastic-viscous fluid where strain rates are small. The equations of the sea ice dynamics are

$$m\frac{\partial \vec{u}}{\partial t} = \nabla \cdot \sigma + \vec{\tau_a} + \vec{\tau_w} - m\, f\, \hat{k} \times \vec{u} - m\, g\, \nabla H_0 \tag{2.19}$$

$$\vec{\tau_a} = c_a \cdot \rho_a \cdot |\vec{U_a}| \cdot (\vec{U_a} cos\phi + \vec{k} \times \vec{U_a} sin\phi), \tag{2.20}$$

$$\vec{\tau_w} = c_w \cdot \rho_w |\vec{U_w} - \vec{u}| \left[(\vec{U_w} - \vec{u}) \cos\lambda + \vec{k} \times (\vec{U_w} - \vec{u}) sin\lambda \right], \tag{2.21}$$

where m is the combined mass of ice and snow per unit area, $\vec{\tau_a}$ and $\vec{\tau_w}$ are the wind and ocean stresses, σ is the internal stress tensor containing the EVP characteristics of the ice model, $m\, f\, \hat{k} \times \vec{u}$ is the Coriolis force and $m\, g\, \nabla H_0$ is the effect of the sea surface slope. The details of the internal stress tensor can be found in Hunke and Lipscomb (2010).

With the updated velocities, CICE calculates the transport and ridging of sea ice through three variables: 1) sea ice concentration a_{in} for a given grid cell and for a given thickness category n, 2) sea ice volume $v_{in} = a_{in} \cdot h_{in}$ where h_{in} is the ice thickness and 3) internal ice energy for a given vertical layer k, $e_{ink} = \frac{v_{in}}{N_i} \cdot q_{ink}$ where N_i is the total number of ice categories and q_{ink} is the ice layer enthalpy which is minus the amount of energy required to melt a unit volume of ice and raise its temperature to $0°C$. The transport equations are:

$$\frac{\partial a_{in}}{\partial t} + \nabla \cdot (a_{in} \vec{u_i}) = 0, \tag{2.22}$$

$$\frac{\partial v_{in}}{\partial t} + \nabla \cdot (v_{in} \vec{u_i}) = 0, \tag{2.23}$$

$$\frac{\partial e_{ink}}{\partial t} + \nabla \cdot (e_{ink} \vec{u_i}) = 0. \tag{2.24}$$

The equations of ridging, variable ψ in equation (2.18), are described in Lipscomb et al. (2007). A similar set of equations is prescribed in the CICE model for the snow residing over sea ice.

Tracers transport is calculated using the updated velocities,

$$\frac{\partial a_{in} T_n}{\partial t} + \nabla \cdot (a_{in} T_n \vec{u_i}) = 0, \tag{2.25}$$

$$\frac{\partial v_{in} T_n}{\partial t} + \nabla \cdot (v_{in} T_n \vec{u_i}) = 0, \tag{2.26}$$

$$\frac{\partial v_{sn} T_n}{\partial t} + \nabla \cdot (v_{sn} T_n \vec{u_i}) = 0, \tag{2.27}$$

Where T_n denotes the tracer value for the sea ice thickness category n.

Once the transport is calculated, the CICE model considers thermodynamics of sea ice. The thermodynamics of sea ice include surface and bottom forcing, temperature and salinity

changes, melt and growth. The surface forcings are given by

$$F_0 = F_s + F_l + F_{lw} + (1-\alpha)(1-i_0)F_{sw}, \tag{2.28}$$

where $F_s = C_s(\Theta_a - T_{sf})$ is the sensible heat flux with C_s being a nonlinear turbulent heat transfer coefficient and Θ_a being the atmosphere's surface potential temperature, $F_l = C_l(Q_a - \frac{q_1}{\rho_a}\exp(\frac{-q_2}{T_{sf}}))$ is the latent heat flux with C_l being a nonlinear turbulent heat transfer coefficient and Q_a being the atmosphere's specific humidity at the surface, $F_{lw} = \epsilon F_{lw\,a} - \epsilon\sigma_{SB}T_{sf}^4$ is the longwave heat flux with $\epsilon = 0.95$ being the emissivity of snow or ice, $F_{lw\,a}$ being the longwave atmospheric radiation reaching sea ice and σ_{SB} is the Stefan-Boltzmann constant, α is the albedo of sea ice, $1 - i_0$ is the fraction of absorbed shortwave flux that penetrates into the ice, F_{sw} is the incoming short wave radiation. The albedo and penetrative fraction of short wave radiation depend on sea ice thickness, surface ice optical properties, presence of melt pond or snow. They are calculated by the model. The bottom heat flux between the ocean and sea ice, F_{bot}, is given by

$$F_{bot} = -\rho_w \cdot c_w \cdot c_h \cdot u_* \cdot (T_w - T_{fr}), \tag{2.29}$$

where ρ_w is the water density, c_w is the water heat capacity, c_h is the heat exchange coefficient, $u_* = \sqrt{|\tau_w|/\rho_w}$ is the friction velocity, $|\tau_w|$ is the norm of the shear stress given by $\rho_w\sqrt{\frac{\partial u}{\partial y}^2 + \frac{\partial v}{\partial x}^2}$, T_w is the surface water temperature, $T_{fr} = -1.8°C$ is the freezing temperature of ocean water.

The vertical salinity profile is prescribed. The midpoint salinity $S_{i\,k}$ in each ice layer k is given by

$$S_{i\,k} = \frac{1}{2}S_{max}[1 - \cos(\pi z^{\frac{a}{z+b}})], \tag{2.30}$$

where $z = (k - 1/2)/N_i$, S_{max}= 3.2 psu and $a = 0.407$ and $b = 0.573$ (Hunke and Lipscomb, 2010). The snow is assumed to be fresh. The temperature profile of sea ice, T_i, is given by

$$\rho_i \cdot c_i \cdot \frac{\partial T_i}{\partial t} = \frac{\partial}{\partial z}\left(K_i\frac{\partial T_i}{\partial z}\right) - \frac{\partial I_{pen}}{\partial z}, \tag{2.31}$$

where ρ_i is the sea ice density assumed to be constant and uniform, $c_i(T, S)$ is the specific heat of sea ice, $K_i(T, S)$ is the thermal conductivity of sea ice, $I_{pen}(z)$ is the solar penetrative radiation at depth z.

Melt is split into three processes based on the location of the melting: surface, bottom and lateral. Surface melting is calculated as:

$$\Delta h = (F_0 - F_{ct})/q \tag{2.32}$$

$$F_{ct} = F_{ct} \qquad = \kappa \frac{\partial T}{\partial z}, \tag{2.33}$$

where Δh is the change in thickness, F_{ct} is the heat conduction at the top of the ice, q is the enthalpy of pure ice, κ is the thermal conductivity of sea ice and T is the vertical temperature profile of sea ice. Bottom melting or growth is given by

$$\Delta h = \frac{F_{cb} - F_{bot}}{q} \Delta t, \tag{2.34}$$

$$F_{cb} = K_h \cdot (T_q - T_{bot}), \tag{2.35}$$

$$F_{bot} = -\rho_w \cdot c_w \cdot c_h \cdot u_* \cdot (T_w - T_{fr}), \tag{2.36}$$

where F_{cb} is the conductive heat flux through the bottom of the ice, $q = -\rho_i(-c_0(\mu S + T) + L_0(1 + \mu S/T) + c_w \mu S)$ is the enthalpy of the ice with $c_0 = 2106$ J/kg/K the specific heat of fresh ice at $0°C$, $L_0 = 334000$ J/kg the latent heat of fusion of fresh ice at $0°C$ and $\mu = 0.054$ K/psu the ratio between the freezing temperature and salinity of brine, Δt is the time step, K_h is the heat conductivity of sea ice, T_q is the temperature of sea ice calculated from enthalpy q, T_{bot} is the temperature at the base of the ice, ρ_w is the water density, c_w is the water heat capacity, c_h is the heat exchange coefficient, $u_* = \sqrt{|\tau_w|/\rho_w}$ is the friction velocity, $|\tau_w|$ is the norm of the shear stress given by $\rho_w \sqrt{\frac{\partial u}{\partial y}^2 + \frac{\partial v}{\partial x}^2}$, T_w is the water temperature, T_{fr} is the water freezing temperature. If Δh is positive, basal growth is occurring. If Δh is negative, bottom melting is occurring. Another process adds bottom ice: frazil ice. Frazil ice develops as supercooled droplets which form small crystals of ice in the mixed layer and, due to their

buoyancy, reach the surface of the ocean. It is calculated as:

$$frazil = \frac{(T_{fr} - T_w) \cdot c_w \cdot \rho_w \cdot h_{mix}}{q_0} \tag{2.37}$$

where h_{mix} is the thickness of the ocean mixed layer, q_0 is the enthalpy of newly formed ice. Finally, lateral melting is calculated as

$$F_{side} = rside \cdot E_{tot}, \tag{2.38}$$

$$rside = \frac{m_1 \cdot (T_w - T_{bot})^{m_2} \cdot \pi}{\alpha \cdot f_D}, \tag{2.39}$$

where E_{tot} is the total energy available to melt ice and snow, $m_1 = 1.6 \cdot 10^{-6}$ and $m_2 = 1.36$ are coming from Maykut and Perovich (1987), $\alpha = 0.66$ from Steele (1992), f_D is the flow diameter set at $300\,m$. Note that the surface and bottom melt impact sea ice area when the sea ice thickness reach the thinnest thickness layer; half of the energy goes to reducing thickness while the other half goes to reducing sea ice area.

The main differences between the CSIM5 and the CICE4 are an improved ridging scheme (Lipscomb et al., 2007), a melt pond parameterization (Holland et al., 2011) and a new radiative transfer scheme (Briegleb and Light, 2007) which includes effect of melt pond and absorber such as black carbon and dust on optical properties of sea ice.

The seasonal cycle of the sea ice extent of the CCSM3 was too high during winter and slightly too high during summer (Holland et al., 2006c). The CCSM4 solved both problems agreeing better with observations (Jahn et al., 2012). The CCSM3 sea ice concentration is extending too far outside the Arctic Ocean while the CCSM4 contains it better (Gent et al., 2011). The trend of sea ice extent between 1981 and 2005 is not well represented in the CCSM4 with 2 simulations not simulating any significant loss. The CCSM4 has thicker ice close to Canada agreeing better with the observations than the CCSM3. The CCSM4 sea ice is too thick in the centre of the Arctic Ocean and it lacks multiyear ice (Jahn et al., 2012). The CCSM4 sea ice motion shows the standard large scale features such as the Beaufort Gyre and the Transpolar Drift Stream. Though, the simulated ice speeds are too large and show a wider distribution compared with observations.

2.4.3 Future projections

The CCSM simulates the present climate and projections of future climate up to 2099. The Intergovernmental Panel on Climate Change (IPCC) published studies of future projections of greenhouse gases (IPCC, 2007, 2013). Those greenhouse gases reflect energy that would have normally escaped our atmosphere. The sum of all the extra energy from all the greenhouse gases is called radiative forcing. The radiative forcings for the Special Report on Emissions Scenarios (SRES) (IPCC, 2007) and the Representative Concentration Pathways (RCP) (IPCC, 2013) are shown in figure 2.9. The SRES includes six families of scenario: A1FI, A1B, A1T, A2, B1, and B2. This thesis focus strictly on SRES A1B. The RCP includes four different pathways: RCP2.5, RCP 4.5, RCP6.0, RCP8.5. The scenarios RCP8.5 and RCP6.0 strictly increase while RCP4.5 stabilizes by 2070 and RCP2.5 peaks at $3\,W/m^2$ by 2040 and then decreases. Note that before 2060, RCP4.5 is stronger than RCP6.0. The same happens for the SRES A1B and A2. Before 2050, SRES A1B is stronger than A2 even if by 2100 A2 has a higher radiative forcing than A1B. Those periods of higher forcing can have an important impact on the climate. If an important event happens due to the higher radiative forcing during those years, the simulated climate could be significantly different.

2.5 Conclusion

The Arctic is the northern portion of planet Earth. At its center lies the Arctic Ocean covered by sea ice. Warm waters enter through the Bering Strait, east of Fram Strait as the West Spitzbergen Current, and through the Barents Sea. Cold waters exit through the Canadian Arctic Archipelago and west of Fram Strait as the East Greenland Current. The Arctic Ocean is characterized by a cold halocline layer between $50\,m$ and $200\,m$ deep. The cold halocline layer insulates the surface ocean and its sea ice from the warm Atlantic layers $300\,m$ deep.

The sea ice is a complex material that under specific circonstances can reject its brine or keep it. The sea ice concentration of a defined region is measured by a satellite radiometer. The error on such measurements can reach up to 25%. Sea ice extent includes all area with more than 15%. It counteracts most of the error on sea ice concentration. Sea ice extent is

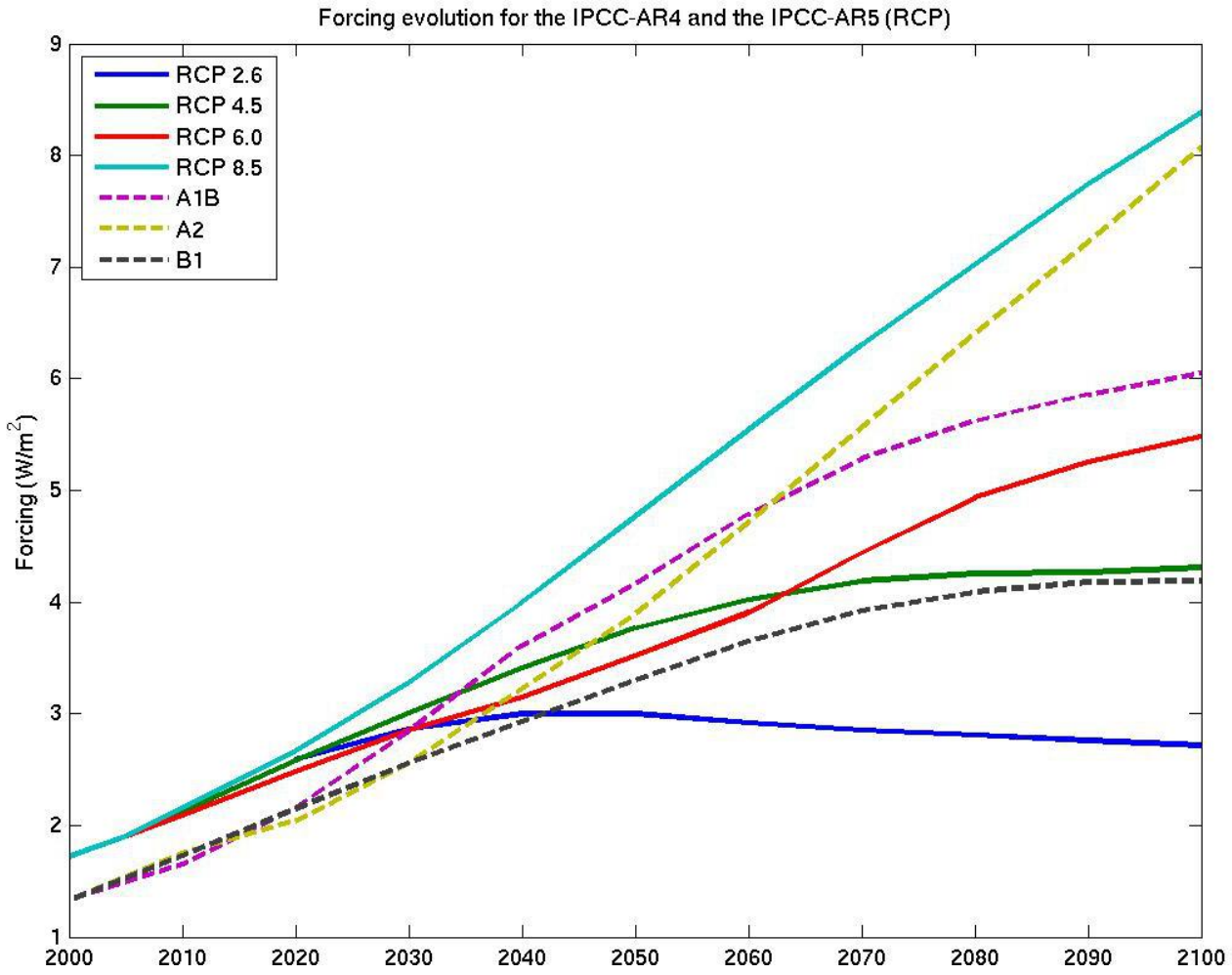

Figure 2.9: Radiative forcing evolution of the different scenarios of the IPCC-AR4 (A1B, A2, B1) and IPCC-AR5 (RCPs).

minimum over the month of September. September sea ice extent reached new low records in 2002, 2005, 2007 and 2012. Sea ice thickness is complicated to measure and observations are scarce both spatially and temporally. It can be done with the help of Ultra Light Sonar, Electromagnetic Sounding, satellites or drilled holes. All observations point to a decrease in sea ice thickness. The sea ice thickness decreased comparably more than sea ice extent.

The Arctic reacts more quickly and more intensely to climate changes. As the sea ice extent decreases, more open water is accessible to the solar radiation. While the sea ice reflects most of the solar radiation, the ocean absorbs most of it. The exposed water gets warmer and melt more sea ice which leaves more open water. It is a positive feedback named the Albedo feedback. It could thaw all summer sea ice in the next decades to come.

Holland et al. (2006a) observed abrupt reductions of Arctic September sea ice extent in

the seven CCSM3 simulations forced by the SRES A1B leading to a summer ice free Arctic Ocean as soon as 2050. They stipulated that one to two years prior the abrupt loss of sea ice extent, pulses of ocean advective heat flux might have preconditioned the sea ice to a rapid loss. The thermodynamic interactions between the sea ice and the ocean is not well documented. It is usually calculated as a residual of all the sea ice forcings and the change in sea ice thickness. This thesis aims at describing the exchanges of heat between the sea ice and the ocean studying extensively all the thermodynamical processes linked to sea ice.

In order to proceed, the seven CCSM3 simulations forced by the SRES A1B will be studied. The CCSM3 has four modules - ocean, sea ice, land, atmosphere - and a coupler linking each parts. The ocean component is the POP model. It solves the Navier Stokes equations for a thin stratified fluid under hydrostatic equilibrium and Boussinesq approximation. The POP model uses a staggered Arakawa B grid with a displaced North Pole. The sea ice components is the CICE model. It has the same grid as the POP model. It solved the advection and forcings of sea ice. Its sea ice is elastic-viscous-plastic (EVP). The model cells have five thickness categories plus open water. The CCSM3 has limited outputs making some analyses impossible. The CCSM4 is also studied for its extensive outputs.

Chapter 3 investigates all the processes affecting sea ice focussing on the seven CCSM3 simulations forced by the SRES A1B. Chapter 4 presents how to calculate all the energy fluxes affecting the surface ocean layer. The CCSM4 having numerous outputs, the heat budget is more readily to compute. Chapter 5 shows an analysis of the advective heat fluxes through the gates of the Arctic Ocean. Both the CCSM versions 3 and 4 are compared.

3 Physical processes affecting sea ice in the Community Climate System Model (CCSM) version 3

The fate of the Arctic sea ice is of capital importance for the Arctic biota, maritime transportation, the governments and the oil industry. Until recently, the idea that the Arctic Ocean might see summertime ice-free conditions as early as 2040 was unheard of. That this could occur under reasonable forcing scenarios was made evident in an article by Holland et al. (2006a). They examined the seven simulations from the Community Climate System Model version 3 (CCSM3) under the SRES A1B scenario for future forcings and greenhouse gases. They observed abrupt loss of sea ice in all of the seven simulations. Based on Holland et al. (2006a), an abrupt loss occurs when the time derivative of the five year running mean of September sea ice extent is inferior to -0.5 million km^2/a. They observed that these events start on a year of low sea ice thickness preceded by "pulse-like" heat transport from the ocean one to two years prior. Subsequently, the albedo feedback accelerates the sea ice loss as more solar radiation is absorbed by the ocean which in turn transfers it to the sea ice. Which physical processes are responsible for the bulk of this decline is, however, unclear.

In this chapter, we examine all the physical processes affecting sea ice in the simulations presented in Holland et al. (2006a). To do so, we base our analysis on sea ice volume instead of sea ice area. This choice is motivated by the fact that heat fluxes affect sea ice volume directly. Sea ice extent and sea ice area are indirectly affected by heat fluxes. In the CCSM3, when the sea ice thickness gets into the smallest thickness category, the sea ice area diminishes as well as the thickness. More precisely, half of the energy available for melt reduce the area and the other half reduce the thickness.

In section 3.1, we describe the sea ice volume evolution. Once the sea ice volume evolution is comprehended, we compare the dynamic and thermodynamic processes in section 3.2. We find that the net dynamic and the net thermodynamic processes are equally important. Thus, we study more extensively each of them. In section 3.3, we study the dynamical processes.

In section 3.4, we study the thermodynamic processes. In the CCSM3, the thermodynamic processes are: surface melt, basal melt, lateral melt, basal growth, frazil ice creation. We find

that only the surface melt, basal melt and basal growth are important. For that reason, we study further the components of the surface melt and basal interactions. In section 3.4.1, we study the components of the surface fluxes. In section 3.4.2, we study the basal interactions. Once all the important terms are analyzed, our conclusions are summarized in section 3.5. But first, we present the sea ice volume evolution from the CCSM3 simulations under the SRES A1B scenario.

3.1 Sea ice volume

The state of sea ice is usually described using sea ice extent. Sea ice extent is defined as the sum of the area of every cell with at least 15% sea ice coverage. In this study, we consider sea ice volume instead. The reason for that choice is that sea ice volume is always affected by

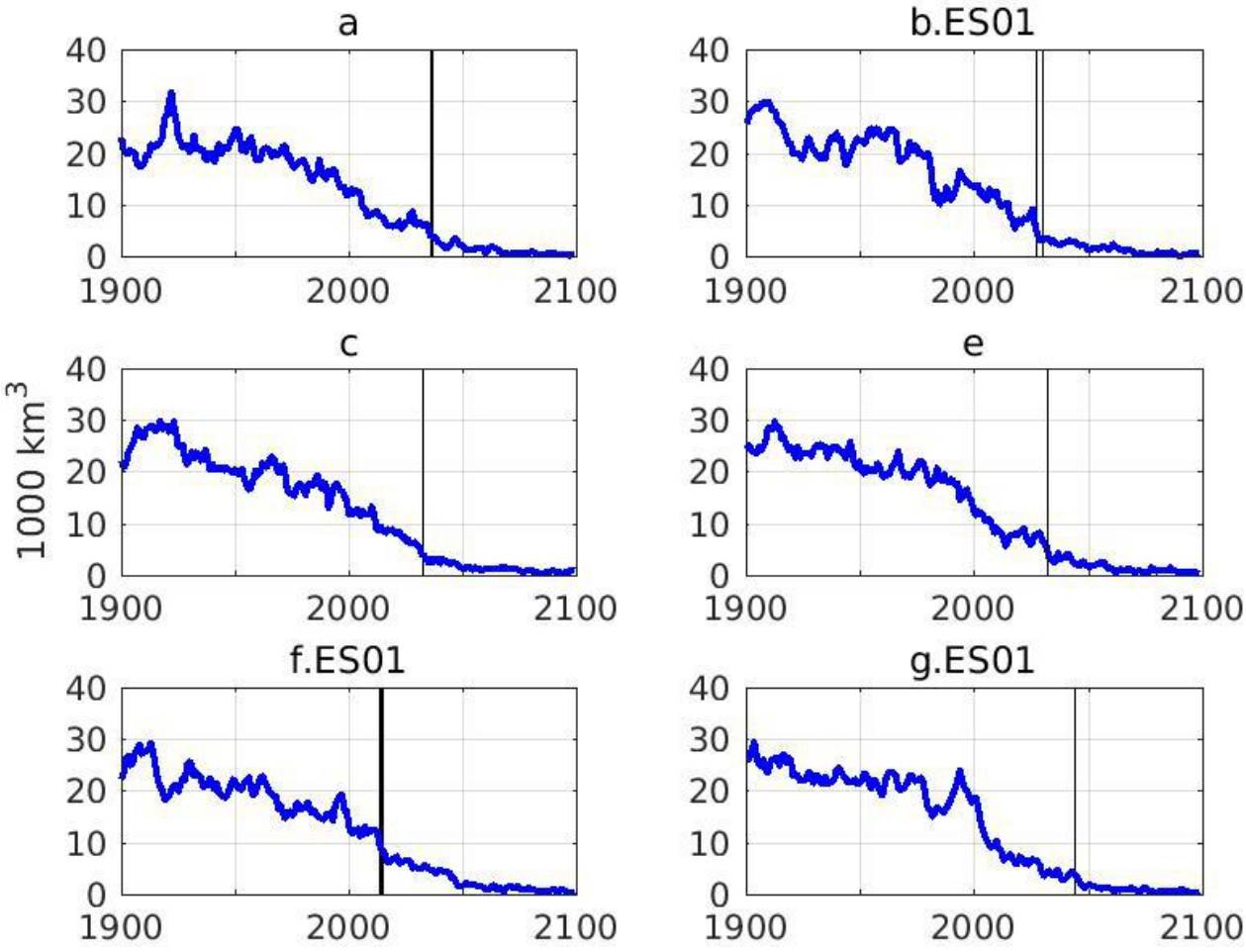

Figure 3.1: Yearly minimum Arctic sea ice volume. The vertical lines represents the years of rapid September sea ice decline.

dynamic and thermodynamic processes. It is not the case for sea ice extent which depends on a threshold on the sea ice concentration. And since we are concerned by the effect of physical processes on sea ice, it seemed the logical choice. Another reason for choosing sea ice volume is that it better represents the state of sea ice. The NSIDC sea ice extent trend during the 1979 to 2012 period has been of -14.2%/decade while the PIOMAS sea ice volume trend for the same period is of -27.8%/decade or -2,800 km^3/a (Schweiger et al., 2011). The sea ice volume is changing at a faster rate than sea ice extent. Therefore, some changes in sea ice volume are not reflected in the sea ice coverage. We believe that the study of the sea ice volume offers a clearer picture of the sea ice state rather than sea ice extent. This feature is also present in the simulations of the CCSM3 under the SRES A1B scenario. For the month of September between 1980 and 2010, the sea ice extent trend is of -6.9%/decade while the sea ice volume trend is of -17.2%/decade. These values are lower in magnitude than the observations. It is known that the sea ice calculated from climate models is more

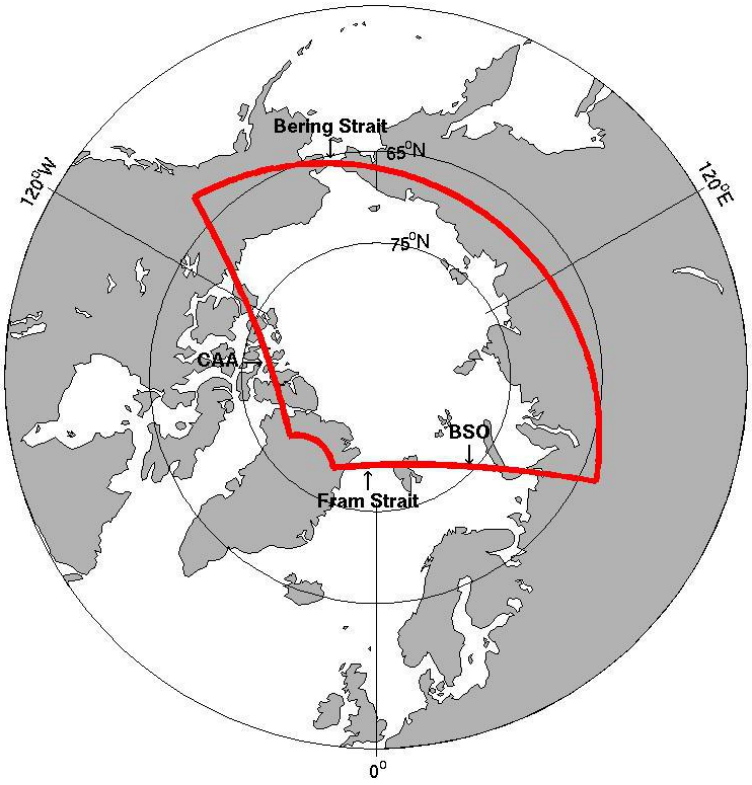

Figure 3.2: Arctic Ocean domain including the four main gates considered in this study: Fram Strait, Barents Sea Opening (BSO), Bering Strait and Canadian Arctic Archipelago (CAA). For simplicity, all gates are defined along lines of constant latitude or longitude index in the rotated grid.

conservative than observations (Overland and Wang, 2013). Now that our reasoning for choosing sea ice volume over sea ice area is presented, we will detail our calculation of the sea ice volume.

The yearly minimum sea ice volume for the six SRES A1B simulations of the CCSM3 is shown in figure 3.1. We focus on the minimum sea ice volume because it is more closely linked to the September sea ice extent abrupt loss. It also show when the Arctic Ocean becomes ice free. We also show the years of rapid declines introduced in Holland et al. (2006a). Since our goal is to understand the sources of these abrupt losses of sea ice we find it important to show the event years for every result. The sea ice volume is calculated over the Arctic region presented in figure 3.2. We chose this region because we are interested in linking the sea ice to Arctic physical processes. Using this region allows us to exclude all processes from the Atlantic or Pacific Oceans. Our results are spatially integrated over this region unless said so. Lastly, we kept the original names of the simulations: a, b.ES01, c, e, f.ES01 and g.ES01.

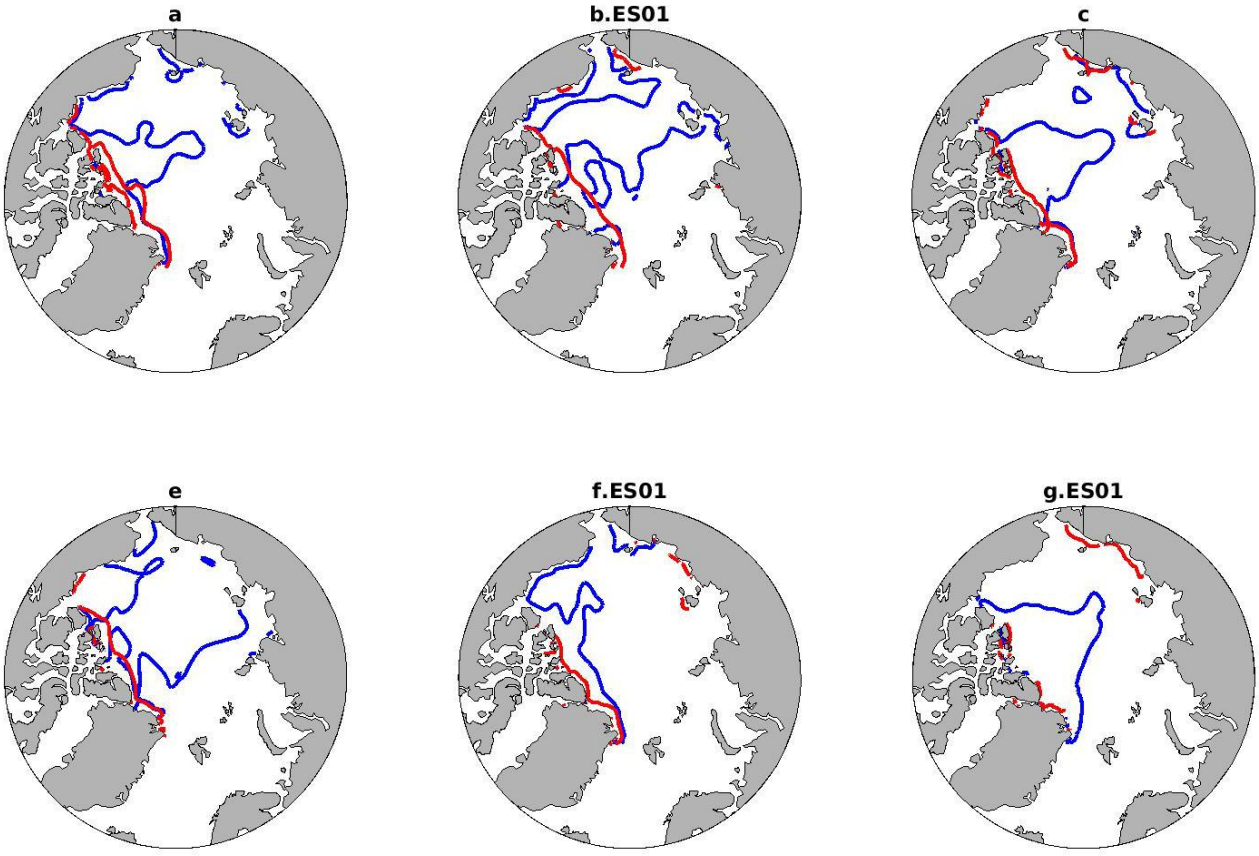

Figure 3.3: One-meter thickness contour plot for the month of September. Blue) Five years before the rapid loss event. Red) Five years after the rapid loss event.

The minimum sea ice volume starts near 25,000 km^3 for all simulations as can be seen from figure 3.1. Between 1900 and 1950, an accumulation of sea ice volume occurs which is immediately lost. Simulation c has the most prominent one with an increase of 7,000 km^3 from 1900 to 1920 which is lost by 1930. From 1950 to 2000, sea ice volume decreases at a mean rate of -110 km^3/a. From 2000 to 2050, the sea ice volume decreases rapidly at a mean rate of -230 km^3/a. During the years of abrupt loss of September sea ice extent, the volume decreases slightly more rapidly but not in an exceptional way. This behaviour has already been described in Holland et al. (2006a). For the rest of the simulated time, the sea ice volume decreases slowly at a mean rate of -20 km^3/a ending close to zero by 2100. The minimum sea ice volume occurs mainly in September with some exceptional years where it occurs in October. For the last 25 years of the simulations, it occurs only in October.

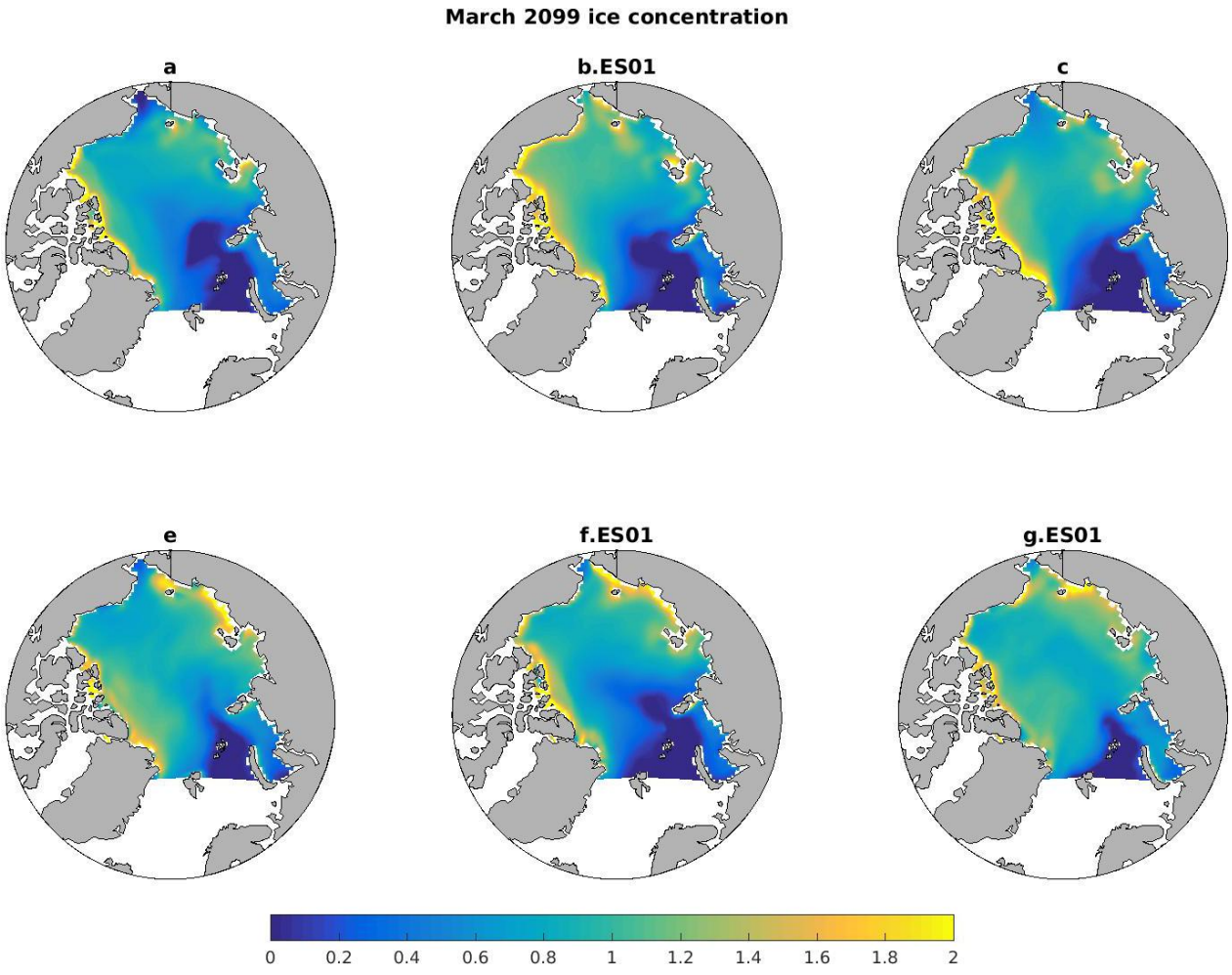

Figure 3.4: March 2099 sea ice thickness distribution.

The extent of the sea ice thickness decreases considerably during the years of rapid sea ice declines, see figure 3.3. Before the abrupt loss events, the region with sea ice thicker than one meter covers the center of the Arctic Ocean. After the abrupt loss events, the sea ice thicker than one meter clings to the Canadian and Greenland coasts. This observation is similar to what is described in Holland et al. (2006a) for the sea ice extent. The loss of sea ice does not stop. By 2099, even the winter sea ice distribution is greatly affected, as can be seen in figure 3.4. In March 2099, the Arctic is not able to form ice in the Barents Sea over the full winter. There is also a retreat at the entrance of the Bering Sea though modest. Simulation a shows the most important loss. This concludes our description of the sea ice volume. We are interested in what caused the sea ice to change. In the next section, we study the strength of the dynamic and thermodynamic processes.

3.2 Dynamic vs thermodynamic processes

The thermodynamic processes create sea ice while the dynamic processes export almost the same amount of sea ice, see figure 3.5. Thermodynamic processes create sea ice at a rate of 4,750 km^3/a in 1900 and decrease down to 900 km^3/a in 2100. It represents a loss of 80% of the sea ice volume creation. The dynamic processes magnitude decreases likewise. The thermodynamic and dynamic processes cancel each other even when averaged over the region of rapid loss of September sea ice extent. This equality holds even when studied monthly over the years of rapid sea ice decline. The values presented in figure 3.5 concord with the results from Serreze et al. (2007) and Holland et al. (2010).

These results do not contradict those of Holland et al. (2006a) and Auclair and Tremblay (2018). In both studies, they looked at the dynamic and thermodynamic processes for summer months. During the summer, thermodynamic processes strictly melt sea ice. It is true that over that time span the dynamic processes are negligible compared to the melt. When integrating over the full year though, thermodynamic processes also include the sea ice formation which results in a net sea ice creation almost equal to the dynamic processes. As will be seen further, before the rapid loss of sea ice extent the sea ice creation is constant. Hence leaving only melt as a cause to the rapid loss events. For that reason, the conclusions

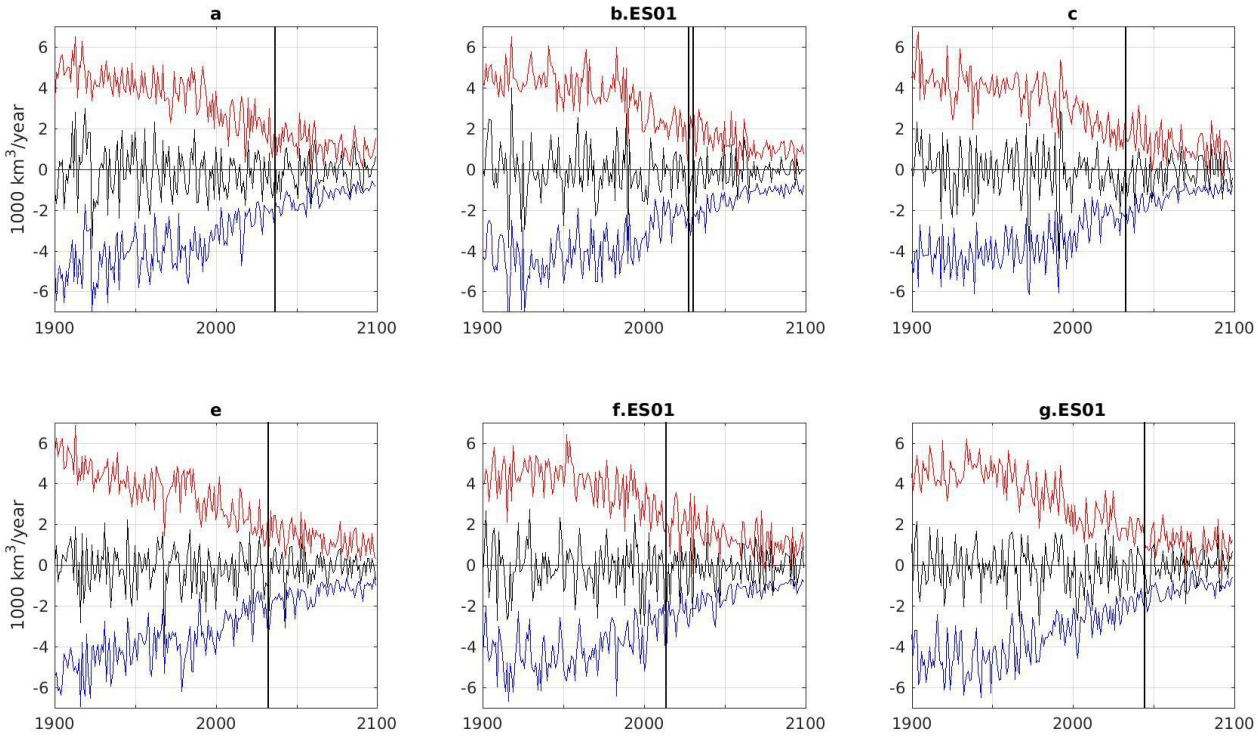

Figure 3.5: Red) Change in sea ice volume caused by thermodynamic processes. Blue) Change in sea ice volume caused by dynamic processes. Black) Total change in sea ice volume. These quantities are obtained from integrating over the Arctic domain presented in figure 3.2. Vertical black lines represent the years of rapid September sea ice decline.

from Holland et al. (2006a) and Auclair and Tremblay (2018) still holds.

Now that it is clear that both dynamic and thermodynamic processes are important, we will examine thoroughly the different processes composing them. The dynamic processes are detailed in section 3.3. The thermodynamic processes are detailed in section 3.4. Once the foremost components identified, we compare them in section 3.5.

3.3 Dynamic processes

The dynamic processes affecting sea ice volume include the transport of sea ice through the gateways of the Arctic Ocean: Fram Strait, Barents Sea Opening, CAA and Bering Strait. The transport of sea ice through the Fram Strait is dominating all the other gates as can be seen in figure 3.6. Averaged over the 1900-1910 time period, the Fram Strait exports 4,000 km^3/a of sea ice while the Barents Sea Opening exports 200 km^3/a, the CAA exports 40 km^3/a and the Bering Strait imports 200 km^3/a. The Fram Strait export is more than ten

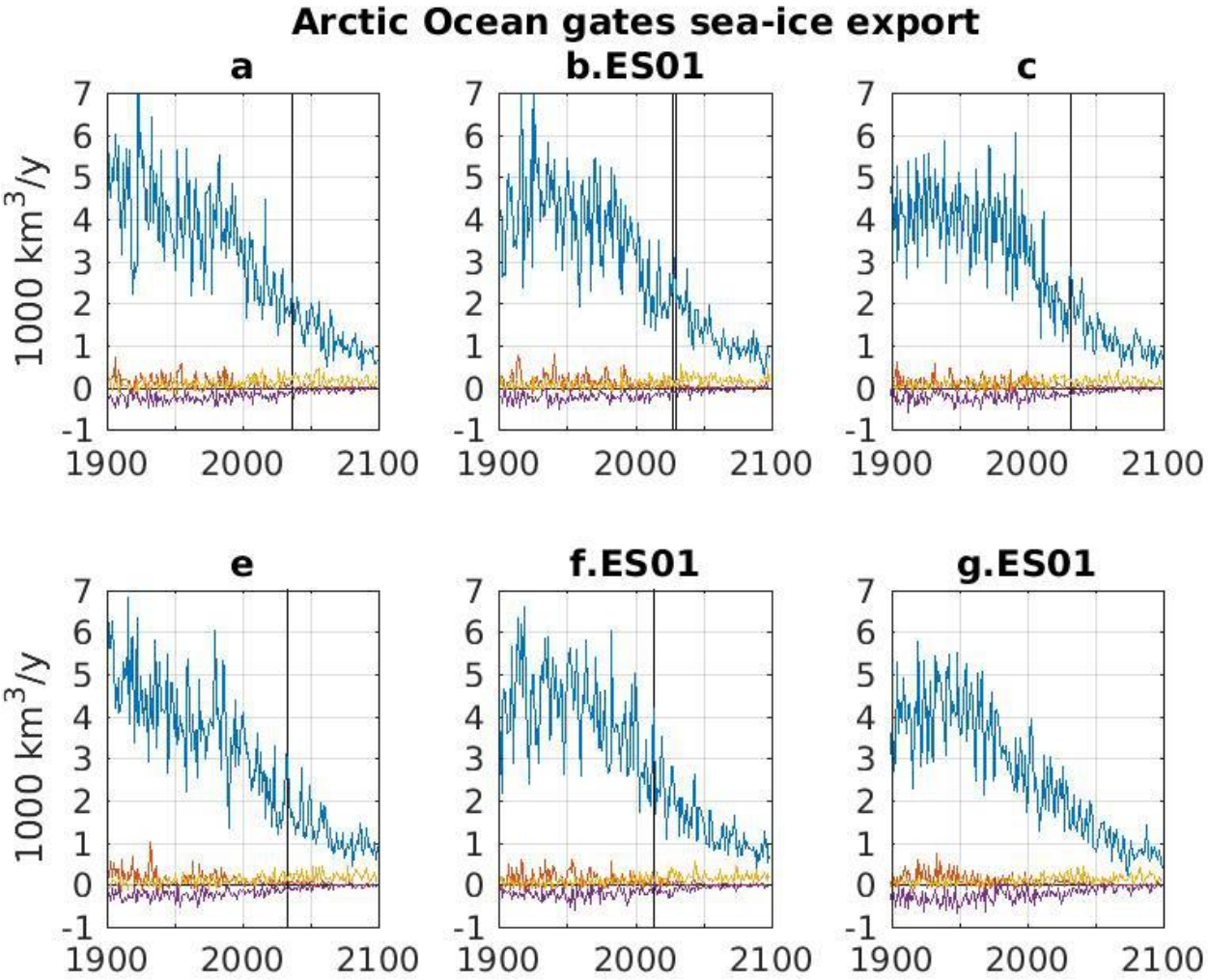

Figure 3.6: Sea ice transport through the gateways of the Arctic Ocean averaged yearly. Blue) Fram Strait. Red) Barents Sea Opening. Yellow) CAA. Purple) Bering Strait.

times more important than the other gateways. Hence, its evolution is the most important factor that affects the future of sea ice. The export through the Fram Strait decreases modestly until the forcing scenario starts year 2000 where it decreases rapidly until 2080 where is stabilizes at 700 km^3/a.

Considering the constant decrease in sea ice transport, we do not believe it causes or facilitates the rapid decline events. On the contrary, we believe it works against the rapid loss of sea ice extent. The source or sources of the rapid decline events ought to come from thermodynamic processes. The next section analyse the thermodynamic processes.

3.4 Thermodynamic processes

The thermodynamic processes include: surface melt, bottom melt, lateral melt, basal growth and frazil formation. As can be seen in figure 3.7, the most important process is the basal growth. It is stable at 10,100 km^3/a until the rapid sea ice decline events and decreases briskly until 2080 where it stabilizes at 6,800 km^3/a. Because it is stable until the rapid sea ice decline events, it cannot have caused it. For the same reason, frazil formation of sea ice and lateral melt can be discarded. The frazil formation averages at 2,100 km^3/a and the lateral melt averages at -800 km^3/a.

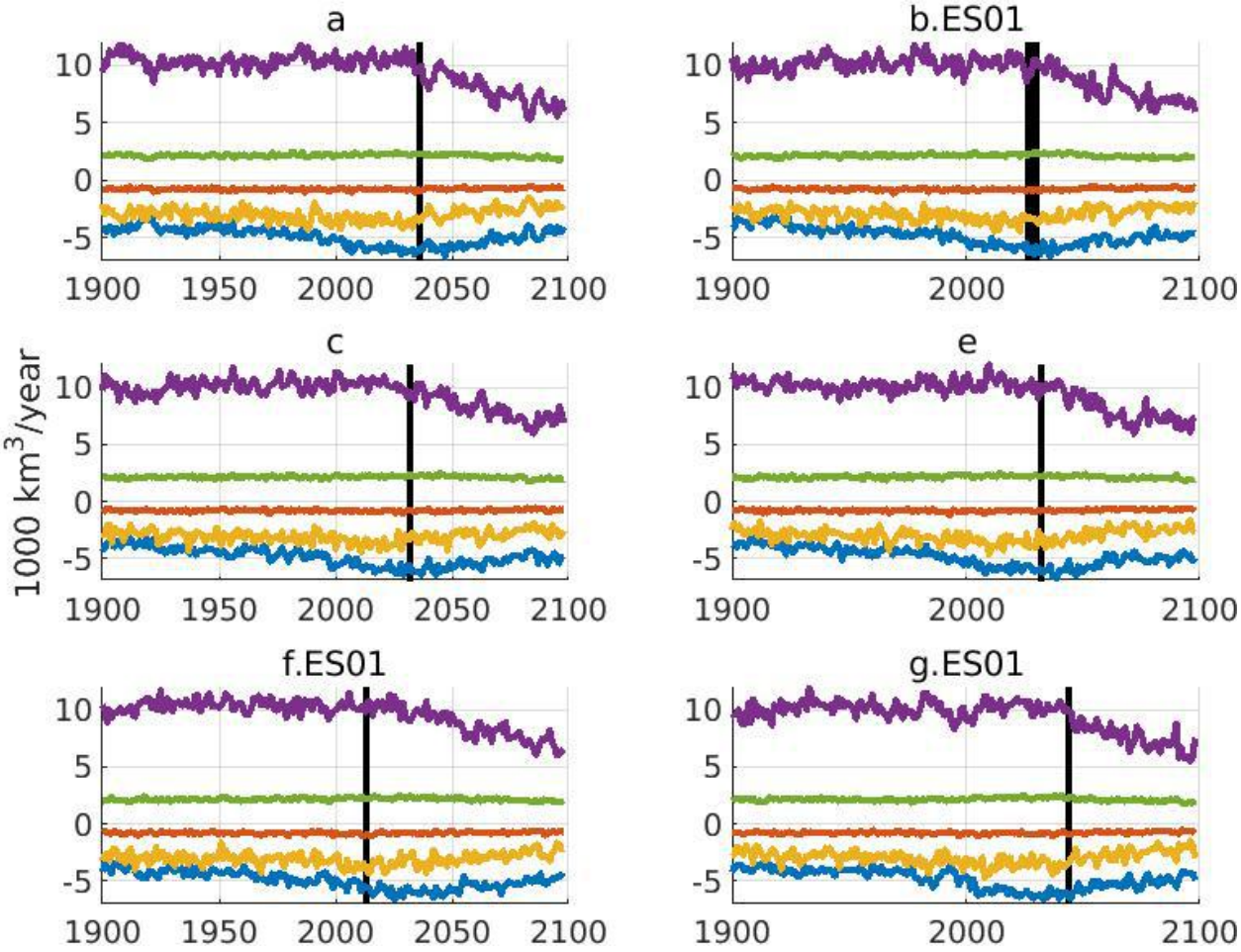

Figure 3.7: Thermodynamic processes. Purple) Basal growth. Green) Frazil formation. Red) Lateral melt. Orange) Surface melt. Blue) Bottom melt. The variables have been averaged yearly and spatially over the Arctic region in figure 3.2.

The remaining thermodynamic processes are surface and basal melt. They both increase in magnitude until the abrupt loss events and then decrease. It makes them good candidates

for causing the abrupt loss events. The surface melt starts at -2,700 km^3/a, decreases down to -4,500 km^3/a and then increases up to -2,400 km^3/a. The basal melt is more important in magnitude. It starts at -3,900 km^3/a, decreases down to -6,700 km^3/a and then increases up to -4,800 km^3/a.

We conclude that increased melt caused the rapid sea ice decline. We discarded the dynamic processes and the formation of new ice in the last two sections. The only process left is melt. Since it increases until the rapid decline and then decrease, they must have cause the rapid sea ice decline events. Both surface and basal melt are significant. In the next two sections, we look at the contributions from the different variables included in their calculation. In section 3.4.1, we study the surface melt. In section 3.4.2, we study the basal melt.

3.4.1 Surface melt

The surface melt is calculated from the difference between the surface fluxes, F_0, and the surface conduction, F_{ct},

$$\Delta h = \frac{F_0 - F_{ct}}{q_{top}}, \tag{3.1}$$

where q_{top} is the enthalpy of surface ice (Hunke and Lipscomb, 2010). The standard output of the CCSM3 does not include the enthalpy of the surface ice nor the surface conduction. It leaves only the surface fluxes to analyse.

Surface fluxes include sensible heat flux, latent heat flux, longwave radiation and solar or shortwave radiation. The most important heat fluxes are the shortwave and longwave radiations, as can be seen in figure 3.8. The shortwave radiation is fairly constant at 26.6 W/m^2. The longwave radiation decreases in strength. It starts at -25.8 W/m^2 and ends at -20.3 W/m^2. For the minor terms, only the sensible flux increases during the simulations. It increases from -1.5 W/m^2 up to 1.1 W/m^2. The latent flux is fairly constant at -4.2 W/m^2. The changes in longwave radiation and sensible heat flux are causing a major shift in surface interactions. Averaged yearly during the 20^{th} century, the net heat flux at the surface of the sea ice has a cooling effect. During the 21^{st} century, the net surface heat flux warms the sea

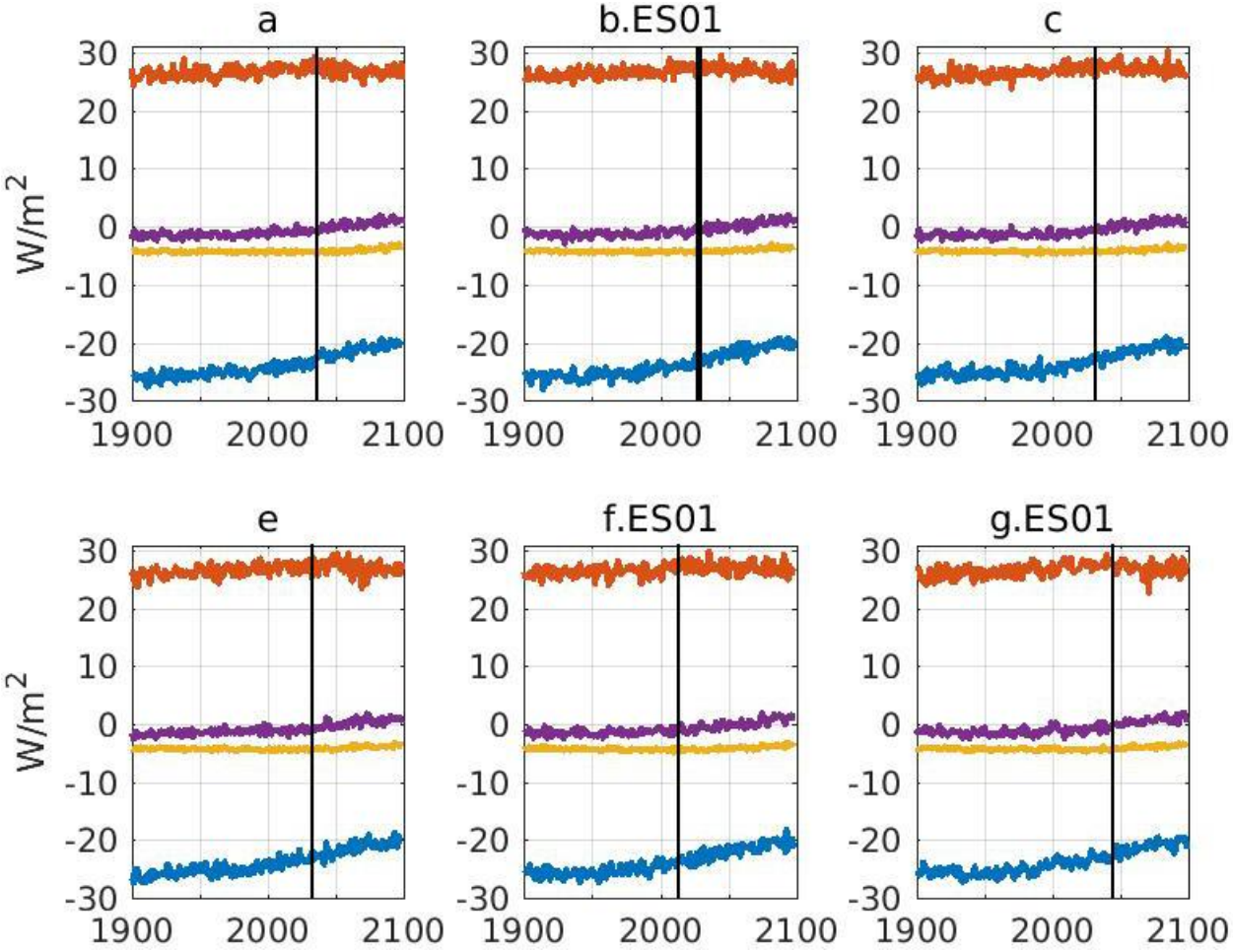

Figure 3.8: Surface fluxes affecting sea ice. Red) Solar radiation. Blue) Longwave radiation. Yellow) Latent heat flux. Purple) Sensible heat flux. All fluxes are averaged yearly and spatially averaged over the Arctic region in figure 3.2. The vertical lines depict the years of rapid September sea ice extent decline.

ice. It starts at -5.8 W/m^2 in 1900 and ends at 3.8 W/m^2 in 2100. We are interested in the sources of change in longwave radiation and sensible heat flux.

The changes in longwave radiation is caused by the increase in greenhouse gases. The longwave radiation is calculated as the difference between the absorbed and emitted longwave radiation;

$$F_{lw\,e} = \epsilon F_{lw\,a} - \epsilon \sigma_{SB} T_{surf}^4, \tag{3.2}$$

where ϵ is the emissivity of sea ice, $F_{lw\,a}$ is the longwave atmospheric radiation reaching sea ice, σ_{SB} is the Stefan-Boltzmann constant and T_{surf} is the temperature of the ice at its surface. The second term on the right hand side of equation 3.2 is the Stefan-Boltzmann law. The

atmospheric longwave radiation is affected by the increase in green house gases reflecting it back to the ground. This effect is more important than the one from increased sea ice surface temperature in the Stefan-Boltzmann law. Since the increase in radiation absorption is more important than the increase in emission, the resulting net longwave radiation increases.

The increase in sensible heat flux is caused by the increase in atmospheric temperature at the surface of the ice. The sensible heat flux is given by the temperature difference between the atmosphere and the sea ice,

$$F_s = C_s(\Theta_a - T_{surf}), \tag{3.3}$$

where C_s is a nonlinear turbulent heat transfer coefficient and Θ_a is the atmospheric surface potential temperature. The atmospheric temperature increased more than the sea ice surface temperature resulting in an increasing sensible heat flux. Both major changes in surface fluxes are now explained.

In summary, the surface melt is driven by surface fluxes. The net surface flux strictly increases during the simulations because the Arctic atmospheric temperature increases and the greenhouse gas effect is enhanced. Though, the surface melt decreases after the rapid loss events. This disparity is caused by the lack of sea ice. Even if the surface heat flux increases, there is less sea ice area to receive this heat. Hence the decrease of surface melt. This conclude our investigation of the surface melt. The second significant thermodynamic process is the basal melt.

3.4.2 Basal melt

Basal melt is calculated from the difference between the heat transferred from the ocean to the sea ice, F_{bot}, and the heat conduction at the ice base, F_{cb},

$$\Delta h = \frac{F_{cb} - F_{bot}}{q_{bot}}, \tag{3.4}$$

where q_{bot} is the enthalpy of basal ice. The standard output of the CCSM3 does not include the heat conduction at the ice base nor the enthalpy of basal ice. It leaves the thermal

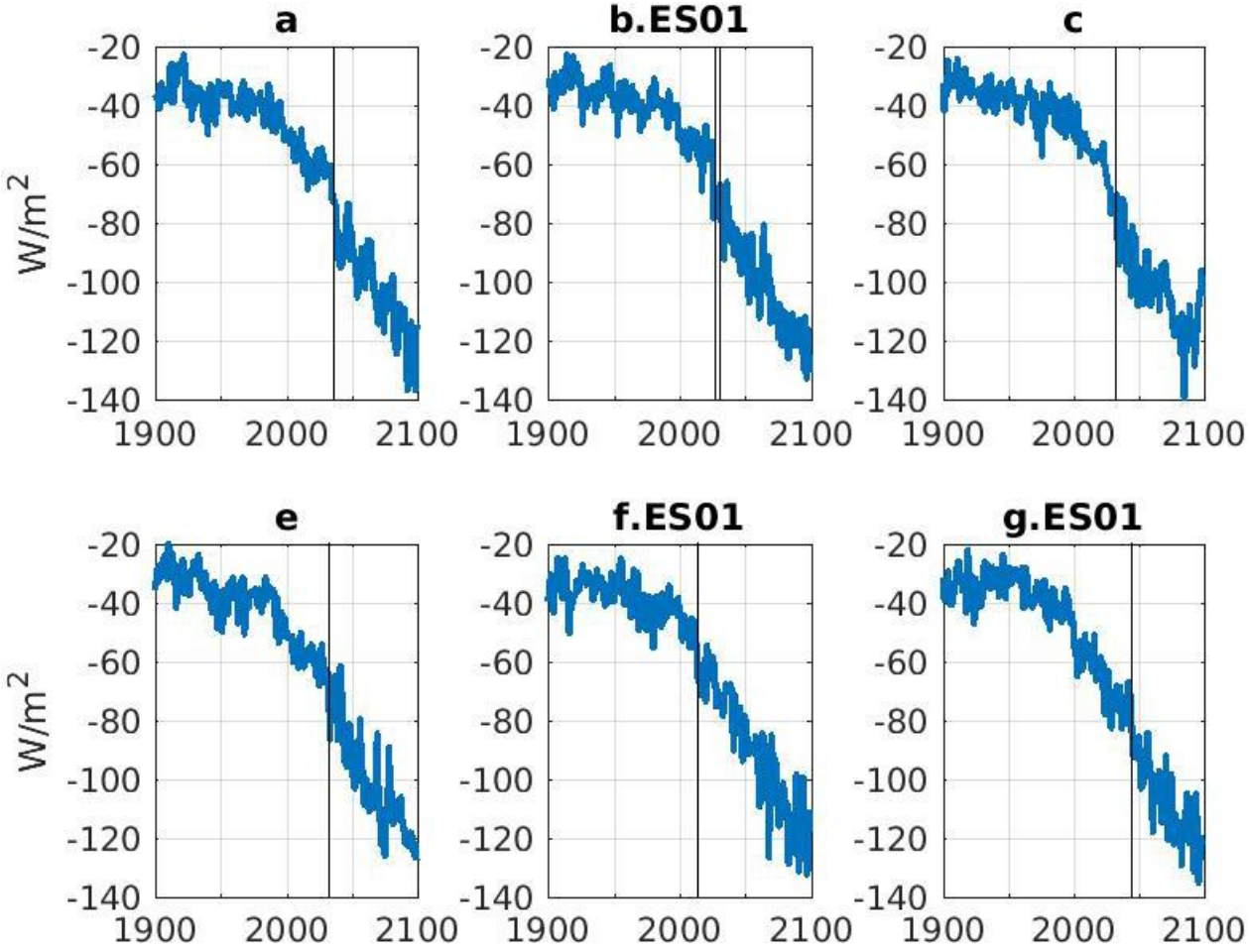

Figure 3.9: Yearly-mean turbulent heat flux between the sea ice and the ocean averaged over the Arctic Ocean. A negative value represents a loss of heat from the ocean to the sea ice. Vertical black lines represent the years of rapid September sea ice extent decline.

interactions between the ocean and the sea ice to analyse. It starts at -34 W/m^2 increasing in strength up to -117 W/m^2 by the end of the simulations, as can be seen in figure 3.9. This 350% increase represents a profound change of regime between the ocean and the sea ice. We are interested in which component or components of the heat flux between the ocean and the sea ice is at play here. But first, we want to know if the CCSM3 heat transfer from the ocean to the sea ice compares well to observations.

McPhee et al. (2003) recorded an averaged oceanic heat flux of 2.6 W/m^2 using a buoy deployed close to the North Pole that drifted through the Fram Strait. When the buoy reached the Yerkman Plateau (North of Svalbard), the oceanic heat flux reached values as high as 22 W/m^2. The sharp bathymetry and the absence of cold halocline layer led to a large ocean heat flux linked with tidal waves. Perovich et al. (1989) calculated an averaged

oceanic heat flux of 14 W/m^2 from a buoy moving through the Fram strait from December 14^{th} 1987 to January 2^{nd} 1988. By the end of December 1987, the buoy entered warm water and measured an ocean heat flux of 128 W/m^2. Using the 1975 Arctic Ice Dynamics Joint EXperiment (AIDJEX) data, Maykut and McPhee (1995) calculated a strong seasonal cycle of the ocean to sea ice heat flux with a yearly average of 5.1 W/m^2. The maximum values of the ocean to sea ice heat flux were 60 W/m^2 in August and almost zero in winter. Perovich and Elder (2002) observed values of ocean to sea ice heat fluxes of 2 W/m^2 during fall, winter and spring and values around 33 W/m^2 during the summer months. The heat exchange between the sea ice and the ocean produced by the CCSM3 do not relate well to observations.

The CCSM3 greatly overestimates the heat transfer from the ocean to the sea ice. Even the lowest value of 34 W/m^2 in 1900 overestimates all the observations. Heat fluxes such as the ones simulated during the last years of the 21^{st} century were observed only during a brief period when the buoy entered warm waters. The model computes such high heat fluxes averaged over the Arctic and yearly. The CCSM3 ocean heat flux to the sea ice is far too agressive. Though, this model is known to produce realistic sea ice compared compared to satellite observations. In order to obtain realistic sea ice, the extra heat from the ocean must be balanced somewhere else. We now study the variables used to compute this heat flux.

The heat flux from the ocean to the sea ice is calculated as:

$$F_{bot} = -\rho_w \cdot c_w \cdot c_h \cdot u_* \cdot (T_w - T_{fr}), \tag{3.5}$$

where ρ_w is the water density, c_w is the water heat capacity, c_h is the heat exchange coefficient, $u_* = \sqrt{|\tau_w|/\rho_w}$ is the friction velocity, $|\tau_w|$ is the norm of the shear stress given by $\mu_w \sqrt{\frac{\partial u}{\partial y}^2 + \frac{\partial v}{\partial x}^2}$ with μ_w being the ocean dynamical viscosity, T_w is the sea surface temperature, T_{fr} is the freezing temperature of the ocean set at $-1.8°$ C in the CCSM3. The only variables are the sea surface temperature and the friction velocity.

The sea surface temperature increases more and more rapidly, see figure 3.10. All the rapid sea ice declines happen at a temperature close to $-0.9°C$. The maximum sea surface temperature increase is of $8°C$ and is located over the Barents Sea. For unknown reasons to

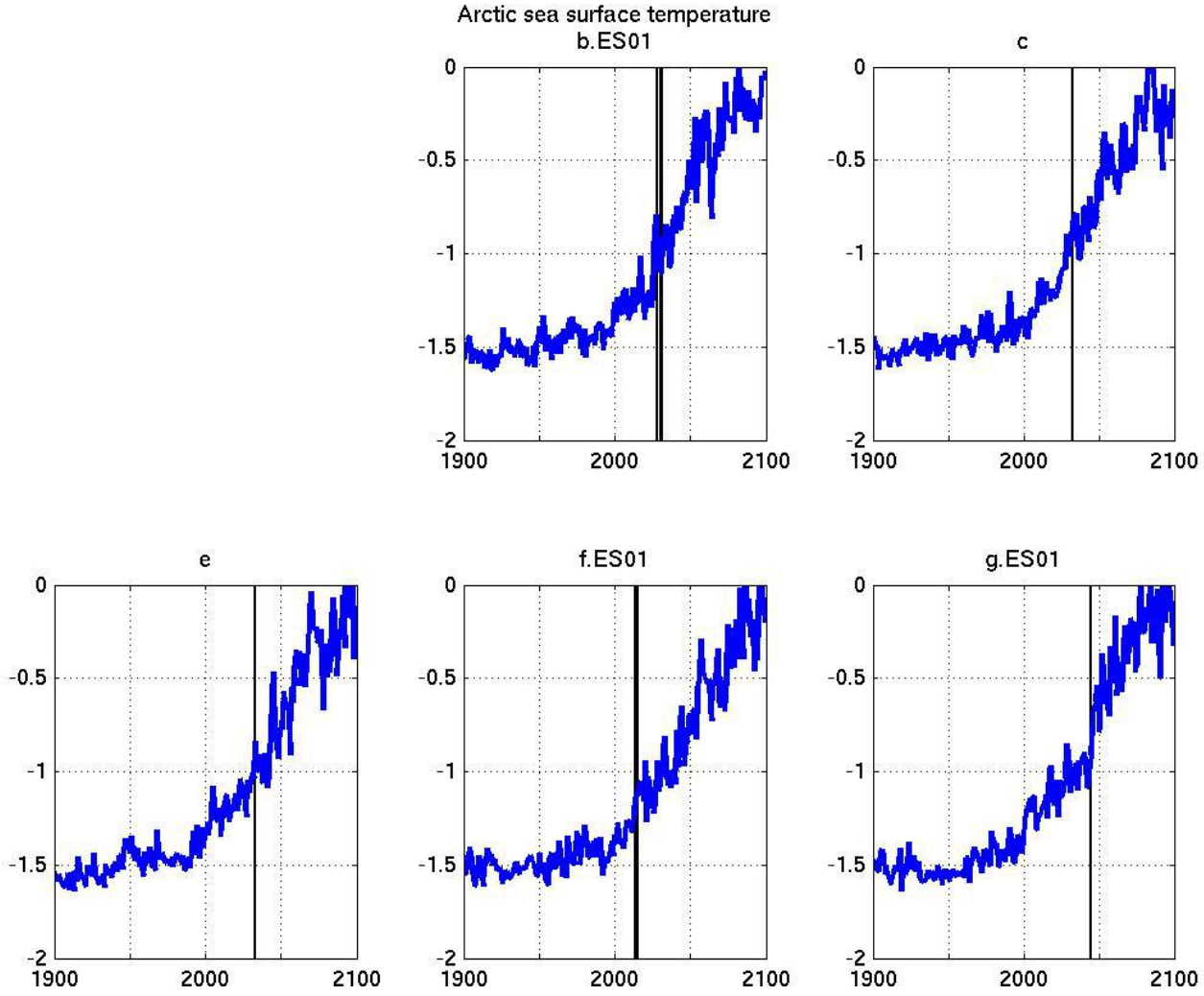

Figure 3.10: Yearly-mean sea surface temperature averaged over the Arctic Ocean in $°C$. Vertical black lines represent the years of rapid September sea ice extent decline.

us, the sea surface temperature data of simulation a is missing.

The friction velocity varies modestly over the simulations. It increases by 1.5% of its initial value until the rapid loss events. It then comes back to its initial value by the end of the simulations. Therefore, it is far less significant than the sea surface temperature.

We conclude that the basal melt is driven by sea surface temperature. The sea surface temperature increases appreciably over the full timespan of the simulations. Though, the basal melt decreases after the rapid loss events. This disparity can be explained by the lack of sea ice. Even if the amount of heat available for melting increases, there is not even sea ice to transfer it to. Hence, the decrease in basal melt.

3.5 Conclusion

The presented analysis of the abrupt loss of Arctic September sea ice extent is based on sea ice volume. In the CCSM3, sea ice volume decreases sooner and faster than the sea ice extent, respectively a loss of 40% and 8% between 1950 and 2000. During the years of the abrupt reductions of Arctic September sea ice extent, the sea ice volume decreases rapidly but not in a surprising way. The level of sea ice volume loss during the years of abrupt loss has been observed at earlier periods. The Arctic sea ice thinned until it reached a threshold where it could not thin much anymore and then started to lose coverage rapidly, hence the rapid loss of September sea ice extent.

The sea ice volume changes from dynamic and thermodynamic processes. The net dynamic process exports sea ice out of the Arctic region and the net thermodynamic process create the same amount. Dynamic processes include the sea ice transport through the gateways to the Arctic Ocean. Sea ice transport out of the Arctic Ocean mainly happens through the Fram Strait while the transport through the Barents sea opening, the Canadian Arctic Archipelago and the Bering Strait are negligible in comparisons. Thermodynamic processes include sea ice melt and formation. Formation is stable until the rapid loss events while the melt increases.

Table 3.1 describes the magnitude of the different processes during the early 20^{th} century before the rapid declines, at the time of the rapid declines, and by the end of the 21^{st} century after the rapid declines.

Processes	1900-1909	Events	2090-2099
Surface melt	-3	-3.5	-2
Bottom melt	-4	-6	-5
Lateral melt	-1	-1	-1
Basal growth	10	10	6
Frazil formation	2	2	2
Total Melt	-8	- 10.5	-8
Total formation	12	12	8
Thermodynamic	1.5	2.5	0
Transport	-4	-2	-1

Table 3.1: Sea ice volume changes due to melt and formation at three different periods: 1900-1909, at the abrupt loss events and 2090-2099. All volume changes are in 1,000 km^3/a.

Rapid loss events are caused by increased melt. Until the rapid loss of September sea ice extent events, melt increases, formation stagnates and transport decreases. Only the melt could have caused major modifications of the sea ice. Both surface and basal melt are important but the most significant changes are coming from the ocean.

The net surface flux is of $-5\,W/m^2$ in 1900 and increases up to $3.5\,W/m^2$ by 2100, a $8.5\,W/m^2$ gain over 200 years. It went from cooling the sea ice to warming it which is considerable. The bottom melt is driven by the turbulent heat flux from the sea ice to the ocean. It starts at $-20\,W/m^2$ in 1900 and ends at $-120\,W/m^2$ in 2100. The ocean heat transfer increased by $80\,W/m^2$ over 200 years. This change is caused by a sharp increase in sea surface temperature. This important increase in sea surface temperature is addressed in chapter 4.

Since the ocean fluxes contributed more to the sea ice melt than the surface fluxes and has undergone more significant changes, we conclude that it must be the primal cause for abrupt sea ice loss events. At this point, not a single process can solely explain the rapid loss of sea ice extent. We still agree with the conclusion of Holland et al. (2006a) which stated that the rapid loss of September sea ice extent is caused by years of high annual variability in conjunction with thinner sea ice.

4 Energy budget of the ocean component of the CCSM

As demonstrated in chapter 3, the ocean plays an important role in the sea ice mass balance. The surface ocean temperature is the most important factor controlling the amount of energy transferred from the ocean to the sea ice. The CCSM sea surface temperature is defined as the temperature of the top layer of the ocean model. We want to quantify the different elements affecting the top layer of the ocean.

Reconstructing the temperature equation would confirm that all the energy sources are accounted for and provide an accurate analysis. We refer to this exercise as closing the temperature-heat budget. In section 4.1, we present the derivation of the theoretical energy equation. We also present the temperature-heat equation we wish to reconstruct. Even if the CCSM3 solves that equation, it does not mean that the standard output allows the user to close the temperature-heat budget. As a matter of fact, the limited output offered by the CCSM3 leads to an incomplete budget. The details are presented in section 4.2. The CCSM version 4 offers an extended standard output. Therefore, we decided to close the temperature-heat budget for it. Unfortunately, it also leads to an incomplete temperature-heat budget. For that reason, we decided to study the CCSM4 codes. Our observations from the code can be found in section 4.4. Concluding remarks can be found in section 4.5.

A closing temperature-heat budget is a powerful tool. Without it, there is always the possibility of a miscalculation or misinterpretation of some of the terms. There is even the possibility of missing terms that could be important to the analysis. At the moment of writing this thesis, no indications on how it should be done are published. Many scholars would have greatly appreciated the presence of such a tool for their own research. This work has already been helpful to Auclair and Tremblay (2018), Nummelin et al. (2015) and Gervais et al. (2019, unpublished).

4.1 Energy equation

The CCSM is based on the Navier-Stokes equations and the energy equation for fluids. We could directly jump to the temperature or internal energy equation, however, it would be relevant to review the theoretical derivation of the energy equation.

The energy density (J/m^3) of a fluid can be split into three parts: kinetic, potential and internal. The kinetic energy density, K, is given by:

$$K = \frac{u^2}{2}, \tag{4.1}$$

where $u^2 = \vec{u} \cdot \vec{u}$ is the norm of the velocity vector (u, v, w) squared. The potential energy density, U, is given by:

$$U = g\, z, \tag{4.2}$$

where g is the gravitational constant and z is the height. In the case of an ideal gas, the internal energy is proportional to the temperature; $I = c_{p,v} T$ where $c_{p,v}$ is the heat capacity with constant pressure with the subscript p or with constant volume with subscript v. Taking the thermodynamic definition of the internal energy applied for an incompressible fluid ($\rho = \rho_0$, $dV = 0$ if the temperature is constant), we obtain

$$dI = c_v \cdot dT + \left[T \frac{\partial P}{\partial T} - P \right] dV = c_v \cdot dT \Rightarrow I = c_v \cdot T. \tag{4.3}$$

The internal energy is proportional to the temperature,

$$I = c_p\, T. \tag{4.4}$$

The total energy, E, of a volume V, is given by

$$E = \int_V \rho \, (K + U + I)\, dV. \tag{4.5}$$

where ρ is the density. The temporal change of the total energy must be equal to the energy flux integrated over the surface, S, of the volume:

$$\frac{\partial E}{\partial t} = - \oint_S \rho \, (K + U + I)\, \vec{u} \cdot \hat{n}\, dS, \tag{4.6}$$

where $\hat{n}$ is a unit vector perpendicular to the surface and pointing outward.

Other sources or transfer of energy includes: pressure work, diffusion and surface inter-

actions. The pressure work done on the system per surface area is given by the pressure, P, times the displacement, $\vec{x}$,

$$W = P\,\hat{n}\cdot\vec{x}. \tag{4.7}$$

Over a small time increment, the pressure can be considered constant leading to:

$$\frac{\delta W}{\delta t} = \frac{\delta(P\,\hat{n}\cdot\vec{x})}{\delta t} = P\,\hat{n}\cdot\frac{\delta\vec{x}}{\delta t} = P\,\hat{n}\cdot\vec{u}. \tag{4.8}$$

The total pressure work done per unit of time over the volume V with surface S is given by:

$$\frac{\Delta W}{\Delta t} = \oint_S P\,\hat{n}\cdot\hat{u}\,dS. \tag{4.9}$$

The diffusion, $\vec{q}$, can be written using Fourier's law for heat fluxes,

$$\vec{q} = -\chi\nabla T, \tag{4.10}$$

where χ is the thermal conductivity in $W/(m\,K)$. The total diffusive heat flux over a volume is given by:

$$\oint_S \vec{q}\cdot\hat{n}\,dS. \tag{4.11}$$

The last piece of the energy budget is the surface interactions: radiation, latent and turbulent heat fluxes. We define the surface interaction term, $\vec{F}$, as zero inside the volume V and equal to F at the top surface of the volume. The total energy income from surface interactions can then be written as:

$$\oint_S \vec{F}\cdot\hat{n}\,dS. \tag{4.12}$$

Note that some of the fluxes will be transmitted through the fluid (e.g. solar flux) and will contribute to F even if the surface of the volume V is not at the surface of the ocean.

Using the equations 4.5, 4.6, 4.9, 4.11 and 4.12, the energy equation can be written as:

$$\int_V \frac{\partial}{\partial t}\left[\rho\,(K+U+I)\right]dV = \oint_S \left[-\rho\,\vec{u}(K+U+I+\frac{P}{\rho}) - \vec{q} + \vec{F}\right]\cdot\hat{n}\,dS. \tag{4.13}$$

Using the divergence theorem on the right hand side of the equation, we obtain

$$\int_V \frac{\partial}{\partial t}\left[\rho\,(K+U+I)\right] dV = \int_V \nabla\cdot\left[-\rho\,\vec{u}(K+U+I+\frac{P}{\rho}) - \vec{q} + \vec{F}\right] dV. \tag{4.14}$$

The last equation is valid for any volume implying that the integrands must be equal, leading to:

$$\frac{\partial}{\partial t}\left[\rho\,(K+U+I)\right] = \nabla\cdot\left[\rho\,\vec{u}(K+U+I+\frac{P}{\rho}) - \vec{q} + \vec{F}\right]. \tag{4.15}$$

Equation 4.16 is the energy equation for a three-dimensional fluid.

Most models do not solve that equation directly. Usually, their advection scheme balances kinetic energy, potential energy and pressure,

$$\frac{\partial}{\partial t}\left[\rho\,(K+U)\right] = \nabla\cdot\left[\rho\,\vec{u}(K+U+\frac{P}{\rho})\right]. \tag{4.16}$$

Considering that scheme, the energy equation becomes the internal energy equation:

$$\frac{\partial}{\partial t}\left[\rho\,I\right] = \nabla\cdot\left[\rho\,\vec{u}I - \vec{q} + \vec{F}\right], \tag{4.17}$$

which can be rewritten in terms of the temperature,

$$\frac{\partial}{\partial t}\left[\rho\,c_p T\right] = \nabla\cdot\left[\rho\,c_p\,T\vec{u} - \vec{q} + \vec{F}\right]. \tag{4.18}$$

The ocean part of the CCSM, the POP model, solves this equation. Reconstructing this equation with the available output of the CCSM3 (or CCM4) is what we call closing the temperature-heat budget.

4.2 Temperature-heat budget for the CCSM3

In order to complete the temperature-heat budget for the CCSM3, we must retrieve every term of equation 4.18 as a variable output from the simulations. Note that all the output variables are averaged monthly. After a thorough inspection of the available variables, we found out that the vertical diffusion is missing. Nevertheless, it is possible to evaluate this

term as a residual of all the other terms. However, we need to balance the other terms satisfyingly first. If the other terms do not balance, the residual would not represent accordingly the vertical diffusion. In order to complete a budget without the vertical diffusion, we consider the vertically integrated budget over each grid column. That way, only the vertical diffusion at the ocean floor and at the surface of the ocean are left which are both zero. No ocean diffusion is allowed with the land or atmosphere. In appendix A, we describe how to access the code, the variables names and definitions, and the temperature-heat equation written with the variables.

All the terms of the vertically integrated column budget can be accounted for using the CCSM3 standard output. The vertically integrated column diffusion and advection of heat are available. The surface fluxes include evaporation, sensible heat, emitted and absorbed longwave radiation, melt, snow, ice runoff, frazil ice formation and absorbed short wave. The monthly mean temperatures are available but not their monthly temporal derivatives. We have to calculate it from the monthly mean temperature fields. The temporal derivate is done using the leapfrog scheme since it gave better results compared to forward and backward Euler schemes. This covers all the terms in equation 4.18.

We consider three regions to test the temperature-heat budget: the Global Ocean, the Arctic Ocean and the grid columns. We chose to study the simulation b30.030b.ES01 because it is the main simulation studied by Holland et al. (2006a). It is characterized by the longest and the most apparent rapid September sea ice extent decline. On a global scale, there is no input of energy from advection or diffusion since all the oceans are boarded by coast. Only the surface fluxes are bringing energy into the ocean peaking at 11 W/m^2 in February and -21 W/m^2 in July, see the top panel of figure 4.1. Note that the surface fluxes are cooling the ocean over the full course of year 1950. The budget error is of $\pm$ 2 W/m^2. It is then possible to evaluate the global vertical diffusion as a residual with an estimated error of $\pm$ 2 W/m^2. In many regions of the oceans, the vertical diffusion of heat is lower than 1 W/m^2. More specifically for the Arctic Ocean, Timmermans et al. (2008) measured lower than 1 W/m^2 vertical diffusive heat fluxes. Hence, it would be impossible to discern between actual vertical diffusive heat fluxes and the budget error.

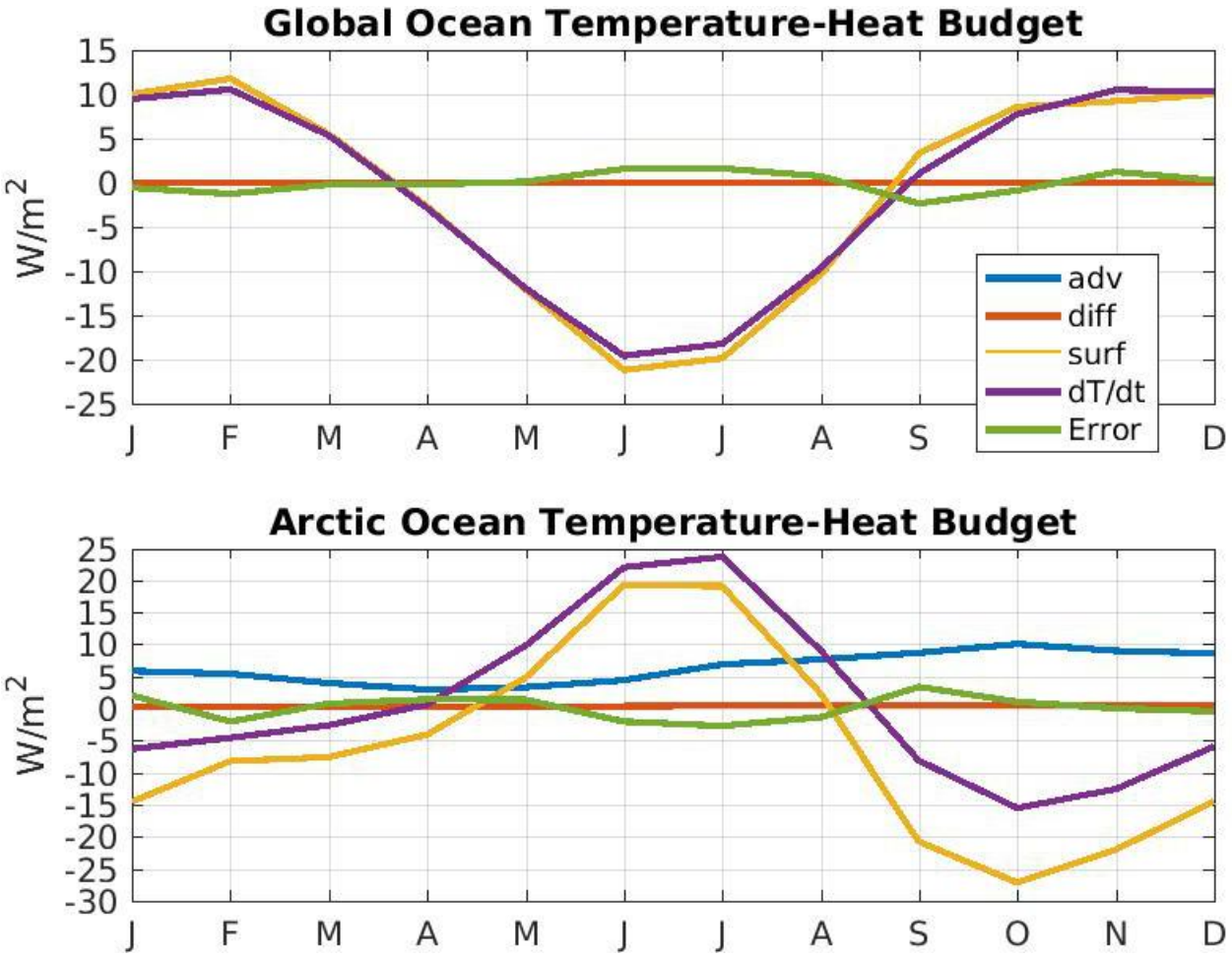

Figure 4.1: Temperature-heat budget for the Global Ocean and the Arctic Ocean of the CCSM3. Each data point comes from monthly mean variables.

Over the Arctic Ocean during summer, the surface fluxes are positive warming the ocean for four months peaking in June and July at 19 W/m^2, see the bottom panel of figure 4.1. During the winter months, the surface fluxes are cooling the ocean at a minimum of $-31\,W/m^2$ in October. The frazil ice formation releases up to 5 W/m^2 of heat during winter and nothing during summer (not shown). The advection of heat inside the Arctic Ocean ranges between 3 and 10 W/m^2. The diffusion has smaller values than 1 W/m^2. The budget error is of $\pm$ 3 W/m^2. Alike the global ocean, the budget error is higher than the expected vertical diffusive heat fluxes.

The averaged column error is of $\pm$ 150 W/m^2 as can be seen in figure 4.2. Though, the column error surpasses 1000 W/m^2 for certain columns. Some regions switch from a highly negative error to a highly positive error from a month to the next. North of Australia,

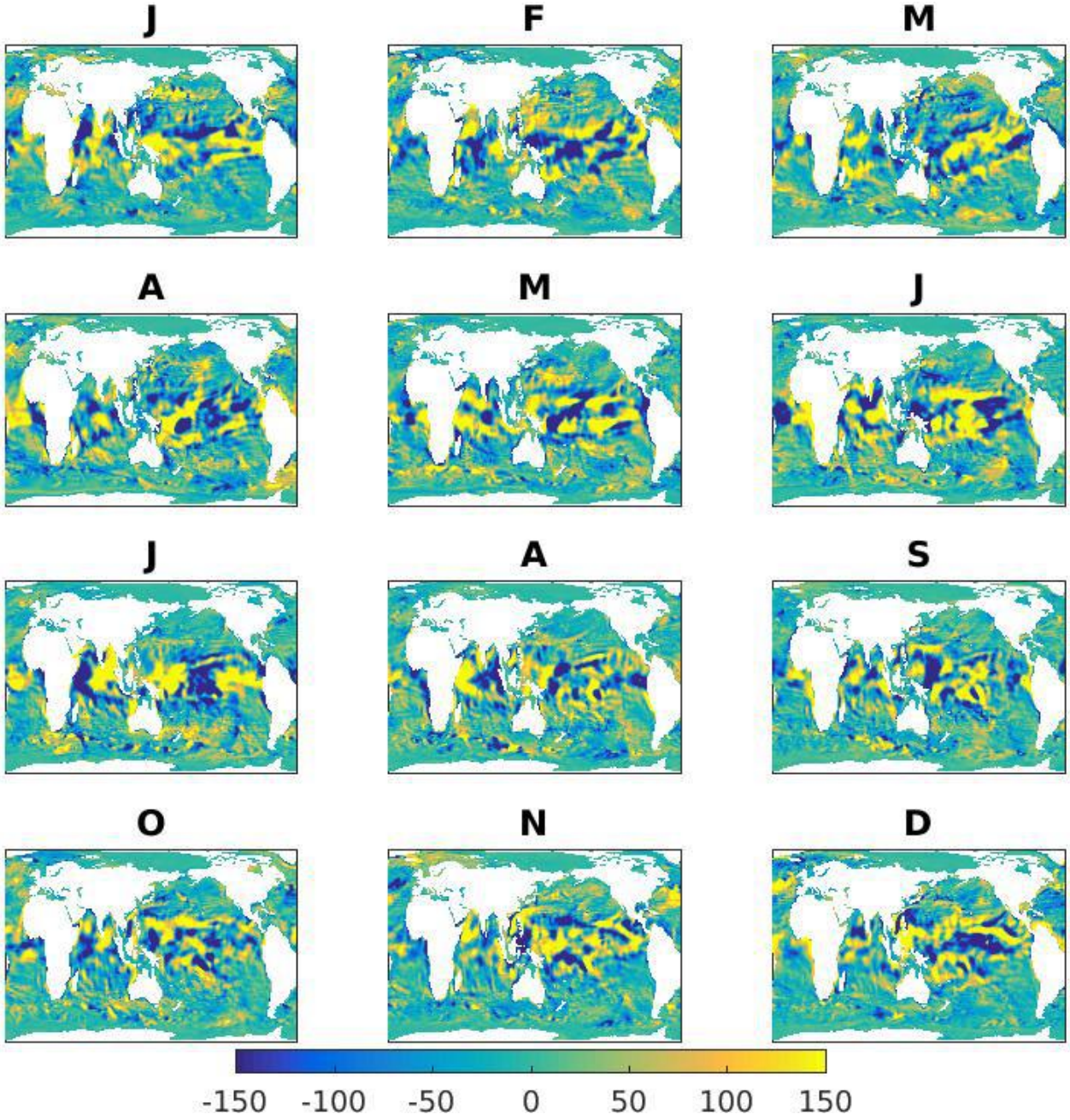

Figure 4.2: Temperature-heat budget of the ocean columns of the CCSM3 in W/m^2. Each graphs comes from monthly mean variables.

Indonesia and New Guinea, there is an area with an error over 150 W/m^2 in January dropping under -150 W/m^2 in February. Then, a combinations of columns with an error of 150 W/m^2 and -150 W/m^2 can be found in the same location for the months of March and April. The error becomes over 150 W/m^2 again in May and then under -150 W/m^2 in June, etc. The error fluctuates greatly spatially and temporally. The column error decreases significantly when averaged yearly though.

The calculated error of the temperature-heat budget is not satisfying using the output of the CCSM3. We believe the error comes from the temporal derivative from monthly mean temperature fields. We expect that the exact temporal derivative given by the difference of two instantaneous temperature snapshots reduces the error. For monthly mean fluxes, the temperature field at 0:00 the first day of the month and the temperature field at 0:00 the first day of the next month are required. But it is not possible with the CCSM3 output. Indeed, it is possible to retrieve restart files for the CCSM3 containing temperature snapshot every 10 years of January 1^{st} at 0:00. This temporal resolution is of no use for us since we want to follow rapid sea ice declines spanning over a period of less than 10 years. For that reason, we decided to turn to the CCSM version 4. This version stored restart files yearly providing temperature snapshot every first of January at 0:00.

4.3 CCSM4

The CCSM4 uses the same variables as the CCSM3 plus numerous more. How to access the code and the temperature-heat equation written with the variables names can be found in appendix B. A notable improvement is the addition of yearly temperature snapshots the 1^{st} of January at 0:00. It allows us to compute an exact temporal derivative for the temperature. Because of the temporal resolution of the temperature snapshots, we study yearly budgets. In the last section, we studied the monthly budgets for the CCSM3. Our analysis is based on the simulation b40.20th.track1.1deg.012 because it contains more output than usual runs being part of the Mother Of All Runs (MOAR). The studied period spans between 1950 to 1959.

Just as for the CCSM3, we analyzed the temperature-heat budget over three regions: the Global Ocean, the Arctic Ocean and the grid columns. The yearly global budget closes up to ± 0.4 W/m^2, see the top panel of figure 4.3. Again, the advection and diffusion terms sum up to zero. The yearly surface flux varies between -1 W/m^2 and 0.85 W/m^2. The temporal changes in temperatures-heat vary from -1.2 W/m^2 up to 1.4 W/m^2. The frazil ice formation is fairly constant over the years at 0.18 ± 0.01 W/m^2. These values are consistent with the yearly mean obtained from the results of the CCSM3.

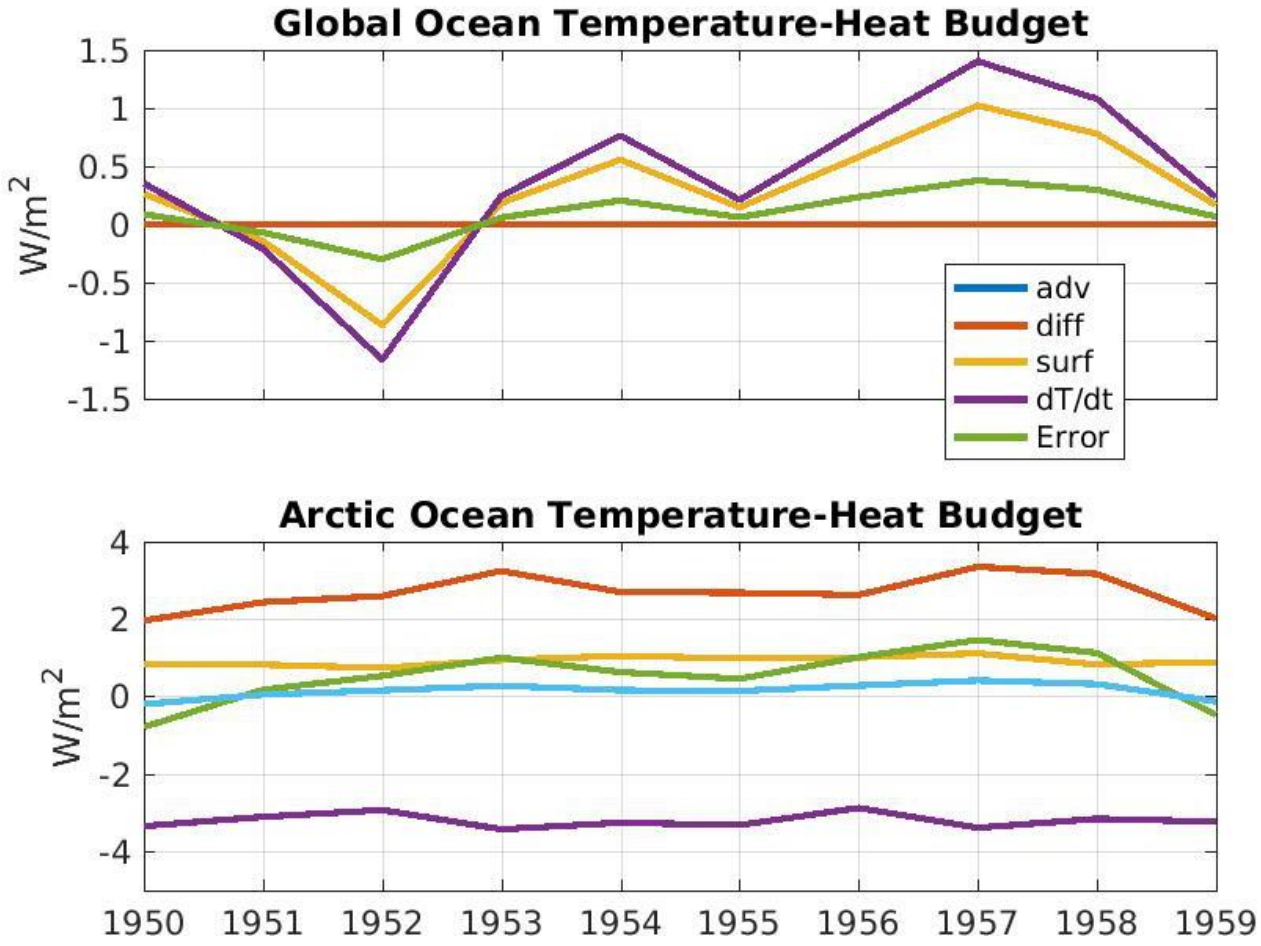

Figure 4.3: Temperature-heat budget for the Global Ocean and the Arctic Ocean of the CCSM4. Each data point has been averaged yearly.

The yearly Arctic budget closes up to $\pm 0.4\,W/m^2$, see the bottom panel of figure 4.3. The fluxes are almost constant through the ten-year period 1950-59. The surface flux is the most important energy sink at $-5\,W/m^2$. The advective flux is the highest energy income at $2.7\,W/m^2$ followed by the frazil ice production at $1.8\,W/m^2$ and then the diffusion of heat at $0.9\,W/m^2$. The internal energy temporal derivative ranges from $-0.8\,W/m^2$ to $1.4\,W/m^2$.

Even if the error of the budget closes satisfactorily globally and over the Arctic Ocean, it is not the case for the ocean columns, see figure 4.4. The column error can reach up to $150\,W/m^2$ and broad regions are at $\pm 50\,W/m^2$. It also changes from very positive to very negative between each year. For example, north of Australia, Indonesia and New Guinea, the error is $50\,W/m^2$ in 1953 then switches to $-50\,W/m^2$ in 1954 and back to $50\,W/m^2$ in 1955. It is an improvement compared to the CCSM3. The average error went from $\pm 150\,W/m^2$ for the CCSM3 down to $\pm 50\,W/m^2$ for the CCSM4 and the maximum error went from $1000\,W/m^2$

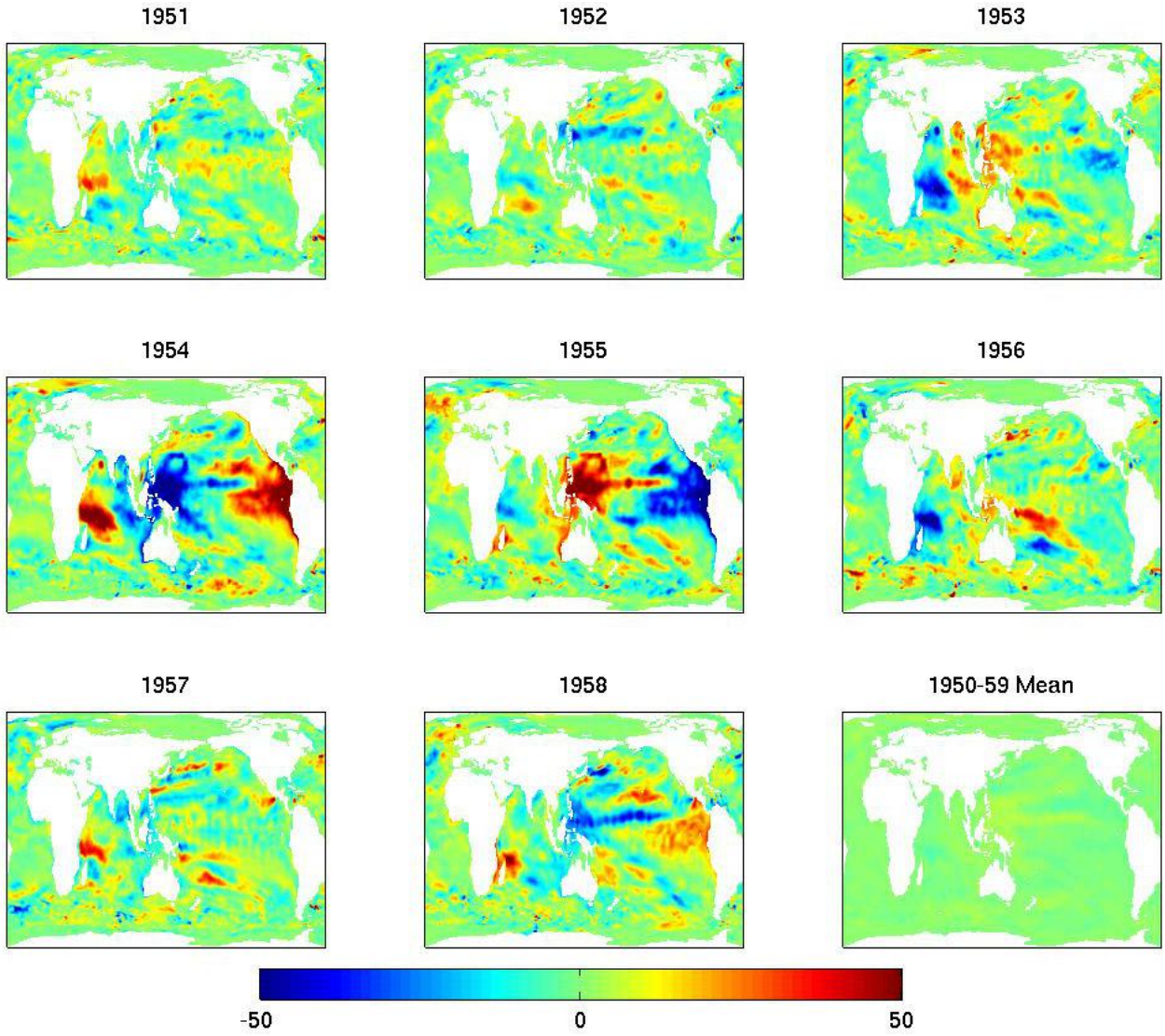

Figure 4.4: Temperature-heat budget of the ocean columns of the CCSM4 in W/m^2 for the years 1951 to 1958 and in the bottom right corner, the average error over 1950-59. Each graphs has been calculated from yearly averaged variables.

for the CCSM3 down to $150\,W/m^2$ for the CCSM4.

Once averaged over the decade, the column error shrinks down to $\pm 10\,W/m^2$ with the majority of the domain being at $\pm 1 W/m^2$. Since the model solves the temperature equation, it should be possible to close it up to machine accuracy using the right variables. The missing process or processes have the following properties: (1) they range between $\pm 150\,W/m^2$, (2) they cancel when integrated globally, (3) they cancels when integrated over the Arctic Ocean, (4) their value decreases significantly when averaged over a decade. After inspecting carefully the complete list of output variables, we conclude that the missing field is not included in

the standard output of the MOAR. In the next section, we delve into the CCSM4 code to investigate which physical process or processes might be missing.

4.4 CCSM4 coded temperature equation

The temperature equation of the CCSM4 adds the results of six subroutines: (1) horizontal diffusion, (2) advection, (3) vertical diffusion, (4) reset temperature, (5) KPP parameterization, (6) short wave radiation absorption. More details on every subroutines in appendix C. The horizontal diffusion is the first element of the temperature-heat budget being called. There are three diffusion schemes: laplacian, biharmonic and Gent-McWilliams. The simulation $b40.20th.track1.1deg.012$ used the Gent-McWilliams scheme (Gent and Mcwilliams, 1990). The CCSM calculates the horizontal diffusion of heat through a side of a cell as the product of the side area of the cell (A_{side}), the spatial derivative of the temperature perpendicular to the side area ($\frac{\Delta T}{\Delta x_\perp}$) and a diffusive coefficient (κ),

$$D = A_{side} \cdot \frac{\Delta T}{\Delta x_\perp} \cdot \kappa. \tag{4.19}$$

The diffusive coefficient includes conventional and Gent-McWilliams diffusive coefficients. The MOARs have more output which includes eastward and northward heat diffusion. Usually, only the vertically integrated divergence of heat diffusion is output, $\int (D_{west} - D_{east} + D_{south} - D_{north}) dz$.

The second element of the temperature-heat budget is the heat advection. It is output as the eastward, northward and bottom heat fluxes and also as the vertically integrated divergence of heat advection. The heat advection on a side of a cell is given by $Adv = A_{side} \cdot T_{side} \cdot u_{side}$.

The third element of the temperature equation is the vertical diffusion. It is calculated as the difference between the top and the bottom vertical diffusion, $(T_{bottom} - T_{top}) \cdot \kappa_{vert}$. For the surface layer, several surface interactions are added: evaporation, sensible heat, emitted and absorbed longwave, melt, snow and ice runoff. They are output separately or as a bundle with the shortwave radiation. The vertical diffusion is not part of the standard or MOAR

output.

The fourth element is the reset temperature process. When the ocean temperature goes under the freezing point, the model resets the ocean temperature back at the freezing point. The involved energy is used to form frazil ice. There is a variable for frazil ice formation in the standard output. However, nothing in the code seemingly ties this variable to what is calculated in the temperature equation. We will use the standard output frazil formation variable to cover this part of the temperature equation.

The fifth element of the temperature equation treats of vertical KPP mixing parameterization (Large et al., 1994). It is given by the product of all the surface forcings times a nonlocal diffusivity coefficient, $F_{surf} \cdot \kappa_{kpp}$. This nonlocal term is bewildering and is still misunderstood in the community though well accepted. It is based on boundary layers physics for the atmosphere, which is well developed, and adapted for the ocean. The divergence of KPP mixing is part of the standard output of the CCSM4 as KPP_SRC_TEMP. This variable was not present in our previous analysis whereas its vertical integration is nul. There is no mixing at the surface of the ocean or at the ocean floor.

The sixth, and last, element of the temperature-heat budget is the short wave absorption. It is part of the standard output and in a bundle including all surface fluxes excluding frazil ice formation.

All the parts of the temperature equation have been reviewed. There are outputs to calculate the results for five of the six elements of the temperature equation. Only the vertical diffusion is missing. A vertically integrated budget brings that term to zero. The only new process that was missing is the non-local KPP mixing parameterization. It does not alter the previous results since it is null when vertically integrated. In the end, all this code verification does not improve the internal energy budget done in the previous sections of this chapter.

4.5 Conclusion

The oceanic temperature has a considerable effect on the sea ice and the Arctic as shown in chapter 3. It is mandatory to understand the sources of heat affecting it if we want to

understand the future of the Arctic. To do so, a reconstruction of the temperature/heat equation is required. Our goal was to study all the energy sources affecting the first layer of the Arctic Ocean. This chapter showed the limit of the CCSM output to reconstruct the temperature/heat equation.

The CCSM3 is lacking the vertical diffusive heat fluxes and the snapshot temperature for an exact temperature temporal derivative. It is tempting to calculate the vertical heat diffusion as a residual of all the other fluxes. While it is possible to calculate the heat advection through a truncated column using eastward and northward advective heat fluxes, it is not possible for the diffusion since the variables are not output. All the horizontal and vertical diffusion would end up in the residual. The estimated error on that result would be the budget error, $3\,W/m^2$. Since the vertical heat fluxes are generally low, under $1\,W/m^2$ in the Arctic Ocean, we find this error too important.

The MOAR of the CCSM4 offers more options since the eastward and northward diffusive heat fluxes are output with the KPP vertical mixing. Yearly temperature snapshots allow for an exact calculation of the temporal derivative. Again, the vertical heat diffusion is not output. It is now possible to compute the mean vertical diffusion globally or over the Arctic Ocean with an estimated error of $0.4\,W/m^2$. Even if this error is acceptable in terms of vertical diffusion, we have not been able to satisfyingly close the internal energy budget for the columns. The column budget error reaches over $150\,W/m^2$ for both the CCSM versions 3 and 4. This uncertainty does not raise enough confidence to trust the estimated error of $0.4\,W/m^2$ without a reasonable explanation. We do not hold any convincing explanation for the extremely high column budget error. We regretfully stop our analysis of the first layer of the CCSM ocean model for that reason.

Even if it is not possible to study in detail each source of heat reaching the surface layer of the Arctic Ocean, it is possible to study the evolution of some sources. The next chapter is dedicated to the advective heat transport through the gateways of the Arctic Ocean.

5 Ocean advective heat fluxes through the gateways of the Arctic Ocean

The heat fluxes entering the Arctic Ocean are increasing (Beszczynska-Moller et al., 2011). There are intrusions of anomalously warm water (1) from the Atlantic (Holliday et al., 2008; Schauer et al., 2008), (2) from the Pacific (Woodgate et al., 2010), (3) over the Arctic shelves (Dmitrenko et al., 2010), (4) along the Arctic continental margin (Dmitrenko et al., 2008), (5) into the central Arctic (Polyakov et al., 2005) and (6) in the Canada Basin (McLaughlin et al., 2009). The waters entering the Arctic are warmer and penetrate further than before. They contribute to the Arctic warming which results in a decline in sea ice coverage, thickness, and volume (Kwok et al., 2008). Understanding the advective heat fluxes entering the Arctic Ocean is key to forecast the future of its sea ice. They are not studied extensively though. The scientific community usually focus on freshwater transport (Wijffels, 2001; Lehner et al., 2012) since it has a considerable effect on the global thermohaline circulation. Holland et al. (2006a) considered the total heat transport through the 55^{th} parallel. This chapter studies the heat transport to the Arctic region. We recall that this region is defined in figure 3.2. Our analysis treats separately the contribution from each gateway.

5.1 Introduction

As seen in chapter 3, the ocean plays an important role in the sea ice mass balance. For the six A1B SRES simulations of the CCSM3, the ocean heat transfer to the sea ice has increased more significantly than any other process. The temperature of the top ocean layer is the main factor of this heat transfer. Disappointingly, it is impossible to account for all the heat fluxes affecting the first layer of the ocean model of the CCSM as shown in chapter 4. It is possible to study available heat fluxes though.

In this chapter we study the advective heat fluxes through the Arctic gateways as simulated by the CCSM versions 3 and 4. The CCSM version 3 has 40 vertical levels and version 4 has 60 vertical levels. There has therefore been a reshaping of the Arctic Ocean gateways in the upgrade between the two versions. One may expect that these changes alter the simulated

fluxes through the gateways. Five of the six CCSM3 simulations of the SRES A1B presented in chapter 3 are studied. Simulation *a* does not have the correct output for this analysis. Along with the five simulations of the CCSM3, we also analyse the results coming from the five simulations of the CCSM4 under the RCP 6.0 scenario. The RCP 6.0 scenario is the closest scenario to the SRES A1B in terms of extra forcing. More informations concerning the scenarios can be found in section 2.4.3.

The next four sections treat the following gateways: Fram Strait (section 5.2), Barents Sea Opening (section 5.3), Canadian Arctic Archipelago (section 5.4) and Bering Strait (section 5.5). The locations of each gate are depicted in figure 3.2. Each section presents the bathymetry of the gateway, its heat transport, its volume transport and its temperature. Only the model mean is discussed: the average of the CCSM3 simulations and the average of the CCSM4 simulations. As will be seen below, the interannual variability of the models is less important than their trend; the variations between simulations are small compared to the trend evolution. The heat and volume transports are compared to observations. Finally, section 5.6 is a discussion of the results wherein we analyse the volume and heat transport budget of the Arctic Ocean.

Advective heat fluxes are calculated as:

$$F_{adv} = C_p \cdot \rho \cdot A \cdot T \cdot u, \tag{5.1}$$

where C_p is the heat capacity, ρ is the density, A is the area that the current goes through, T is the temperature of the current and u is its velocity. When it comes to advective heat fluxes, their effect such as warming or cooling is unclear. Only a complete budget bears meaningful information on warming or cooling. The Divergence theorem or Stoke's theorem states that

$$\int_V \frac{dT}{dt} dV = \int_A T(\vec{u} \cdot \vec{dA}). \tag{5.2}$$

Which can be rewritten for the Arctic Ocean and its gateways as

$$\int_{AO} \frac{dT}{dt} dV = \left[\int_{Fram} + \int_{BSO} + \int_{CAA} + \int_{Bering} \right] T(\vec{u} \cdot \vec{dA}). \tag{5.3}$$

One could study the Fram Strait advective heat fluxes extensively but could never draw conclusion in their effect on the Arctic Ocean. The cooling or warming of the Arctic Ocean is given only from the full integration over all the gateways.

The work in this chapter uses the usual definition of the advective heat flux as in equation 5.1[3]. This heat flux concord with the the total meridional heat transport diagnostic[4]. It also gives the exact same results as in Auclair and Tremblay (2018). We keep in mind the complications presented in the last paragraphs by comparing the relative strength of the different heat fluxes, avoiding any speculations on how much warming or cooling they cause.

5.2 Fram Strait

As seen in chapter 3, the Fram Strait is the main location where sea ice is exported out of the Arctic Ocean. Its shape is presented in figure 5.1. The reshaping of the Fram Strait in the CCSM4 made it shallower and narrower. Its maximum depth is 2500m for the CCSM3 and 2075m for the CCSM4. The total area of the Fram Strait is 361 km^2 for the CCSM3 and 291 km^2 for the CCSM4 which represents a difference of 20% of the CCSM3 area. From observations, the Fram Strait has a plateau 2500m deep expanding over 200 km (Beszczynska-Moller et al., 2011). In the CCSM3, the Fram Strait is not wide enough at the bottom compared to observation. In the CCSM4, the Fram Strait is not wide enough at the bottom and is too shallow compared to observations.

The yearly advective heat flux through the Fram Strait ranges between 2 TW and 20 TW averaging at 9 TW for both the SRES A1B and the RCP 6.0 during the 20^{th} century. This can be seen in the first row of figure 5.2. Over the 21^{st} century, the advective heat flux of the SRES A1B simulations decreases rapidly at a rate of -0.35 TW/a ending at -25 TW. The heat flux from the RCP 6.0 simulations increases steadily at 0.05 TW/a ending at 15 TW (see below for explanation). Schauer and Beszczynska-Moeller (2009) measured a mean advective heat flux of 36±6 TW between 1997 and 2009 from moorings. Cuny et al. (2005) measured 29 TW during the years 1980-2005. During the period 1980-2010, the mean heat transport is 8 TW for the CCSM3 and 9 TW for the CCSM4. The maximum values of the different

[3]We use the variables UET and VNT.
[4]Variable NHeat.

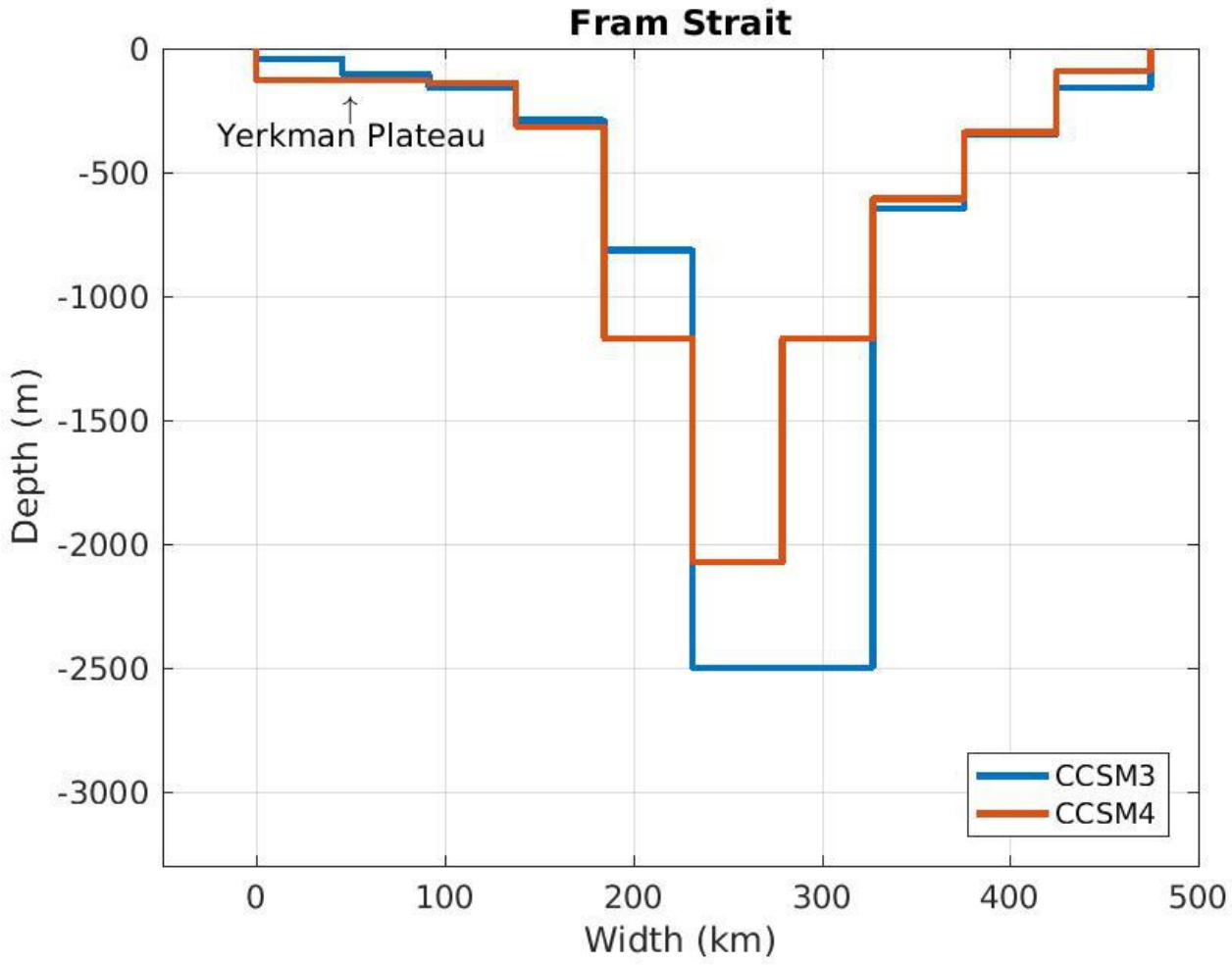

Figure 5.1: Bathymetry of the Fram Strait for the CCSM version 3 in blue and version 4 in red. The Yerkman Plateau is located on the left side (west) of the Fram Strait. Completely on the left (west) is Greenland and on the right (east) side is Svalbard.

simulations are under 20 TW. The simulated heat transport through the Fram Strait is too weak compared to observations. To understand the evolution of the heat transport, we need to study the inflow and outflow volume transport and temperature.

The simulated total volume transports through the Fram Strait are negative meaning that more water exits the Arctic Ocean through the Fram Strait than enters. They steadily increase in magnitude as can be seen on the left plot of the second row of figure 5.2 . It starts at -4.7 Sv and ends at -5.7 Sv for the CCSM3. For the CCSM4, it starts at -1.4 Sv and end at -2.1 Sv. Schauer et al. (2008) measured -2.0±2.7 Sv between 1997-2007 while Rudels et al. (2008) obtained -1.7 Sv from 1980 to 2005. For the years 1980-2010, the CCSM3 simulated -5 Sv and the CCSM4 -1.8 Sv. The CCSM3 and the CCSM4 simulations agree

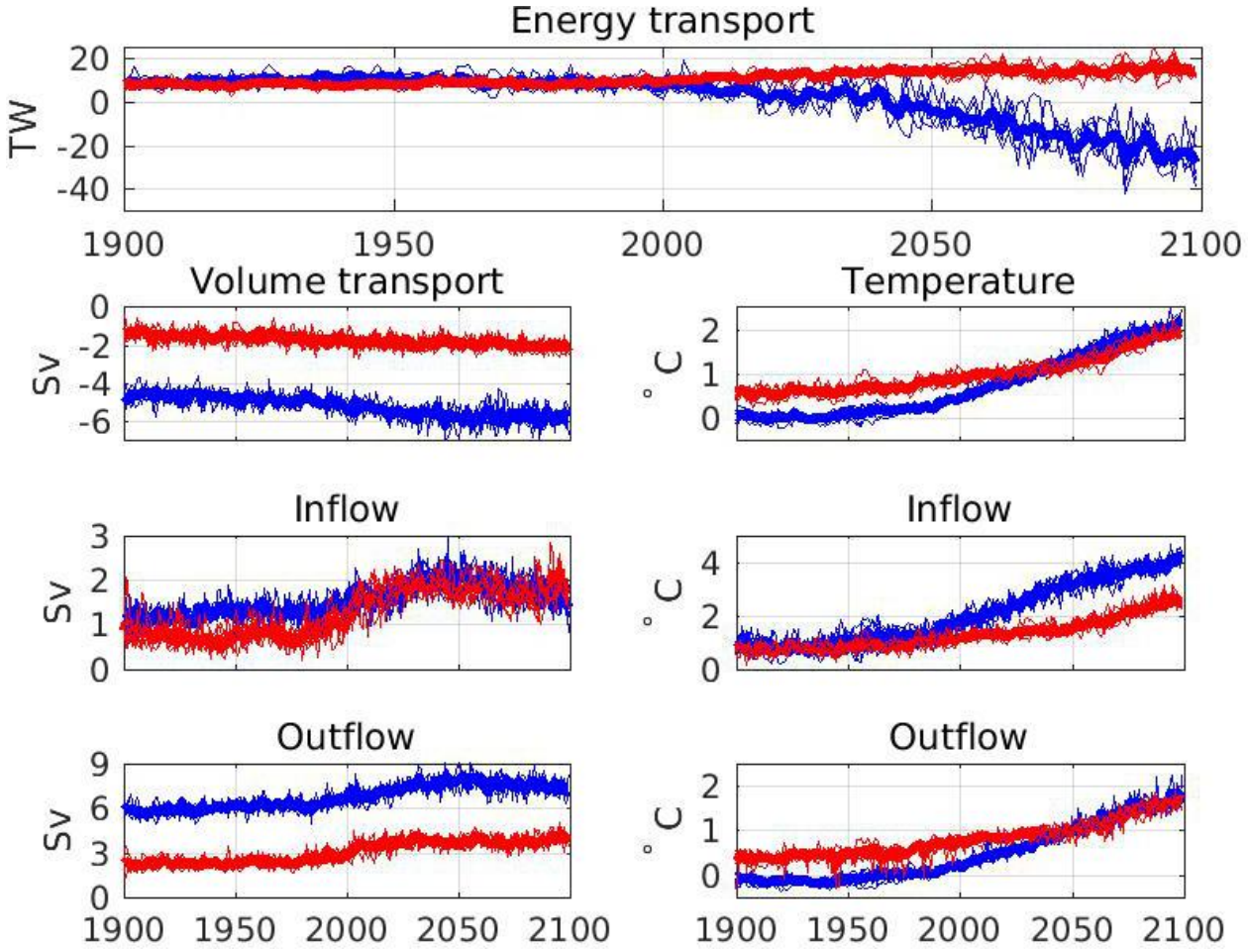

Figure 5.2: Fram Strait heat transport in terawatts (TW), volume transport in Sverdrup (Sv) and temperature in degree Celsius ($°C$) for the CCSM3 in blue and the CCSM4 in red. Each simulation is represented by a thin line, and the model mean is represented by a bold line. The data for volume transport and temperature are presented as follows: averaged over the gateway (second row), averaged over the inflow region (third row), averaged over the outflow region (fourth row).

with measurements.

The Fram Strait inflow has three phases, see the left plot of the third row of figure 5.2. For the CCSM3, the first phase starts at 1.1 Sv and increases at a pace of 0.0025 Sv/a until 1980. The second phase consists of a rapid increase of 0.01 Sv/y reaching 2.4 Sv by 2050. During the third phase, the inflow through the Fram Strait decreases steadily down to 1.5 Sv. The first phase of the CCSM4 inflow starts with a plateau at 0.7 Sv. The second phase is made of a rapid increase up to 2 Sv by 2050. The third phase is a plateau at 1.8 Sv.

The simulated outflows follow a similar three-phases design, see the left plot of the fourth row of 5.2. First, the CCSM3 outflow increases slowly from 5.9 Sv in 1900 up to 6.2 Sv in

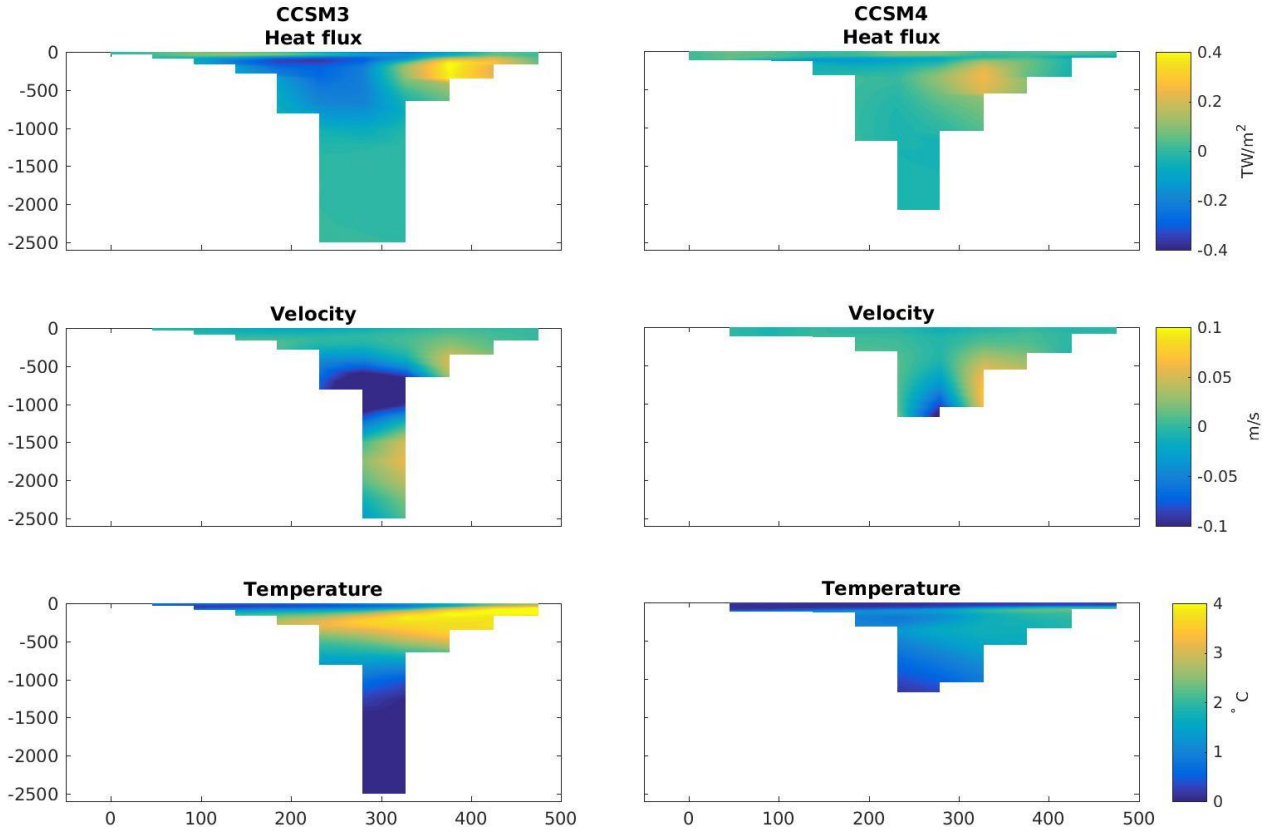

Figure 5.3: Fram Strait spatial variations in heat flux, velocity and temperature. The left column is dedicated to the CCSM3 and the right column is dedicated to the CCSM4. The variations are calculated from the difference between the 2050-2099 average and the 1900-1950 average. The depth axis is in metres and the width axis is in kilometres.

1980. Second, it increases rapidly until 2050 reaching 8.2 Sv. Third, it decreases down to 7.2 Sv by 2100. The first phase of the outflow of the CCSM4 is a plateau at 2.3 Sv. The second phase consists of a rapid increase up to 4.2 Sv by 2030. The third phase is a plateau at 3.8 Sv. The outflow increase is more important in the CCSM3 than the CCSM4.

The simulated temperatures of the inflow and outflow increase steadily, see the three plots on the second column of figure 5.2 from the second to the fourth row. The temperatures of the inflow of both the CCSM3 and CCSM4 are at $1°C$ in 1900 increasing up to $4.1°C$ for the CCSM3 and $2.6°C$ for the CCSM4 by 2100. The outflows are at $-0.1°C$ in 1900 for the CCSM3 and $0.4°C$ for the CCSM4 both increasing up to $1.7°C$ by 2100. The mean ocean temperature over the Fram Strait starts at $0.07°C$ for the CCSM3 and $0.6°C$ for the CCSM4. They both increase over the whole simulation ending close to $2°C$.

The CCSM3 and the CCSM4 simulated an increased heat flux west of Svalbard along the

West Spitsbergen Current, as can be seen on the first row of figure 5.3. The intensification in the CCSM3 is more important than in the CCSM4. A decrease of similar magnitude occurs over the location of the East Greenland Current. The decrease is more apparent close to the surface but it reaches down 800m deep in the CCSM3. In the CCSM4, the decrease spreads over a thin line close to the ocean surface.

Figure 5.3 shows the results from all the simulations and the model means as bold lines. All simulations from a same model behaves in a similar manner. The model trend is well defined. The differences between the different simulations or the model internal variability are smaller than the trend. Hence, the study of the model average represents adequately the model behaviour. For that reason, only the model average is studied.

Both models predict an increase in velocity over the West Spitsbergen Current and an increased outflow 1000m deep, see the centre plots of figure 5.3. The CCSM3 simulated a second important increase in velocity 1800m deep. Note that the gate shape presented for the heat fluxes is not the same as the velocity gate shape. The velocity field is defined on the northeast corner of the cell resulting in a narrower gate. For example, consider a two cell gate such as presented in figure 5.4. The first cell has a defined temperature and velocity. The second cell has a defined temperature but its side ends on the wall of the gate which sets the velocity to zero. The two temperature cell gate is a one velocity cell gate. Hence the narrower shape of the gate for the velocity fields. The spatial graphs for the temperature increase were made on the same shape as the velocity fields for an easier comparison.

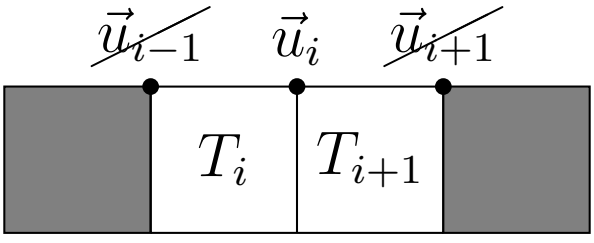

Figure 5.4: Example of a horizontal two cell Arakawa B-grid bordered by land. The ocean temperature of the second and third cells is defined while the temperature of the first and fourth cells is undefined since they are land cell. Only the second cell has a non-zero velocity. The first and third cell velocity ends on land and is defined as zero. The velocity of the fourth cell is undefined since there is no water bordering it.

The region where the temperature increases is located at a depth of about 500 meters close to Greenland and is wider to the east, see the bottom plots of figure 5.3. The temperature increase is more important in the CCSM3 than the CCSM4. The East Greenland Current of the CCSM3 intensifies greatly over the length of the simulation while the West Spitsbergen Current increases less resulting in a dramatic decrease of the value of the heat flux. The CCSM3 and the CCSM4 simulated very different outcomes for the Fram Strait.

The important features of the Fram Strait are (1) a positive heat transport during the 20^{th} century, (2) a massive decrease in heat transport for the CCSM3 and (3) a slight increase for the CCSM4. For the CCSM3, the positive heat transport through the first simulated century arises from the temperature of the outflow being close to zero contributing almost nothing to the heat transport. The inflow is the only source of heat transport with a positive temperature. For the CCSM4, the positive heat transport cannot be understood from the volume transport and the temperature plots. The heat transport is calculated as the volume transport multiplied by the temperature at each time step and then averaged, $\overline{u\,T}$. The volume transport and temperature presented in figure 5.2 are yearly means. The difference from both calculations, $\overline{u\,T} \neq \overline{u}\,\overline{T}$, leads to a positive heat transport in the CCSM4. The observed massive decrease of heat transport through the Fram Strait in the CCSM3 is explained by an increased outflow of up to 2 Sv with a $2°C$ temperature increase over 200 years for yearly average data. The inflow of the CCSM3 is too weak in comparison. It cannot stop the decrease of heat transport even if its temperature increased by $3°C$. The slight heat transport increase in the CCSM4 comes from a more important increase of the inflow than the outflow, with their temperature increasing similarly. When comparing the simulations to the observations, the heat fluxes from the CCSM3 and 4 are too weak but the total volume transport compares well to measurements.

5.3 Barents Sea Opening

The Barents Sea Opening starts on the east side of Svalbard, goes over Novaya Zemlya Island and over the tight opening between the Barents Sea and the Kara Sea, leading to Russian soil. The bathymetry of the Barents Sea Opening considered in this study is shown in figure 5.5.

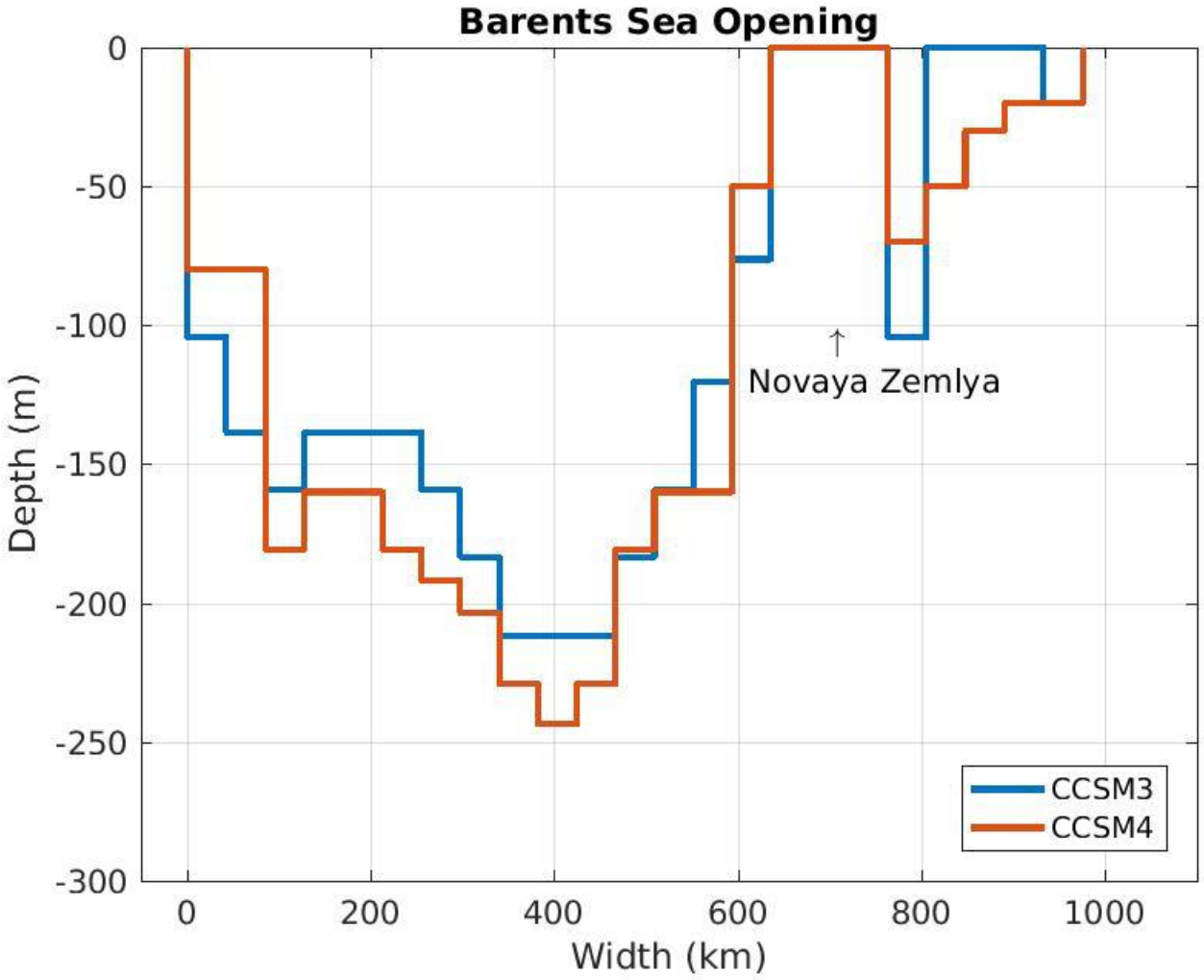

Figure 5.5: Bathymetry of the Barents Sea Opening for the CCSM version 3 in blue and version 4 in red. The location of Novaya Zemlya island is showed. On the left side (west) is Svalbard. On the right side (east) is Russia.

The CCSM4 cross-section of the Barents Sea Opening is very similar to the CCSM3, with the CCSM4 seafloor reaching slightly deeper. The total area of the Barents Sea Opening is 104 km^2 for the CCSM3 and 114 km^2 for the CCSM4 with a maximum depth of 212 m and 244 m respectively.

The advective heat flux through the Barents Sea Opening of the CCSM3 starts at 25 TW and increases until 1980 at 0.24 TW/a, see the first row of figure 5.6. From 1980 up to 2070, it increases rapidly at 1.2 TW/a. For the remaining of the century, it increases at 0.6 TW/a ending at 147 TW. The heat flux of the CCSM4 starts at zero and is stable until 1980 where it increases at a rate of 0.2 TW/a ending at 29 TW. Skagseth et al. (2008) and

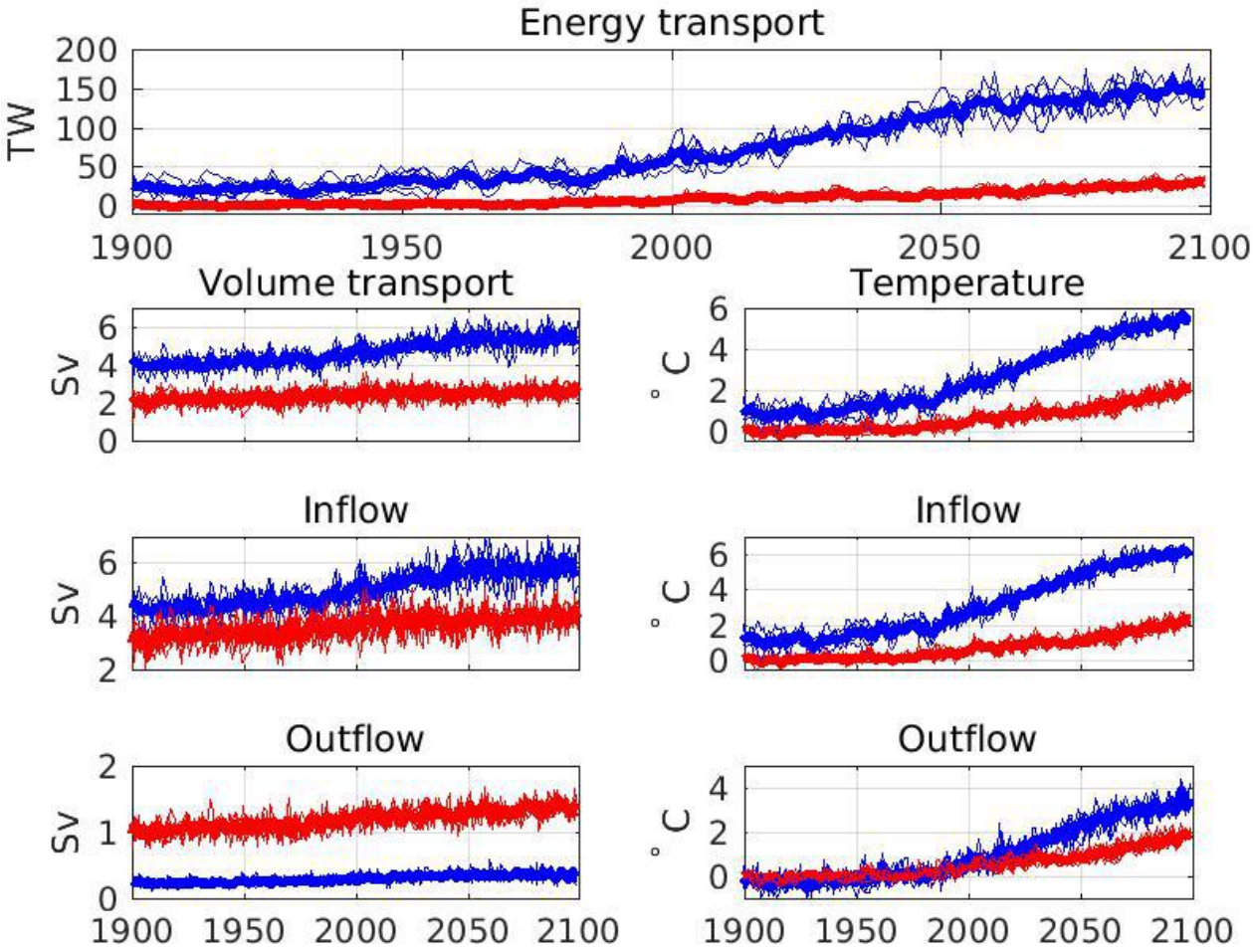

Figure 5.6: Barents Sea Opening heat transport in terawatts (TW), volume transport in Sverdrup (Sv) and temperature in degree Celsius ($°C$) for the CCSM3 in blue and the CCSM4 in red. Each simulation is represented by a thin line, and the model mean is represented by a bold line. The data for volume transport and temperature are presented as follows: averaged over the gateway (second row), averaged over the inflow region (third row), averaged over the outflow region (fourth row).

Smedsrud et al. (2010) measured advective heat fluxes entering the Barents Sea between 50 and 70 TW between 1997 and 2007. The CCSM3 simulated 60 TW during the same period while the CCSM4 simulated 8 TW. The CCSM3 agrees with the observations, whereas the CCSM4 simulated far too weak heat transport. Note that the moorings which provided the observations are not located at the same place as the Barents Sea Opening defined in this thesis. The moorings link Svalbard directly to Norway while the gateway defined here goes to Russia. Smedsrud et al. (2010) showed that over that region a large loss of ocean heat is lost through sensible heat, latent heat and longwave radiation.

The total amount of water through the Barents Sea opening starts at 4.1 Sv and ends at

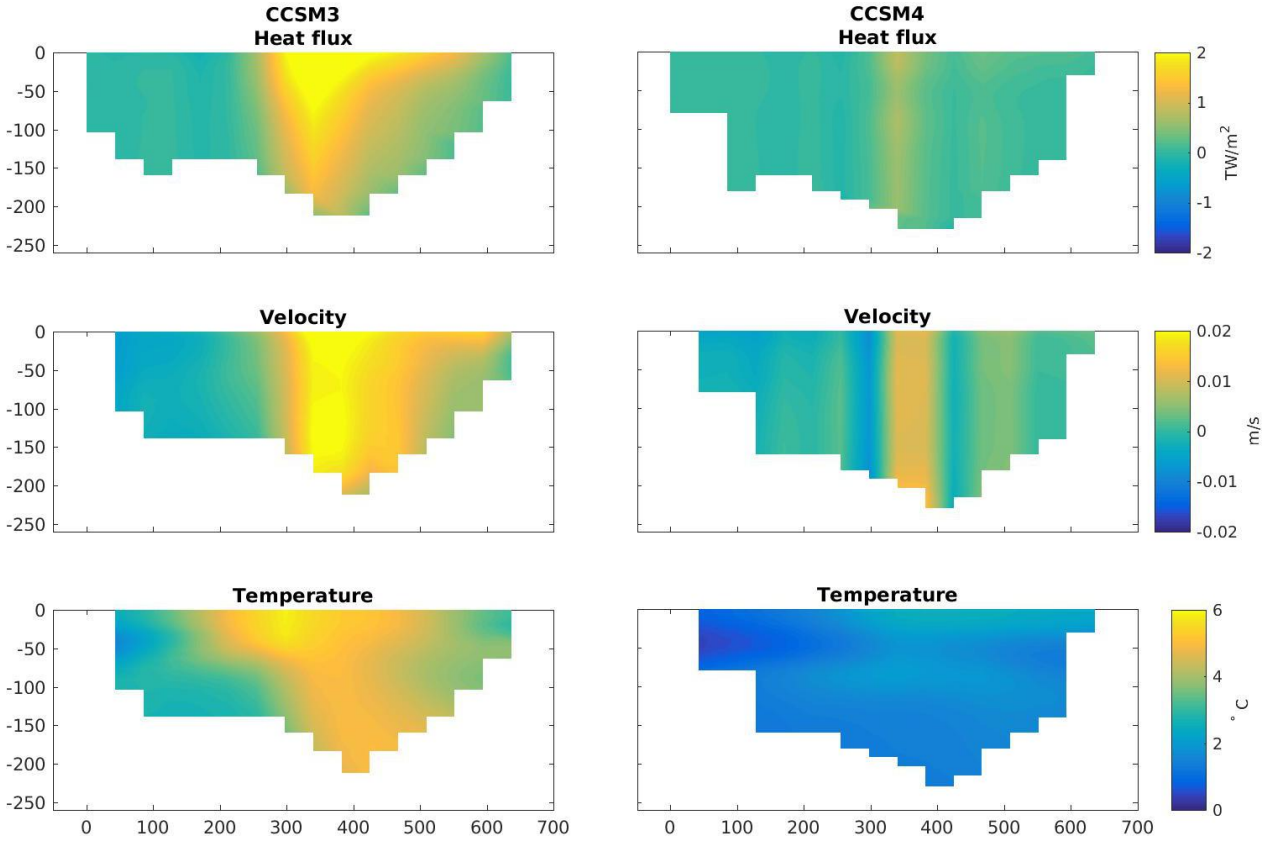

Figure 5.7: Barents Sea Opening spatial variations in heat flux, velocity and temperature. The left column is dedicated to the CCSM3 and the right column is dedicated to the CCSM4. The variations are calculated from the difference between the 2050-2099 average and the 1900-1950 average. The depth axis is in metres and the width is in kilometres. Note that the colour axis changed from figure 5.3.

5.4 Sv for the CCSM3 compared to 2.1 Sv and 2.6 Sv for the CCSM4, as can be seen on the left plot of the second row of figure 5.6. Skagseth et al. (2008) and Smedsrud et al. (2010) observed a mean volume transport through the Barents Sea Opening of 2 Sv/a between 1997-2007. During the 1997-2007 period, the total volume transport of the CCSM3 and CCSM4 simulations are 4.7 Sv and 2.5 Sv respectively. The volume transport of the CCSM3 is too large compared to measurements. The CCSM4 volume transport is more in line with measurements.

The volume of water entering the Arctic Ocean through the Barents Sea Opening increases steadily for both the CCSM3 and the CCSM4, see the left plot of the third row of figure 5.6. It starts at 4.3 Sv for the CCSM3 and increases up to 5.8 Sv by 2100. For the CCSM4, it starts at 3.1 Sv and ends at 4 Sv. The outflow of the CCSM3 through the Barents Sea

Opening is negligible compared to the inflow, see the left plot of the fourth row of figure 5.6. It starts at 0.25 Sv in 1900 and ends at 0.33 Sv in 2100. The outflow of the CCSM4 is more important starting at 1 Sv and ending at 1.3 Sv.

The temperature increases non-linearly over the Barents Sea Opening, as can be seen on the right plots from the second to the fourth row of figure 5.6. The temperature of the inflow for the CCSM3 starts at $1.3°C$ and increases up to $6.1°C$. The outflow temperature is cooler at $-0.2°C$ in 1900 increasing to $3.5°C$ in 2100. The CCSM4 inflow temperature starts at $0.1°C$ and increases up to $2.2°C$ by 2100. Its outflow temperature starts at $0°C$ and increases up to $1.8°C$. The mean temperature of the Barents Sea opening starts at $1°C$ and $0°C$ and increases up to $5.5°C$ and $2°C$ respectively for the CCSM3 and the CCSM4.

The CCSM3 heat transport through the Barents Sea opening is maximal in its center, and is larger to the east than to the west, see the top row of figure 5.7. The CCSM4 increase in heat transport occurs over a thin vertical line at the center of the opening. The heat flux increase seen in the CCSM3 is more important than in the CCSM4. The velocity field increase is centred over the same region as the heat transport but spans a wider area. The increase in velocity is weak though with changes of the order of 0.01 m/s over 200 years. The temperature of the Barents Sea Opening increases over the whole gateway for both the CCSM3 and CCSM4. The highest increase occurs at the centre of the opening over the first 50 m for the CCSM3 and close to the surface for the CCSM4. The temperature increase of the CCSM3 goes over $6\,°C$ while the CCSM4 increase in temperature caps at $3\,°C$.

The most notable feature of the Barents Sea Opening is the considerable heat flux increase through the Barents Sea Opening predicted by the CCSM3 compared to the more modest increase of the CCSM4. The heat transport increase observed in the CCSM3 is caused by an important inflow increase coupled with an inconsequential outflow. The inflow increase is less important in the CCSM4 compared to the CCSM3 and its outflow is more important. The result is an increasing heat transport but not as large as seen in the CCSM3. The CCSM3 heat transport agrees with observations but its volume transport is too strong. On the other hand, the CCSM4 volume transport agrees with observations but its heat transport is too weak.

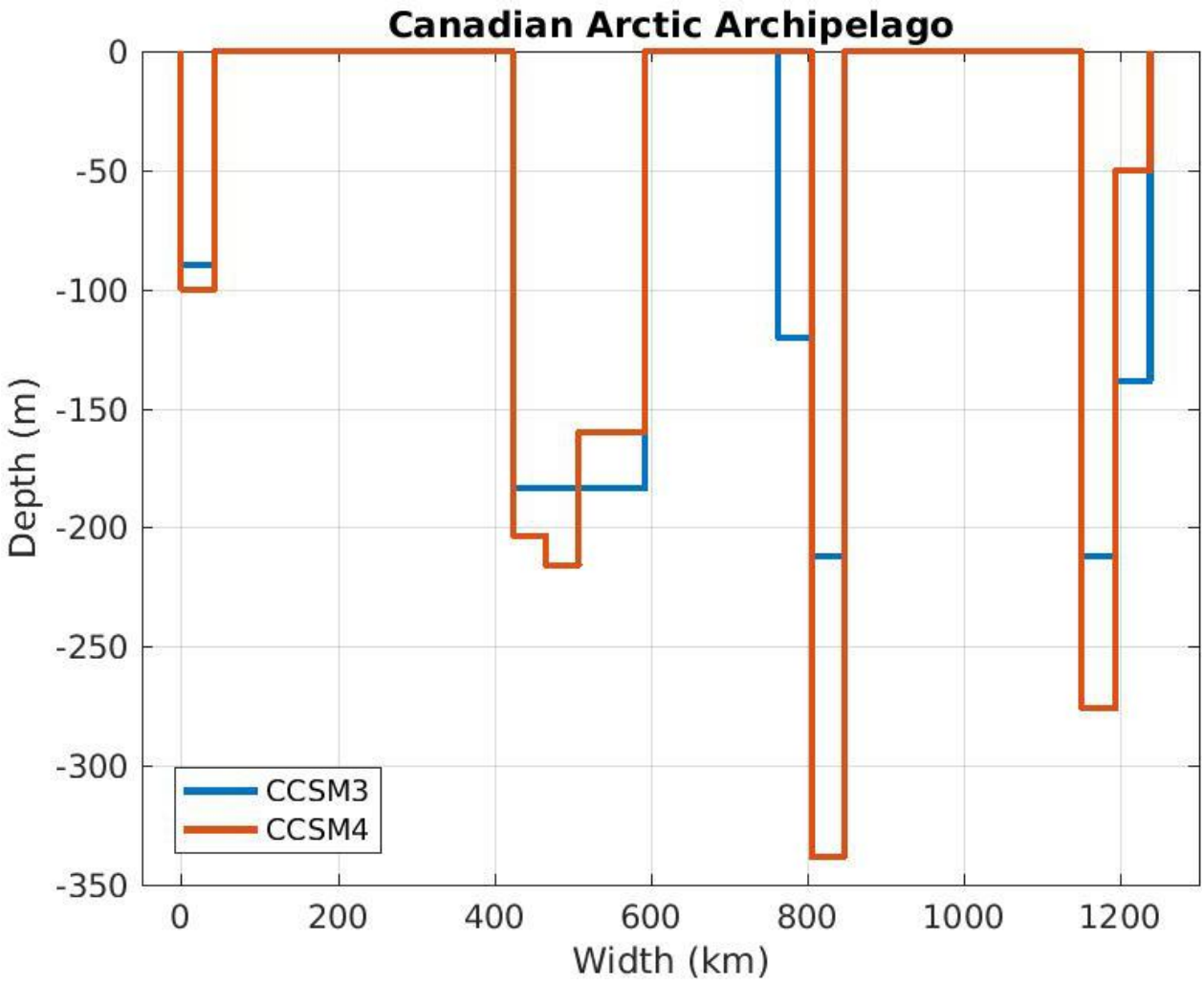

Figure 5.8: Bathymetry of the Canadian Arctic Archipelago along the cross-section defined in figure 3.2. It is completely located inside Canadian territory.

5.4 Canadian Arctic Archipelago

The bathymetry of the Canadian Arctic Archipelago along the line defined in figure 3.2 is presented in figure 5.8. It consists of four compact gateways: 1) Amundsen Gulf close to the Beaufort Sea, 2) M'Clure Strait, 3) The body of water between Melville Island and Ellesmere Island, 4) Nares Strait. The bathymetry of the CCSM4 reaches deeper than the CCSM3 with respective depth of 338m and 212m. On two openings, the CCSM3 is wider than the CCSM4. On the two other openings, the width is the same for both the CCSM3 and CCSM4. The resulting area, 64 km^2, is the same for both models. When it comes to observations of the gateways across the Canadian Arctic Archipelago, each gateway is studied separately by different teams of researchers. The observations are scarce and limited. None measured the

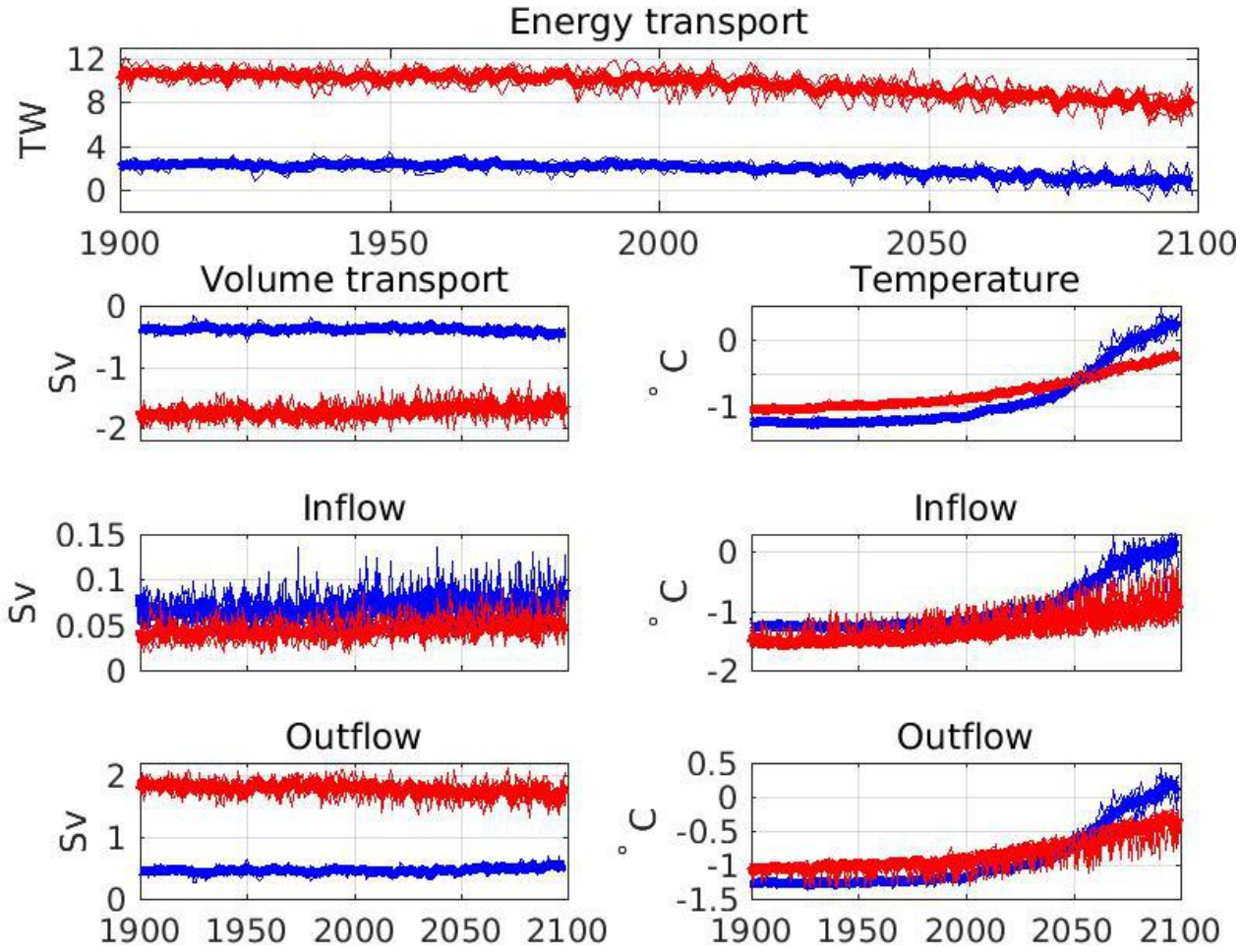

Figure 5.9: Canadian Arctic Archipelago heat transport in terawatts (TW), volume transport in Sverdrup (Sv) and temperature in degree Celsius ($°C$) for the CCSM3 in blue and the CCSM4 in red. Each simulation is represented by a thin line, and the model mean is represented by a bold line. The data for volume transport and temperature are presented as follows: averaged over the gateway (second row), averaged over the inflow region (third row), averaged over the outflow region (fourth row).

heat transport. Hence, we cannot provide any comparisons with observations. The openings of the Canadian Arctic Archipelago are narrow and when spatially plot, most of the openings is lost over the velocity grid. Also, the spatial variations are very modest. Therefore, there will be no spatial variation study of heat fluxes, velocity and temperature.

The heat flux through the Canadian Arctic Archipelago for the SRES A1B simulations starts at 2.2 TW and stays stable until 2000 where it decreases at a rate of -0.015 TW/a ending at 0.76 TW, see the first row of figure 5.9. The CCSM4 exhibits the same two phases. Its heat flux starts at 10.5 TW and is stable for 100 years where it decreases in magnitude at a rate of -0.024 TW/a ending at 7.7 TW. Note that the heat flux simulated by the CCSM4

is five times greater than the one predicted by the CCSM3.

The volume transport of the Canadian Arctic Archipelago is characterized by an outflow with an inconsequential inflow, see the left plots from the second to the fouth row of figure 5.9. The total volume of water through the Canadian Arctic Archipelago for the CCSM3 starts at -0.38 Sv in 1900 and increases in strength linearly up to -0.46 Sv by 2100. For the CCSM4, it starts at -1.8 Sv in 1900 and decreases in strength linearly down to -1.6 Sv by 2100. The reason for the higher outflow in the CCSM4 is because the Nares Strait is now connected to the Atlantic Ocean. It is a new feature of the ocean component of the CCSM4.

The mean temperature and the outflow temperature are almost identical due to the extremely weak inflow, see the right plots from the second to the fourth row of figure 5.9. The mean temperature of the inflow starts at $-1.2°C$ in 1900 and increases rapidly ending at $0.2°C$ in 2100 for the CCSM3. The CCSM4 Canadian Arctic Archipelago temperature starts at $-1°C$ in 1900 and increases non-linearly ending at $-0.25°C$ in 2100.

The positive heat transport through the Canadian Arctic Archipelago comes from the product of a negative velocity (outflow) and a negative temperature. By the end of the 21^{st} century, the CCSM3 temperature goes from subzero to positive resulting in several years with negative heat fluxes over the different simulations of the CCSM3. The outflow of the CCSM4 slightly decreases in strength. Its temperature increases getting closer to zero but staying negative. Both changes contribute to the CCSM4 decrease in heat transport magnitude through the Canadian Arctic Archipelago.

5.5 Bering Strait

The Bering Strait is the smallest gate to the Arctic Ocean. Its bathymetry is shown in figure 5.10. It links Russia to Alaska. The Bering Strait of the CCSM3 has an area of 8 km^2 which is twice the area in the CCSM4 with 4 km^2. The CCSM3 is 125 km wider and 11 m deeper than the CCSM4. The CCSM3 and the CCSM4 have a wider than observed Bering Strait which is approximated at 85 km wide (Beszczynska-Moller et al., 2011). The modelled Bering Straits are not deep enough. The Bering Strait is 50 m deep. The CCSM3 is far too wide with an acceptable depth. The CCSM4 is closer to reality in terms of the width but is

not deep enough with a depth of 30 m. The Bering Strait spans over such a small number of model cells that most spatial variations are deemed identical. No spatial figure are presented for that reason.

The advective heat flux through the Bering Strait of the SRES A1B from the CCSM3 starts at -2.1 TW and increases at 0.014 TW/a until 2000 where it accelerates at 0.07 TW/a ending at 5.1 TW, see the first row of figure 5.11. The CCSM4 follows the CCSM3 with higher values. It starts at -0.94 TW and increases at 0.03 TW/a for 100 years. For the remaining 100 years, it increases at 0.09 TW/a ending at 10 TW. Both versions of the CCSM present an increase in heat flux over the whole region. Woodgate et al. (2010) measured a heat flux between 10 and 20 TW between 1998 and 2007. The CCSM3 simulated -0.8 TW during the

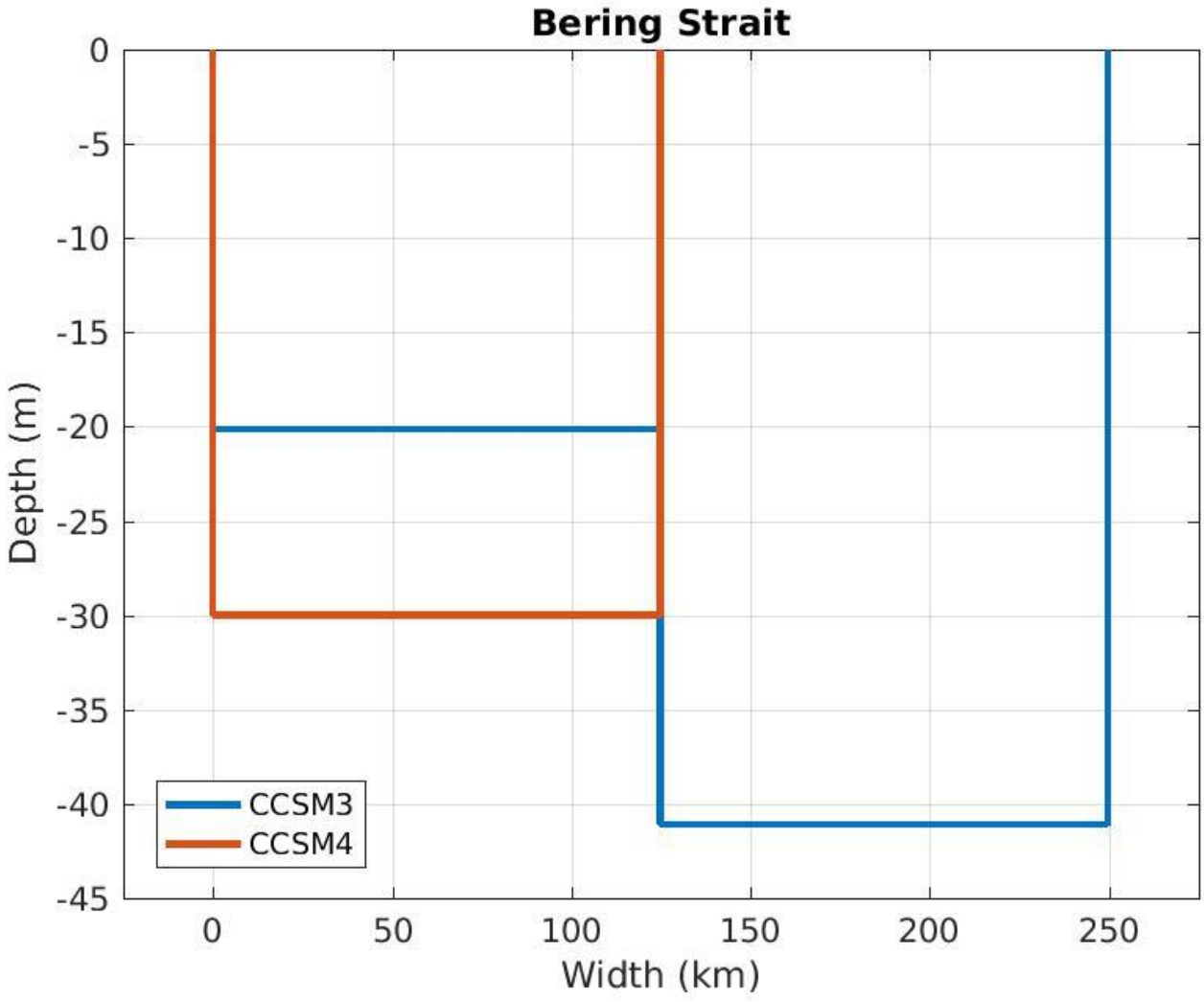

Figure 5.10: Bathymetry of the Bering Strait for the CCSM3 in blue and CCSM4 in red. On the right side (west) of the strait is Russia. On the left side (east) of the strait is Alaska.

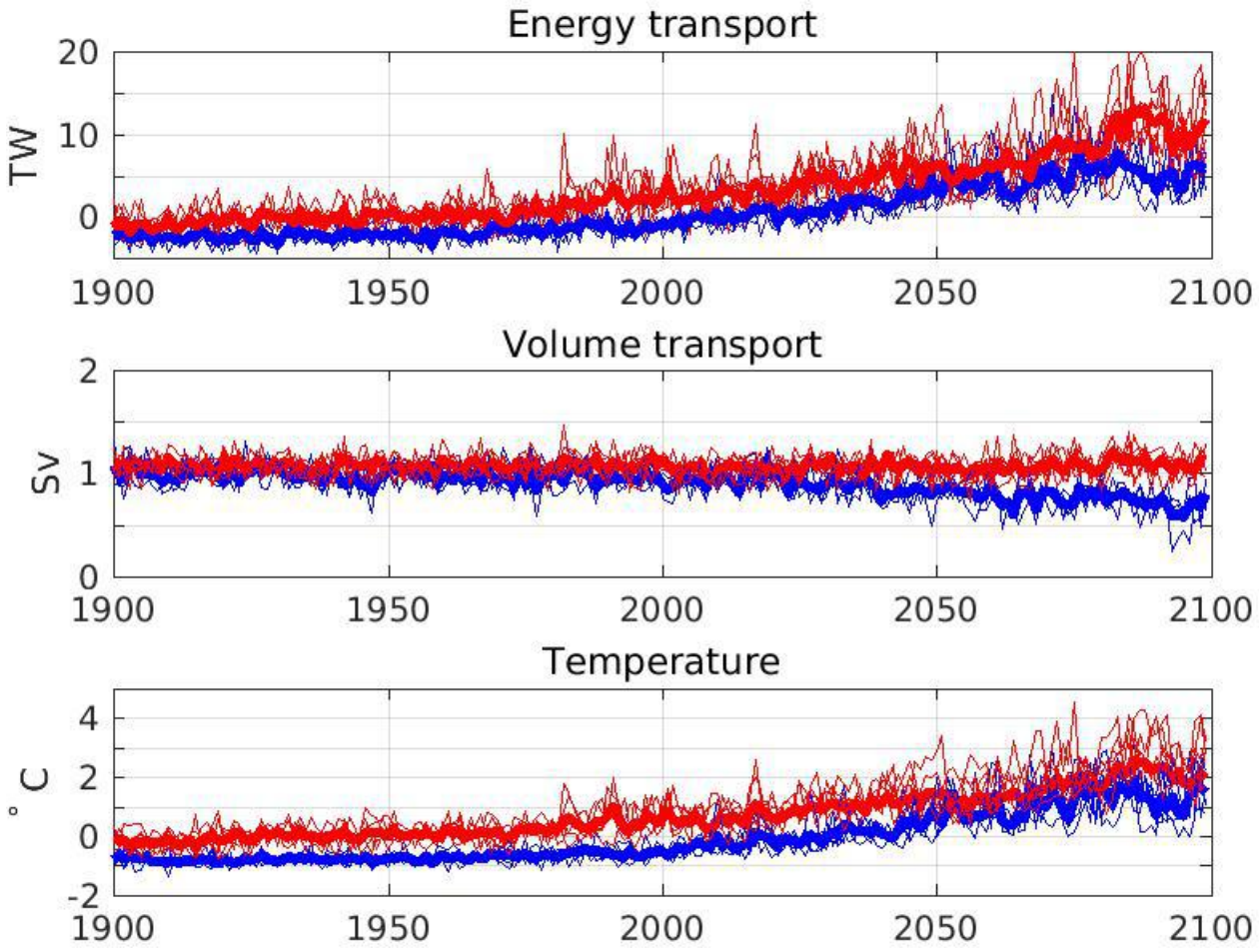

Figure 5.11: Bering Strait heat transport, volume transport and temperature. Blue) CCSM3. Red) CCSM4.

same period and the CCSM4 2.4 TW. They are both too low to agree with observations.

The Bering Strait has no outflow. The CCSM3 inflow is stable during the 20^{th} century at 1 Sv, see the second row of figure 5.11. It then decreases steadily over the 21^{st} century ending at 0.7 Sv. The CCSM4 inflow through the Bering Strait is stable over the full simulation at 1 Sv. Woodgate et al. (2010) observed an inflow of 0.8±0.2 Sv between 1998-2007. Both the CCSM3 and the CCSM4 agree with the observed inflow for the Bering Strait.

The temperature of the CCSM3 over the Bering Strait is modestly increasing over the 20^{th} century starting at $-0.9°C$ and ending at $-0.75°C$, see the third row of figure 5.11. During the 21^{st} century, it increases more rapidly ending at $1°C$ by 2100. The CCSM4 has the same two phases. The temperature of the Bering Strait for the CCSM4 starts at $-0.3°C$ in 1900, increases slowly up to $0.4°C$ in 2000 and then increases rapidly up to $2.3°C$ by 2100.

The CCSM3 and CCSM4 exhibit the same characteristics over the Bering Strait. The modelled shapes are not representative of the measurements. The increase in heat transport through the Bering Strait is explained by the increase in temperature. The heat fluxes disagree strongly with the observations being too weak but the volume transports agree.

5.6 Discussion

The heat transported through the Barents Sea Opening (BSO) is dominant compared to all the other gateways of the Arctic Ocean for the CCSM3, see figure 5.12. It is consistent with the sea ice missing in the Barents Sea observed in March 2099 in all the SRES A1B simulations of the CCSM3, see figure 3.4. The heat transport through the Fram Strait has a small impact on the total budget. The contribution from the Bering Strait and the Canadian

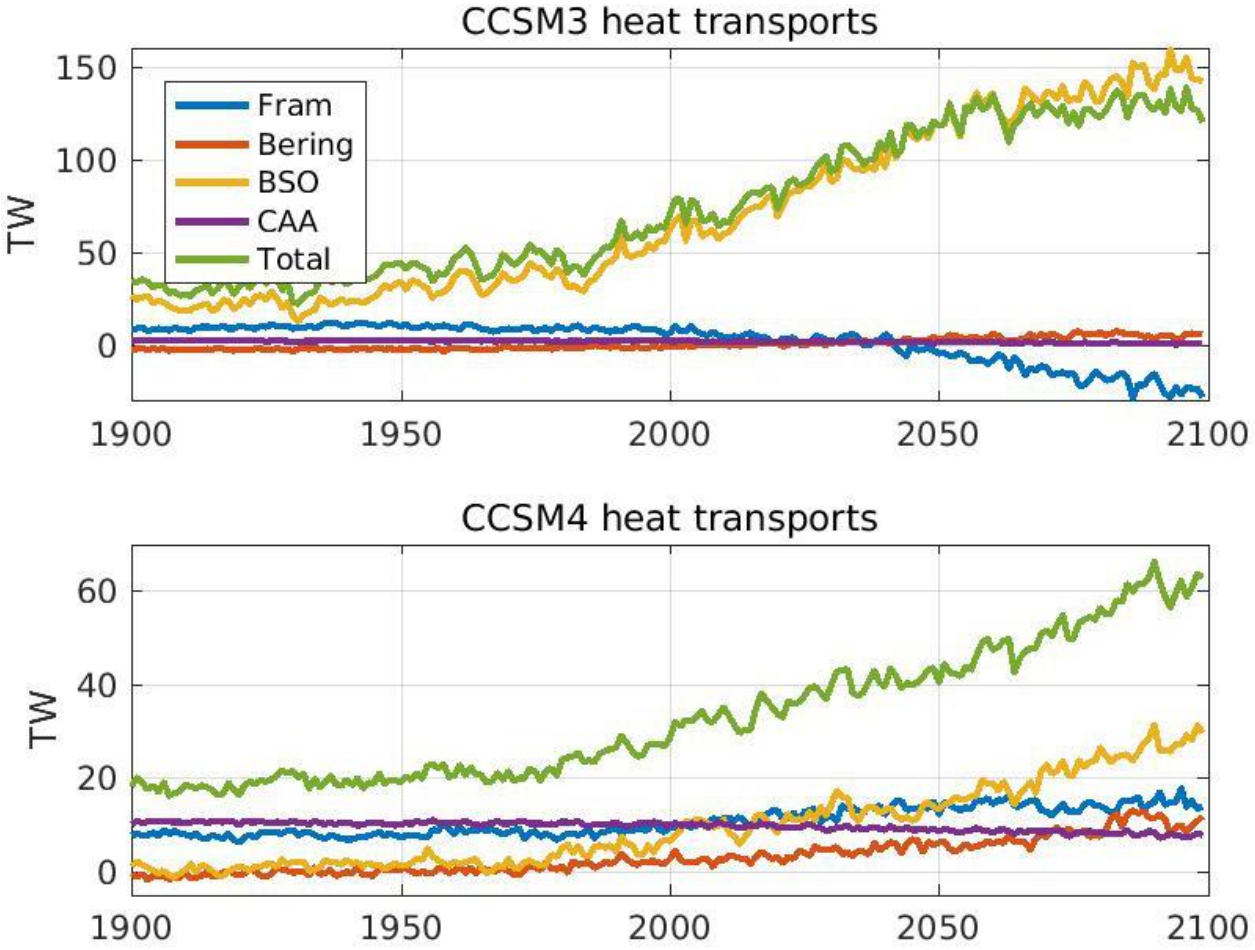

Figure 5.12: Heat transport through the gateways of the Arctic Ocean. Top) CCSM3. Bottom) CCSM4.

Arctic Archipelago are negligible. Even though the heat transport through the Bering Strait is small compared to the Barents Sea Opening, it can have an important effect. Indeed, since it is maximal close to the surface, its impact can be felt rapidly and strongly by the sea ice. It has left its mark on simulations a, b.ES01 and e, see figure 3.4. Woodgate et al. (2010) believe that the minimum sea extent recorded in 2007 was partly caused by an increase in heat transport through the Bering Strait weakening the sea ice in the vicinity.

In the case of the simulations under the RCP 6.0 scenario of the CCSM4, the total heat transported to the Arctic Ocean is divided into four commensurate sources. The Barents Sea Opening is the gateway that had the largest increase in heat transport, as it did in the CCSM3. The only decreasing heat flux comes from the Canadian Arctic Archipelago, with the decrease occurring mildly over the full simulation.

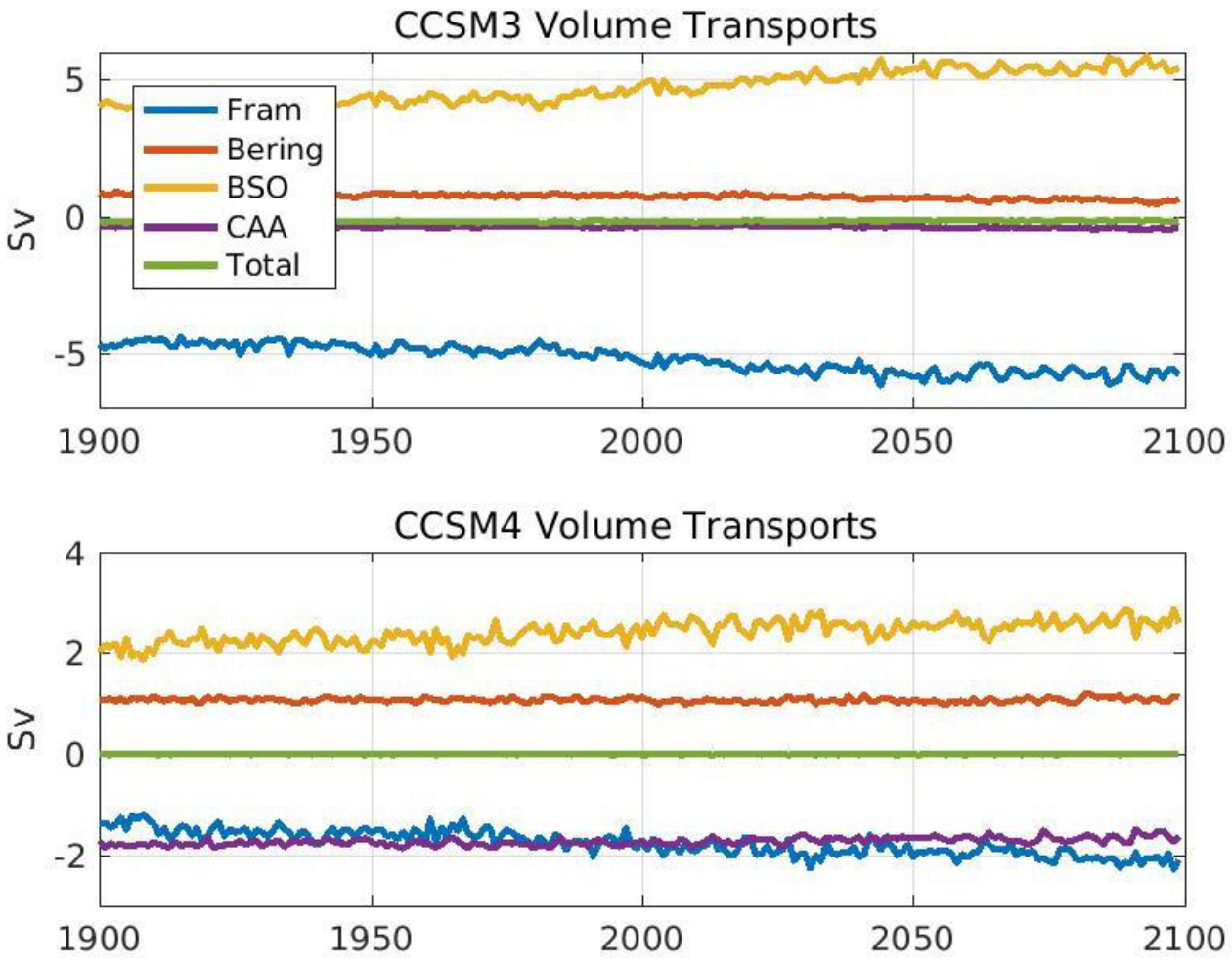

Figure 5.13: Volume transport through the gateways of the Arctic Ocean. Top) CCSM3. Bottom) CCSM4.

As stated in the introduction of this chapter, the warming of the Arctic takes several forms. The simulated heat transported to the Arctic Ocean by the CCSM3 SRES A1B is more aggressive than in the CCSM4 RCP 6.0. In 1900, the total heat transported to the Arctic Ocean was of 35 TW for the CCSM3 and 19 TW for the CCSM4. By 2100, it rose up to 130 TW for the CCSM3 and 60 TW for the CCSM4.

The volume transport budget closes satisfactorily in both CCSM3 and CCSM4. The CCSM ocean component treats the excess or loss of volume transport as sea level variation. The modest variations or the volume budget elevate or lower the mean sea level of the Arctic Ocean. The volume of water entering through the Barents Sea Opening in the CCSM3 is completely evacuated through the Fram Strait, as illustrated in figure 5.13. For the CCSM4, approximately one third of the water volume enters through the Bering Strait and two thirds through the Barents Sea Opening. Half of this water exits through the Fram Strait and the other half through the Canadian Arctic Archipelago.

The CCSM does not reproduce accurately the heat transport though the gateways of the Arctic Ocean in comparison to observations, as presented in table 5.1. The volume transport simulated by the CCSM4 agrees better than the one by the CCSM3. Indeed, while the CCSM4 volume transport agrees with observations for the Fram Strait, the Barents Sea

Heat transport

	Years	Obs	CCSM3	CCSM4
Fram	1997-2009	36 ± 6 TW	8 TW	9 TW
BSO	1997-2007	50-70 TW	60 TW	8 TW
CAA	-	-	-	-
Bering	1998-2007	10-20 TW	-0.8 TW	2.4 TW

Volume transport

	Years	Obs	CCSM3	CCSM4
Fram	1997-2007	-2.0±2.7 Sv	-5 Sv	-1.8 Sv
BSO	1997-2007	2 Sv	4.7 Sv	2.5 Sv
CAA	-	-	-	-
Bering	1997-2007	0.8±0.2 Sv	0.8 Sv	0.9 Sv

Table 5.1: Heat and volume transport through the gateways of the Arctic Ocean from observations, simulated by the CCSM3 SRES A1B and simulated by the CCSM4 RCP 6.0 scenario. The gateways of the Arctic Ocean are: Fram Strait, Barents Sea Opening (BSO), Canadian Arctic Archipelago (CAA) and Bering Strait. The highlighted values do not agree with the observations.

Opening and the Bering Strait, the CCSM3 volume transport agrees only for the Bering Strait. For the heat transport, both the CCSM3 and CCSM4 disagree with observations. Since the heat transport is calculated from the product of the volume flux and the gateway temperature, and the volume transport from the CCSM4 agrees with observations, the CCSM4 temperature fields must be inaccurate. It is known from Jahn et al. (2012) that the CCSM4 Arctic Ocean temperature profile is too high compared to observations below a depth of one kilometre. It is possible that one would obtain results that are more comparable with the observations if the bathymetry of the various gateways used in the simulations was closer to the real values.

6 Conclusion

Observations show that the most sensitive region of our planet to global warming is the Arctic (Serreze and Barry, 2011). Indeed, the Arctic magnifies the global warming (Holland and Bitz, 2003). Numerical simulations are our best tool to understand and forecasts the future of our climate. The equations of climate are non-linear making them difficult to solve without a numerical tool. For that reason, numerous numerical models have been developed all around the world. The non-linearity of the equations gives rise to chaotic behaviour. Small changes in the initial conditions can bring large discrepancies in the solutions. Consequently, the numerical simulations will stray away from observations. These difficulties make the study of climate forecast interesting and rich in ideas and innovations.

In chapter 2, we introduced the diverse elements defining the Arctic such as the Arctic Ocean and its sea ice. The basic features of the ocean and sea ice component of the CCSM versions 3 and 4 are discussed. Finally, the different futuristic scenarios used to forecast climate are presented. Reading chapter 2 should have introduce the reader to all the important notions required for chapters 3, 4 and 5 where the results from simulations from the CCSM versions 3 and 4 were analyzed.

This thesis studied (1) the thermal interactions between the Arctic sea ice and the Arctic Ocean, (2) the thermal interactions inside the Arctic Ocean, (3) advective heat fluxes through the gateways of the Arctic Ocean. In chapter 3, we investigated the evolution of the sea ice volume for the six simulations of the CCSM3 under the SRES A1B described in Holland et al. (2006b). Sea ice volume starts decreasing in 1950 while the sea ice extent decrease starts in the 21^{st} century; 40% of the sea ice volume has been lost between 1950 and 2000 compared to only 8% of the sea ice extent. The transport of sea ice volume out of the Arctic Ocean happens almost entirely through the Fram Strait. The Fram Strait sea ice export diminishes by 75% over the course of the simulations. The most important and most growing thermodynamic process is basal melt. It is determined by the amount of heat from the ocean transferred to the sea ice. The amount of heat transferred increased by more than 400%. This utmost increase is caused by a rapid increase in sea surface temperature. The rapid loss of September sea ice extent described in Holland et al. (2006b) cannot be explained solely by

the bottom melt though. All the other processes are important and cannot be neglected.

In chapter 4, we investigated all the heat sources influencing the Arctic Ocean surface temperature for the CCSM3. Unfortunately, the vertical heat diffusion is not part of the standard output of the CCSM3. It is possible to evaluate it as a residual of the temperature change and the other heat sources. To ascertain the inclusion of all the other heat sources, closing a column budget is necessary. The column budget has zero vertical diffusion at the ocean's surface and at the ocean's floor. This exercise leads to a 2 W/m^2 error over the Global Ocean, 3 W/m^2 over the Arctic Ocean and 150 W/m^2 over the columns. Those errors are unacceptable compared to the expected vertical diffusive heat fluxes less than 1 W/m^2 discussed in Timmermans et al. (2008). The error can be lowered using instantaneous temperature snapshots for the temporal derivative instead of monthly averaged temperature fields. The CCSM3 does not provide such fields at an acceptable temporal resolution, so we were unable to improve the magnitude of the error. The temperature snapshots were however accessible for the CCSM4, allowing us to perform this exercise. The CCSM4 temperature-heat budget closes up to 0.4 W/m^2 over the Global Ocean and the Arctic Ocean. Even if the budget errors for the Global and Arctic Oceans improved appreciably, the temperature-heat budget of the columns has an error of 50 W/m^2. The error in the temperature-heat budget is unacceptable and brings us to wonder whether the output of the CCSM can reproduce the temperature-heat equation. In the present case, we believe that a thorough testing of the code is in order so that one can understand where the error originates from. In the end, even if the code verification allowed us to shed some light on several of the heat sources at play, we were unable to obtain a refined temperature-heat budget where the error is acceptable over the grid columns.

Instead of examining all the heat sources as a whole, we scrutinized only one source in chapter 5: the advective heat fluxes through the gateways of the Arctic Ocean. We showed how advective heat fluxes can be elusive and that different calculations bring different results. Their impact on warming or cooling the Arctic Ocean can only be ascertained by doing a full budget over all the gates. The gateways include the Fram Strait, the Barents Sea opening, the Canadian Arctic Archipelago and the Bering Strait. There are considerable discrepancies

between the CCSM3 and CCSM4 forecasts. The heat transport through the Fram Strait of the CCSM3 and CCSM4 completely differ over the 21^{st} with the CCSM3 decreasing and the CCSM4 increasing both significantly. The heat transport in the CCSM3 through the Barents Sea Opening increases more than four times more than observed in the CCSM4. Over the Canadian Arctic Archipelago and the Bering Strait, the results are similar in the CCSM3 and in the CCSM4. The CCSM3 total heat transport is dominated by the Barents Sea Opening. It starts at 35 TW and ends at 130 TW. The CCSM4 total heat transport receives notable contributions from all the gateways. It begins at 19 TW in 1900 and stops at 60 TW. The advective heat transport is twice as important in the CCSM3 than in the CCSM4. The CCSM heat transport projections do not agree well with observations.

In term of innovative research, we studied extensively the physical processes affecting sea ice and their subcomponents. We found out that the significant increase in sea surface temperature is the most important change in the Arctic leading to sea ice melt. We tried to explain the increase in temperature using the same idea we used for the sea ice : analyzing the physical processes affecting the Arctic Ocean and their subcomponents. We have not been able to link the changes in temperature and the physical processes with exactitude. Reconstructing equations from the output variables of a climate model is a technical exercise. It is does not bring new scientific knowledge. Though, without a machine accurate reconstruction of the equations, only doubtful conclusion can be drawn. Such arduous exercise should be done by expert personnel from the climate model research center. Nevertheless, it was possible to study the advective heat transport through the gateways of the Arctic Ocean. We found that this heat transport warms the Arctic Ocean.

The exchange of heat between the Arctic Ocean and its sea ice is a complex process. we are proposing four ideas to improve our knowledge of the Arctic, its sea ice and its ocean:

1. High resolution simulations focussing on the junction between fluid and solid. This type of simulation would enhance our understanding of how heat and kinetic energy is transferred between the Arctic Ocean and the Arctic sea ice.

2. A thorough investigation of the CCSM temperature-heat equation. It seems the standard output does not offer the adequate variables to do so. The temperature is core in

the many transformations the Arctic undergoes. It is mandatory to access the sources of the temperature increase if we want to understand the future of the Arctic.

3. Climate model simulations with controlled ocean circulation and heat transport. The impact of the heat transport through the gates of the Arctic Ocean on the sea ice is a challenging topic. Only the first few ocean layers have the possibility to melt sea ice. It would be important to understand in detail which heat transports are impactful and how deep they can penetrate into the Arctic Ocean.

4. Climate simulations evolving through the future forcings instead of time. Simulations usually begin in 1900 and end in 2100. We are proposing to use future forcing instead. The simulations would begin at 0 W/m^2 and end at 8 W/m^2 for example. It could save computational time since one simulation through extra forcing forecasts all the future scenarios at once.

A CCSM3 temperature-heat budget

In this appendix, we explain how to access the variables important to the temperature-heat budget presented in chapter c3, how to obtain their definition and how to calculate the budget using the variables.

The standard output of the CCSM3 can be found in the monthly history files. Those files include all the output fields averaged monthly. It is possible to access one of the history file through the Earth System Grid web site[5]. If the reader owns a NCAR YubiKey, typing 'hsi' in a terminal connects the user to NCAR High Performance Storage System (HPSS) where all the outputs are stored. The ocean history files are located at /CCSM/csm/"RunName"/ocn/hist/. Using the command 'get', the user can transfer the file to his or her own account and then work with the data. The list of the variables included in a file can be shown by using the NETCDF[6] command 'ncdump -h "FileName" | less'. The option '-h' only shows the variables' description and not the data. The option '| less' will show enough information to fit the terminal size. It is then possible to go through the list pressing *Enter*. The heat transfer related variables include: surface fluxes, frazil ice formation, vertically integrated horizontal divergence of heat diffusion, advective heat fluxes in all three spatial directions, vertically integrated temperature advection tendency, potential temperature and some constants, see table A.1.

Using the variables in table A.1, the vertically integrated temperature heat budget is calculated as

$$cp\_sw \times rho\_sw \times TAREA \sum_z \left[\frac{T_{m+1,z} - T_{m-1,z}}{2\Delta t} dz \right] = \tag{A.1}$$
$$cp\_sw \times rho\_sw \times TAREA \times (HDIFT + ADVT)$$
$$+ TAREA \times (SHF + QFLUX),$$

where the subscript m designs the month, Δt is the number of seconds in the month. The indices for the latitude and the longitude are the same everywhere and are implicit.

[5] https://www.earthsystemgrid.org/home.html

[6] For more information on NETCDF visit *https://www.unidata.ucar.edu/software/netcdf/docs/faq.html#whatisit*, last visited May 9, 2018.

Name	Definition	Unit
SHF	Surface fluxes absorbed by the ocean.	W/m^2
QFLUX	Frazil ice formation.	W/m^2
HDIFT	Vertically integrated horizontal divergence of heat diffusion.	$cm\,^\circ C/s$
UET	Advective flux of Heat in grid-x direction	$^\circ C/s$
VNT	Advective flux of Heat in grid-y direction	$^\circ C/s$
WTT	Advective flux of Heat in grid-z direction	$^\circ C/s$
ADVT	Vertically integrated temperature advection tendency	$cm\,^\circ C/s$
TEMP	Potential temperature	$^\circ C$
TAREA	Area of T cells	cm^2
dz	Thickness of layer k	cm
cp_sw	Specific heat of sea water	$erg/g/K$
rho_sw	Density of sea water	g/cm^3

Table A.1: CCSM3 output variables required for the temperature-heat budget.

B CCSM4 temperature-heat budget

In this appendix, we presents the variables from the CCSM4 output important for the calculation of the temperature heat-budget in chapter 4.3 along with the budget equation using these variables. The procedure to obtain the variables is the same as presented in appendix A. Table B.1 contains the important variables that are part of the CCSM4 output which lead to the temperature-heat budget.

Using these variables, the vertically integrated temperature-heat budget can be written

Name	Definition	Unit
SHF	Surface fluxes absorbed by the ocean.	W/m^2
QFLUX	Frazil ice formation.	W/m^2
HDIFT	Vertically integrated horizontal divergence of heat diffusion.	$cm\,^\circ C/s$
UET	Advective flux of Heat in grid-x direction	$^\circ C/s$
VNT	Advective flux of Heat in grid-y direction	$^\circ C/s$
WTT	Advective flux of Heat in grid-z direction	$^\circ C/s$
ADVT	Vertically integrated temperature advection tendency	$cm\,^\circ C/s$
TEMP	Potential temperature	$^\circ C$
TAREA	Area of T cells	cm^2
dz	Thickness of layer k	cm
cp_sw	Specific heat of sea water	$erg/g/K$
rho_sw	Density of sea water	g/cm^3
HDIFE_TEMP	Advective flux of Heat in grid-x direction	$^\circ C/s$
HDIFN_TEMP	Advective flux of Heat in grid-y direction	$^\circ C/s$
HDIFB_TEMP	Advective flux of Heat in grid-z direction	$^\circ C/s$
KPP_SRC_TEMP	KPP non local mixing term	W/m^2

Table B.1: CCSM4 output variables required for the temperature-heat budget.

as

$$cp\_sw \times rho\_sw \times TAREA \sum_z \left[\frac{T_{y+1,z} - T_{y,z}}{\Delta t} dz \right] = \tag{B.1}$$
$$cp\_sw \times rho\_sw \times TAREA \times (HDIFT + ADVT)$$
$$+ TAREA \times (SHF + QFLUX + KPP\_SRC\_TEMP),$$

where the subscript y represents the year, the temperature field here is instantaneous, Δt is the number of seconds in a year. Again, The indices for the latitude and the longitude are the same everywhere and are implicit.

C CCSM4 code verification

Tracking the definition of a variable in a gigantic code such as the CCSM is a laborious task. There are no direct ways to follow a variable through the code up to its equation. The variables are constantly changing names and are sometimes calculated as temporary variables in a specific routine. The approach we followed consisted of taking one variable at a time and following its lead as far as possible. First, we found all the occurrences of the variable name using the terminal command 'grep VarName *.F90'. Second, we scrutinize all the entries in the terminal directly in the Fortran90 code file. Third, if the name of the variable changes, we restart at step one with the new name. At some point, the code and the variables start revealing themselves making searches easier and faster. In this appendix, we explain how to obtain the CCSM versions 3 and 4 code and every code part required to understand the different variables of the temperature-heat budget of the CCSM.

The CCSM4 code can be obtained following the instructions on the UCAR web site[7]. For those who could still be interested in the CCSM3, it can be obtained on the Earth System Grid web page: https://www.earthsystemgrid.org/. A search for 'CCSM3 code' should quickly bring the user to the download options for the code.

In the next sections, we present the notable sections of the codes relating to the temperature-

[7] *http://www.cesm.ucar.edu/models/ccsm4.0/ccsm_doc/x367.html*, last visited May 9, 2018

heat budget. Only the west-east components are explicitly presented. The south-north component is calculated identically but over a different index.

C.1 Temperature equation

The temperature equation is coded in the subroutine *tracer_update* called at line 551 of *baroclinic.F90* and defined at line 1600:

```
1680    FT = c0
1691    call hdifft(k, WORKN, TMIX, UMIX, VMIX, this_block)
1694    FT = FT + WORKN
1761    call advt(k,WORKN,WTK,TMIX,TCUR,UCUR,VCUR,this_block)
1763    FT = FT - WORKN ! advt returns WORKN = +L(T)
1788    call vdifft(k, WORKN, TOLD, STF_IN, this_block)
1790    FT = FT + WORKN
1835   call set_pt_interior(k,this_block,WORKN(:,:,1))
1853    call add_kpp_sources(WORKN, k, this_block)
1856    call add_sw_absorb(WORKN, SHF_QSW(:,:,bid), k, this_block)
1859    FT = FT + WORKN
1971    TNEW(:,:,k,n) = TOLD(:,:,k,n) + c2dtt(k)*FT(:,:,n)
```

The six involved subroutines are: (1) *hdifft* for the horizontal diffusion, (2) *advt* for the advection, (3) *vidfft* for the vertical diffusion, (4) *set_pt_interior* , *add_kpp_sources* and *add_sw_absorb*. Each routine computes its heat input in WORKN which is added to FT the temperature flux. We need to follow how WORKN is calculated in each routine. For each instance of WORKN, we want to know if it is output by the CCSM4.

C.2 Horizontal diffusion

The horizontal diffusion is the first element of the temperature budget being called. The subroutine *hdifft* can be found in *horizontal_mix.F90* at the line 413. The variable WORKN changes its name to HDTK. There are three diffusion schemes: laplacian (*hmix_del2*), biharmonic (*hmix_del4*) and Gent-McWilliams (*hmix_gm*). The simulation $b40.20th.track1.1deg.012$ used the Gent-McWilliams scheme. The routine computing the Gent-McWilliams mixing, *hdifft_gm*, is located in the file *hmix_gm.F90*. The variable HDTK in file *horizontal_mix.F90* changes its name to GTK in file *hmix_gm.F90*.

hmix_gm.F90

```
1162    subroutine hdifft_gm (k, GTK, TMIX, UMIX, VMIX, this_block)
1344    TX(i,j,kk,n,bid) = KMASKE(i,j) &
```

```
1445    * (TMIX(i+1,j,kk,n) - TMIX(i,j,kk,n))
1440    TX(i,j,kk+1,n,bid) = KMASKE(i,j) &
1441    * (TMIX(i+1,j,kk+1,n) - TMIX(i,j,kk+1,n))
2023    WORK3(i,j) = KAPPA_ISOP(i, j,ktp,k,bid) &
2024    + HOR_DIFF (i, j,ktp,k,bid) &
2025    + KAPPA_ISOP(i, j,kbt,k,bid) &
2026    + HOR_DIFF (i, j,kbt,k,bid) &
2027    + KAPPA_ISOP(i+1,j,ktp,k,bid) &
2028    + HOR_DIFF (i+1,j,ktp,k,bid) &
2029    + KAPPA_ISOP(i+1,j,kbt,k,bid) &
2030    + HOR_DIFF (i+1,j,kbt,k,bid)
2076    FX(:,:,n) = dz(k) * CX * TX(:,:,k,n,bid) * WORK3
2077    FY(:,:,n) = dz(k) * CY * TY(:,:,k,n,bid) * WORK4
2340    GTK(i,j,n) = ( FX(i,j,n) - FX(i-1,j,n) &
2341    + FY(i,j,n) - FY(i,j-1,n) &
2342    + FZTOP(i,j,n,bid) - fz )*dzr(k)*TAREA_R(i,j,bid)
```

CX is related to the grid. TMIX is the tracer at the mixing time level. KMASKE is the ocean mask for the east side of grid cells. The CCSM grid places the tracers at the centre of the grid as illustrated in figure 2.8.

To calculate the tracer diffusion, it is required to compute the tracer value at the sides of the cell times the diffusion component. TX and TY are the tracer values at the east side of the cell and at the north side of the cell respectively. WORK3 and WORK4 are the diffusion component on the east side and north side of the cell respectively. FX is the eastward diffusion of heat on the east side of the cell and FY is the northward diffusion of heat on the north side of the cell. Finally, GTK is the divergence of diffusion of a cell.

Once GTK is sent back in *horizontal_mix.F90* as HDTK, it is integrated vertically and output as variable HDIFT.

horizontal_mix.F90

```
333     call define_tavg_field(tavg_HDIFT,'HDIFT',2, &
334     long_name='Vertically Integrated Horz Mix T tendency', &
335     coordinates='TLONG TLAT time', &
336     units='centimeter degC/s', grid_loc='2110')
413     subroutine hdifft(k, HDTK, TMIX, UMIX, VMIX, this_block)
485     where (k <= KMT(:,:,bid))
486     WORK = dz(k)*HDTK(:,:,1)
491     call accumulate_tavg_field(WORK,tavg_HDIFT,bid,k)
```

KMT gives the index of the deepest grid cell on the T-grid. The CCSM code defines output field using function *define_tavg_field* and then averages and stores date using function *accumulate_tavg_field*. Here, the variable tavg_HDIFT is linked to the output variable

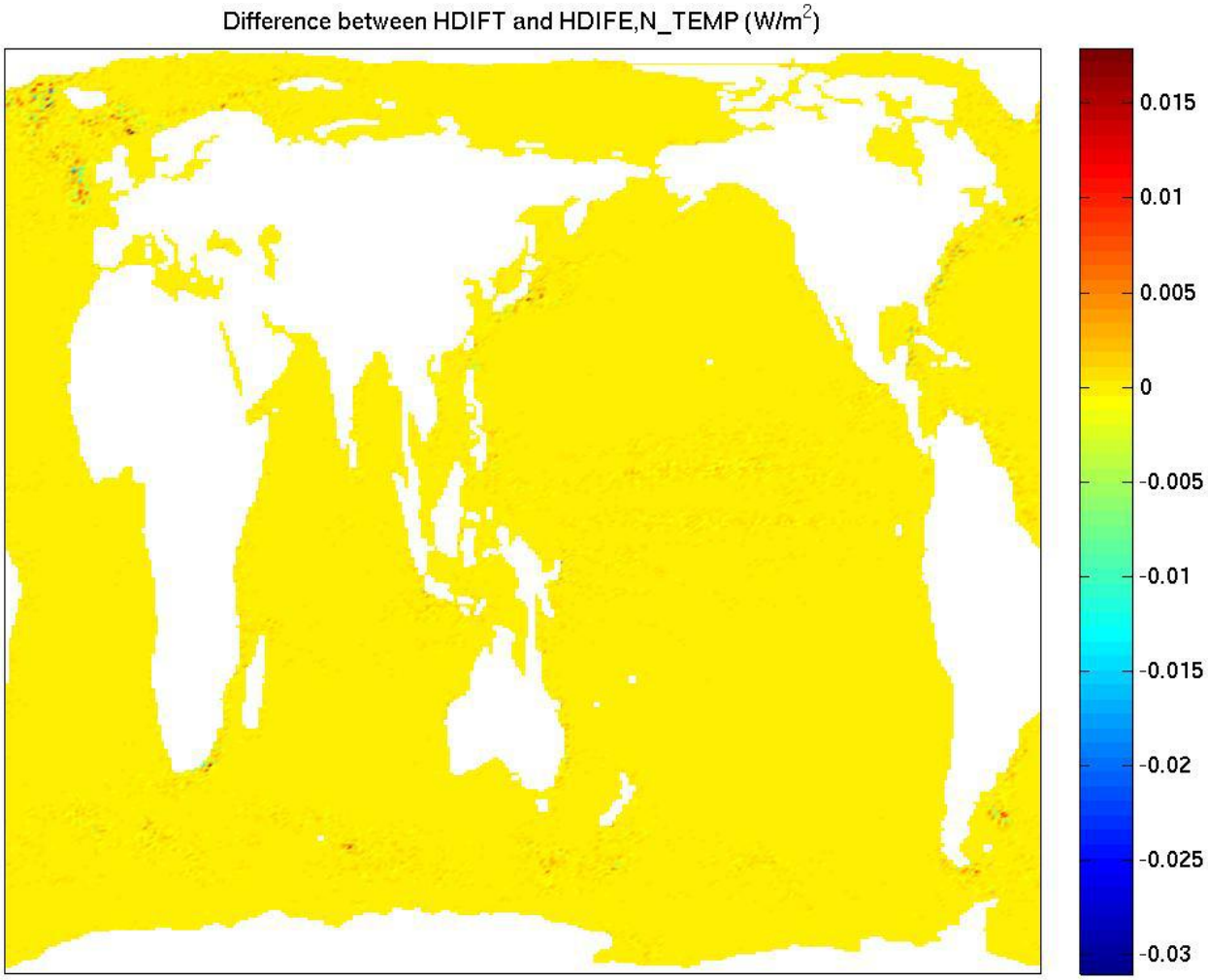

Figure C.1: Difference between HDIFT and its reconstruction from HDIFE_TEMP and HDIFN_TEMP in W/m^2.

HDIFT in line 333. The variable WORK is averaged as tavg_HDIFT which will be output as HDIFT, line 491.

The MOAR outputs three extra variables for diffusion: HDIFE_TEMP, HDIFN_TEMP, HDIFB_TEMP. There is nothing about those variables in the code. Based on their definition using the terminal command ncdump, it is reasonable to believe that HDIFE_TEMP is FX in line 2076 and HDIFN_TEMP is FY in line 2077. FX and FY units are $cm^3\,°C/s$ while HDIFE_TEMP and HDIFN_TEMP are $°C/s$. Therefore, we believe that FX and FY have been divided by TAREA and dz to give HDIFE_TEMP and HDIFN_TEMP.

We can test our hypothesis by reconstructing HDIFT from the vertically integrated divergence of HDIFE_TEMP and HDIFN_TEMP. Following lines 2340 and 2341 in hmix_gm.F90,

the divergence is given by

$$HDIFE\_TEMP_{ij} \cdot TAREA_{ij} - HDIFE\_TEMP_{i-1\,j} \cdot TAREA_{i-1\,j} \tag{C.1}$$

$$+ HDIFN\_TEMP_{ij} \cdot TAREA_{ij} - HDIFN\_TEMP_{i\,j-1} \cdot TAREA_{i\,j-1}. \tag{C.2}$$

Using the output of the history file b40.20th.track1.1deg.012.pop.h.1998-12.nc, the error between HDIFT and its reconstruction peaks at $0.03\,W/m^2$, see figure C.1. We conclude that HDIFE_TEMP and HDIFN_TEMP are the eastward and northward diffusive heat flux respectively.

In conclusion, the vertically integrated divergence of the ocean horizontal diffusive heat flux is stored by the CCSM as HDIFT. For the MOAR of the CCSM4, extra variables are output: the eastward diffusive heat flux HDIFE_TEMP and the northward diffusive heat flux HDIFN_TEMP.

C.3 Advection

The second element of the temperature budget is the heat advection calculated in subroutine *advt* which can be found in the file *advection.F90*. The variable WORKN changes its name to LTK.

advection.F90

```
1602    subroutine advt(k,LTK,WTK,TMIX,TRCR,UUU,VVV,this_block)
2513    LTK(i,j,n) = p5*((VTN(i,j)-VTN(i,j-1)+UTE(i,j)-UTE(i-1,j)) &
2514    *TRCR(i ,j ,k,n) + &
2515    VTN(i ,j )*TRCR(i ,j+1,k,n) - &
2516    VTN(i ,j-1)*TRCR(i ,j-1,k,n) + &
2517    UTE(i ,j )*TRCR(i+1,j ,k,n) - &
2518    UTE(i-1,j )*TRCR(i-1,j ,k,n))* &
2519    TAREA_R(i,j,bid)/ &
2548    LTK(:,:,n) = LTK(:,:,n) + dz2r(k)*WTK* &
2549    (TRCR(:,:,k-1,n) + TRCR(:,:,k ,n))
2562    LTK(:,:,n) = LTK(:,:,n) - dz2r(k)*WTKB* &
2563    (TRCR(:,:,k,n) + TRCR(:,:,k+1,n))
```

VTN is the northward velocity located on the north side of the cell and UET is the eastward velocity on the east side of the cell. LTK starts by computing the divergence of horizontal tracer transport. It then adds vertical tracer transport at the top of the cell and then at the bottom of the cell.

The variable LTK is then multiplied by minus the vertical length of the cell, summed vertically and stored as ADVT.

advection.F90

```
 782    call define_tavg_field(tavg_ADV_TRACER(1),'ADVT',2, &
 783    long_name='Vertically-Integrated T Advection Tendency',&
 784    units='centimeter degC/s', grid_loc='2110', &
 785    coordinates='TLONG TLAT time')
1602    subroutine advt(k,LTK,WTK,TMIX,TRCR,UUU,VVV,this_block)
1922    WORK(i,j) = -dz(k)*LTK(i,j,n)
1926    call accumulate_tavg_field(WORK,tavg_ADV_TRACER(n),bid,k)
```

In the temperature equation, -WORKN is added to FT. The stored version of the vertically integrated heat advection already includes the minus sign as of line 1922. Therefore, the temperature budget made from the output of the CCSM will have the form $\frac{dT}{dt} = ADVT + \cdots$ instead of the usual $\frac{dT}{dt} + ADV = \cdots$.

From the variable list, two other variables are giving advective heat transport: UET and VNT. They are calculated in file advection.F90. The following analysis depicts the investigative work required to understand how is calculated an output variable of the CCSM.

advection.F90

```
 749    call define_tavg_field(tavg_UE_TRACER(1),'UET',3, &
 754    call define_tavg_field(tavg_VN_TRACER(1),'VNT',3, &
1777    FVN = p5*VTN*TAREA_R(:,:,bid)
1778    FUE = p5*UTE*TAREA_R(:,:,bid)
1820    WORK = FUE*( TRCR(:,:,k,n) + &
1821    eoshift(TRCR(:,:,k,n),dim=1,shift=1))
1822    call accumulate_tavg_field(WORK,tavg_UE_TRACER(n),bid,k)
1835    WORK = FVN*( TRCR(:,:,k,n) + &
1836    eoshift(TRCR(:,:,k,n),dim=2,shift=1))
1837    call accumulate_tavg_field(WORK,tavg_VN_TRACER(n),bid,k)
2337    UTE(i,j) = p5*(UUU(i ,j ,k)*DYU(i ,j ,bid) + &
2338    UUU(i ,j-1,k)*DYU(i ,j-1,bid))
2342    VTN(i,j) = p5*(VVV(i ,j ,k)*DXU(i ,j ,bid) + &
2343    VVV(i-1,j ,k)*DXU(i-1,j ,bid))
```

The variable WORK is accumulated as $tavg\_UE\_TRACER$, line 1822, which is output as UET, line 749. WORK is calculated as west-east velocity on the east side of the cell times the length of the east side divided by the surface area, FUE, multiplied by the tracer on the east side of the cell. It is the advective tracer transport per surface area unit per vertical length unit.

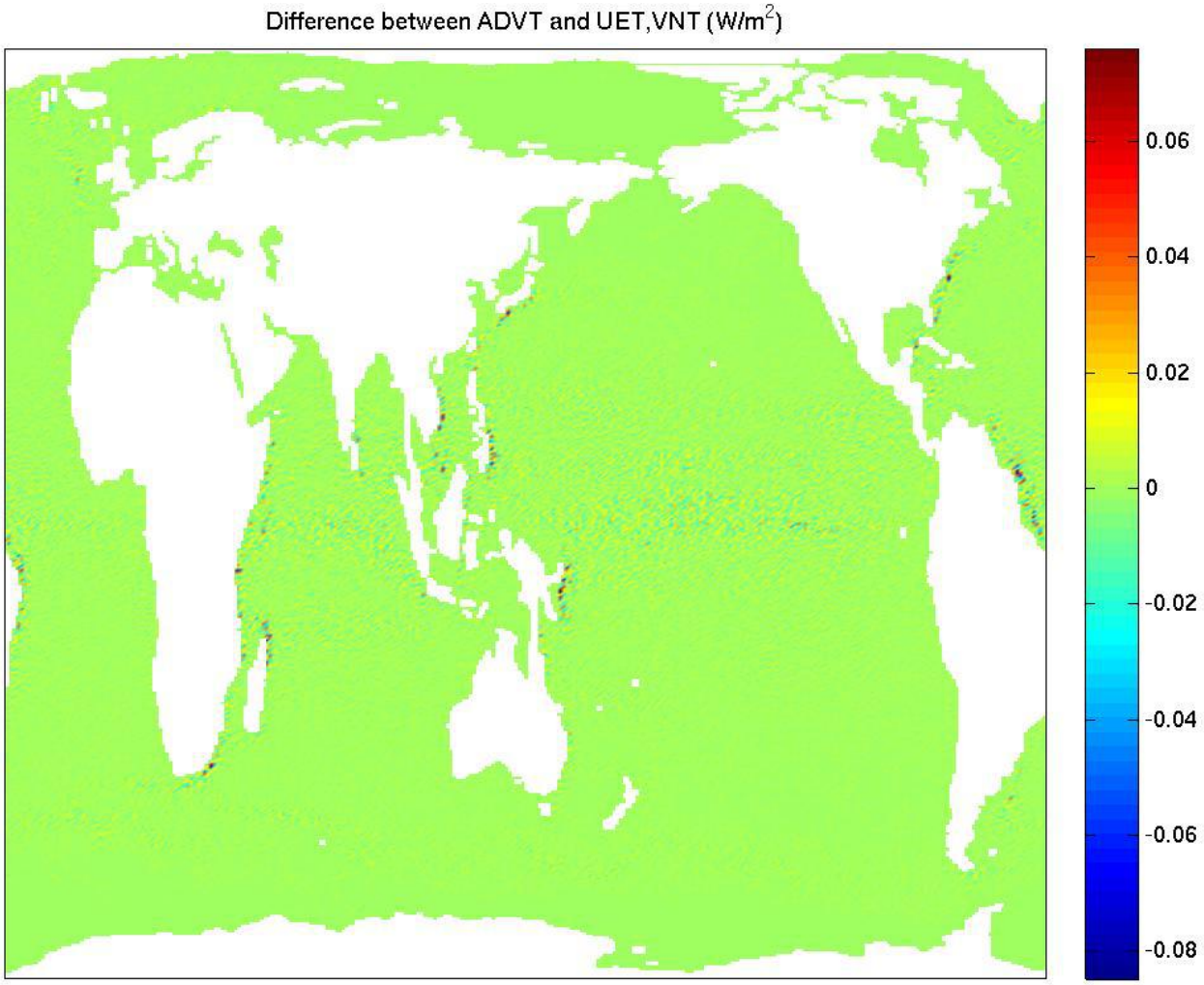

Figure C.2: Difference between ADVT and its reconstruction from UET and VNT in W/m^2.

Putting together the pieces of code for ADVT, UET and VNT, it seems UET and VNT are the east and north part of ADVT divided by TAREA. The divergence must be calculated as shown in the diffusion section, see equation C.1. The error between ADVT and its reconstruction is extremely high for 34 columns over 122,880 peaking at $8000\,W/m^2$. Once those 34 points are neglected, the error drops at a maximum of $0.1\,W/m^2$, see figure C.2. We do not fully understand the source of the high error over such a small number of columns. We believe it could come from storing errors from the hardware.

In conclusion, the vertically integrated divergence of heat advection is stored in variable ADVT with an extra minus sign. Variables UET and VNT are the eastward and northward heat advection.

C.3.1 Vertical diffusion

The third element of the temperature equation is the vertical diffusion. It is calculated in file *vertical_ mix.F90*. The variable WORKN changes its name to VDTK.

vertical_mix.F90

```
645   subroutine vdifft(k, VDTK, TOLD, STF, this_block)
733   if (k == 1) then
734   VTF(:,:,n,bid) = merge(STF(:,:,n), c0, KMT(:,:,bid) >= 1)
735   endif
765   VTFB = merge(VDC(:,:,kvdc,mt2,bid)* &
766   (TOLD(:,:,k ,n) - TOLD(:,:,kp1,n))*dzwr(k) &
767   ,c0, KMT(:,:,bid) > k)
771   VTFB = merge( -bottom_heat_flx, VTFB, &
772   k == KMT(:,:,bid) .and. &
773   zw(k) >= bottom_heat_flx_depth)
777   VDTK(:,:,n) = merge((VTF(:,:,n,bid) - VTFB)*dzr(k), &
778   c0, k <= KMT(:,:,bid))
788   VTF(:,:,n,bid) = VTFB
```

VDTK is calculated as the difference between VTF and VTFB. They are the vertical heat diffusion at the top and the bottom of the cell respectively. The model sets the vertical heat diffusion at the bottom of the ocean at zero. It then calculates the bottom heat diffusion of the next cell by multiplying the diffusivity, VDC, and the vertical temperature derivative at the bottom of the cell. The surface heat diffusion of the lower cell is defined by the bottom heat diffusion of the higher cell. For the first layer, the vertical heat diffusion is given by STF. It is defined in the file forcing_coupled.F90

forcing_coupled.F90

```
715   STF(:,:,1,iblock) = (EVAP_F(:,:,iblock)*latent_heat_vapor &
716   + SENH_F(:,:,iblock) + LWUP_F(:,:,iblock) &
717   + LWDN_F(:,:,iblock) + MELTH_F(:,:,iblock) &
718   -(SNOW_F(:,:,iblock)+IOFF_F(:,:,iblock)) * latent_heat_fusion_mks)* &
719   RCALCT(:,:,iblock)*hflux_factor
```

STF includes several surface fluxes: evaporation, sensible heat, emitted and absorbed long wave, melt, snow and ice runoff. Note that the standard output files describe the latent heat of vapour units as KJ/Kg but it actually has units of J/Kg.

The subroutine collecting the standard output variables, accumulate_tavg_field, is not called in subroutine vidfft for the variable VDTK. Hence, the vertical diffusion is not part

of the standard output. When integrated vertically, the diffusion at the top of a cell will be cancelled by the bottom of the following cell (line 788) leaving only the contribution from the bottom and top of the column. The bottom of the column is set at zero (line 778) and the top of the column holds surface fluxes (lines 670, 734-735). The variable STF plus the shortwave radiation absorbed by the ocean is output as variable SHF.

forcing.F90

```
445    WORK = (STF(:,:,1,iblock)+SHF_QSW(:,:,iblock))/ &
446    hflux_factor ! W/m^2
451    call accumulate_tavg_field(WORK,tavg_SHF,iblock,1)
```

Every surface fluxes are output separately. When the definition of SHF is compared to the output files, the resulting error is machine accurate, figure C.3.

In conclusion, the vertical diffusion is not output by the CCSM. It is possible to work around it by calculating the vertically integrated budget. The only non-zero terms left after the integration are: evaporation, sensible heat, emitted and absorbed longwave, melt, snow and ice runoff. They are output separately or as a bundle with the shortwave radiation in variable SHF.

C.4 Reset temperature

The fourth element of the temperature budget, set_pt_interior, is calculated in file forcing_pt_interior.F90. The variable WORN changes its name to PT_SOURCE.

forcing_pt_interior.F90

```
677    subroutine set_pt_interior(k,this_block,PT_SOURCE)
756    DPT_INTERIOR = pt_interior_restore_rtau* &
757    (PT_INTERIOR_DATA(:,:,k,bid,now) - &
758    TRACER(:,:,k,1,curtime,bid))
766    PT_SOURCE = PT_SOURCE + DPT_INTERIOR
```

The constant pt_interior_restore_rtau is defined as $(24 * 60^2 * 10^{20})^{-1}$. It is the reciprocal of the restoring timescale. The variable PT_INTERIOR_DATA is defined as the limit temperature the model allows. If the computed temperature exceeds the limit, the model restores the temperature at the limit. It is not part of the standard output. Though, the

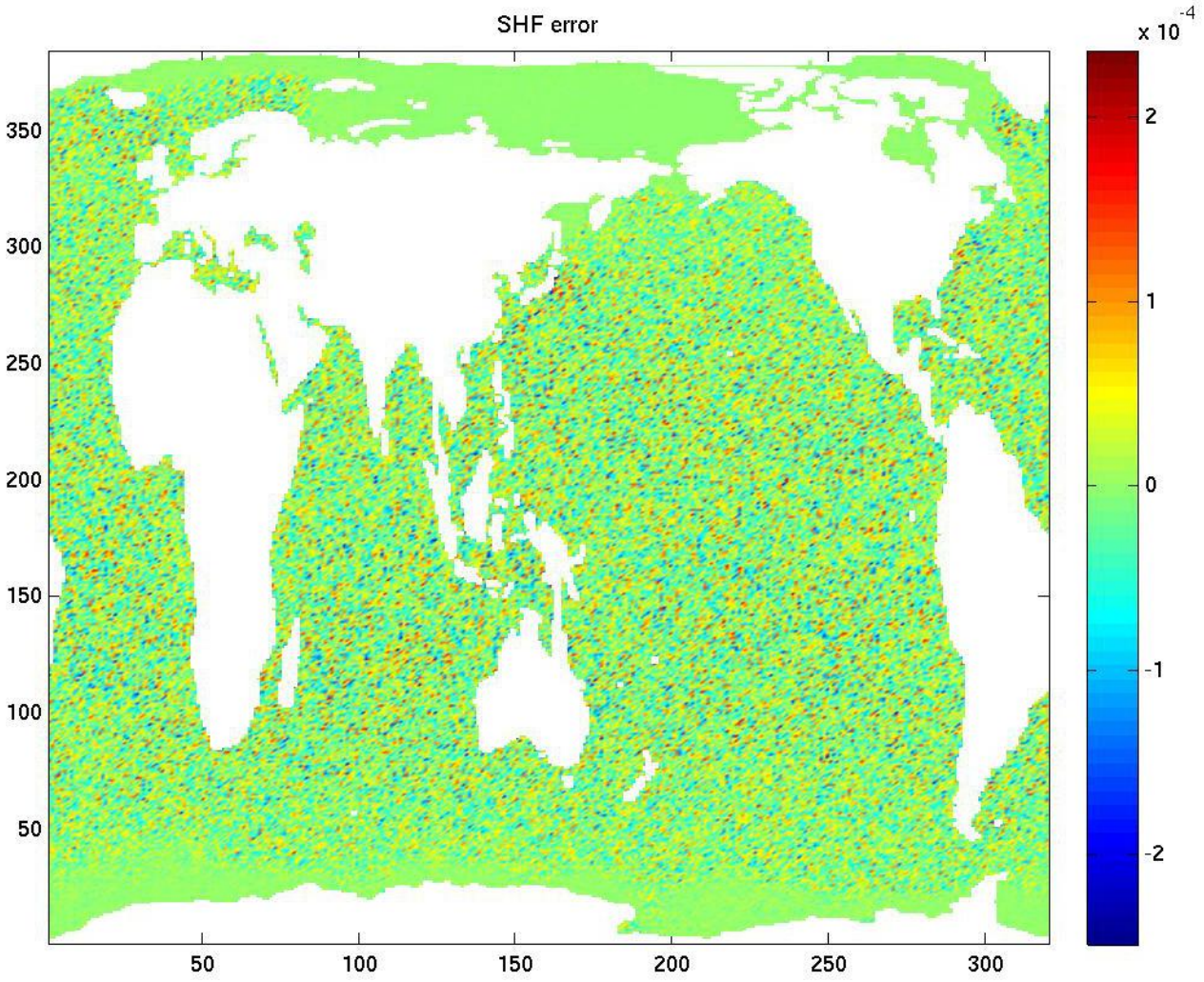

Figure C.3: Code definition of SHF verification with the output variables: SHF, EVAP_F, SENH_F, LWUP_F, LWDN_F, MELTH_F, SNOW_F, IOFF_F, SHF_QSW. The colour axis is in W/m^2.

variable QFLUX, which is part of the standard output, seems to hold that role. It is defined in ice.F90.

ice.F90

```
451    POTICE = (TFRZ - TNEW(:,:,k,1))*DZT(:,:,k,bid)
506    QICE(:,:,bid) = QICE(:,:,bid) - POTICE
692    QFLUX(:,:,bid) = QICE(:,:,bid)/tlast_ice/hflux_factor
```

From the code, Hunke and Lipscomb (2010) and Smith and Gent (2004b),

$$QFLUX = \frac{\Theta_f - \Theta}{\Delta t_{ice}} \, dz \, \rho_w \, C_{pw}. \tag{C.3}$$

It restores any temperature below the freezing temperature and transform this energy in frazil ice formation.

In conclusion, the restoring temperature flux is not part of the standard output. We believe the variable QFLUX holds that role but we did not find any direct link with PT_SOURCE.

C.5 KPP

The fifth element of the temperature equation, add_kpp_sources, is calculated in vix_kpp.F90. It is the nonlocal K-profile parameterization for vertical mixing, or KPP, defined in Large et al. (1994). The variable WORKN changes its name to KPP_SRC.

vmix_kpp.F90

```
896     KPP_SRC(:,:,k,n,bid) = STF(:,:,n)/DZT(:,:,k,bid) &
897     *( VDC(:,:,k-1,mt2)*GHAT(:,:,k-1) &
898     -VDC(:,:,k ,mt2)*GHAT(:,:,k ))
```

VDC is the diffusivity and GHAT is the non-local mixing coefficient. The nonlocal vertical mixing of temperature is output as variable KPP_SRC_TEMP. Note that KPP_SRC_TEMP sums up to zero when integrated vertically, figure C.4.

C.6 Absorbed short wave

The sixth, and last, element of the temperature budget is add_sw_absorb and is calculated in file sw_absorption.F90. The variable WORKN changes its name to WORK.

sw_absorption.F90

```
868     WORK = max(SHF_QSW,c0) !*** insure no neg QSW - store in work
```

The variable SHF_QSW is the short wave absorbed from the ocean. It is given to the ocean component of the CCSM from the coupler that acquired the data from the atmosphere and sea ice components. It is output individually and as a bundle with all the other surface fluxes as SHF. SHF has already been discussed in section C.3.1.

C.7 Conclusion

Accounting for the six subroutines included in the temperature equation, the required variables for the vertically integrated budget are: HDIFT for the horizontal diffusion, ADVT for the horizontal advection, SHF for the surface forcing included in the vertical diffusion and the short wave absorption subroutines, QFLUX for the restoring temperature. The column budget equation becomes:

$$\sum_z \frac{\partial T}{\partial t} = HDIFT + ADVT + SHF + QFLUX. \tag{C.4}$$

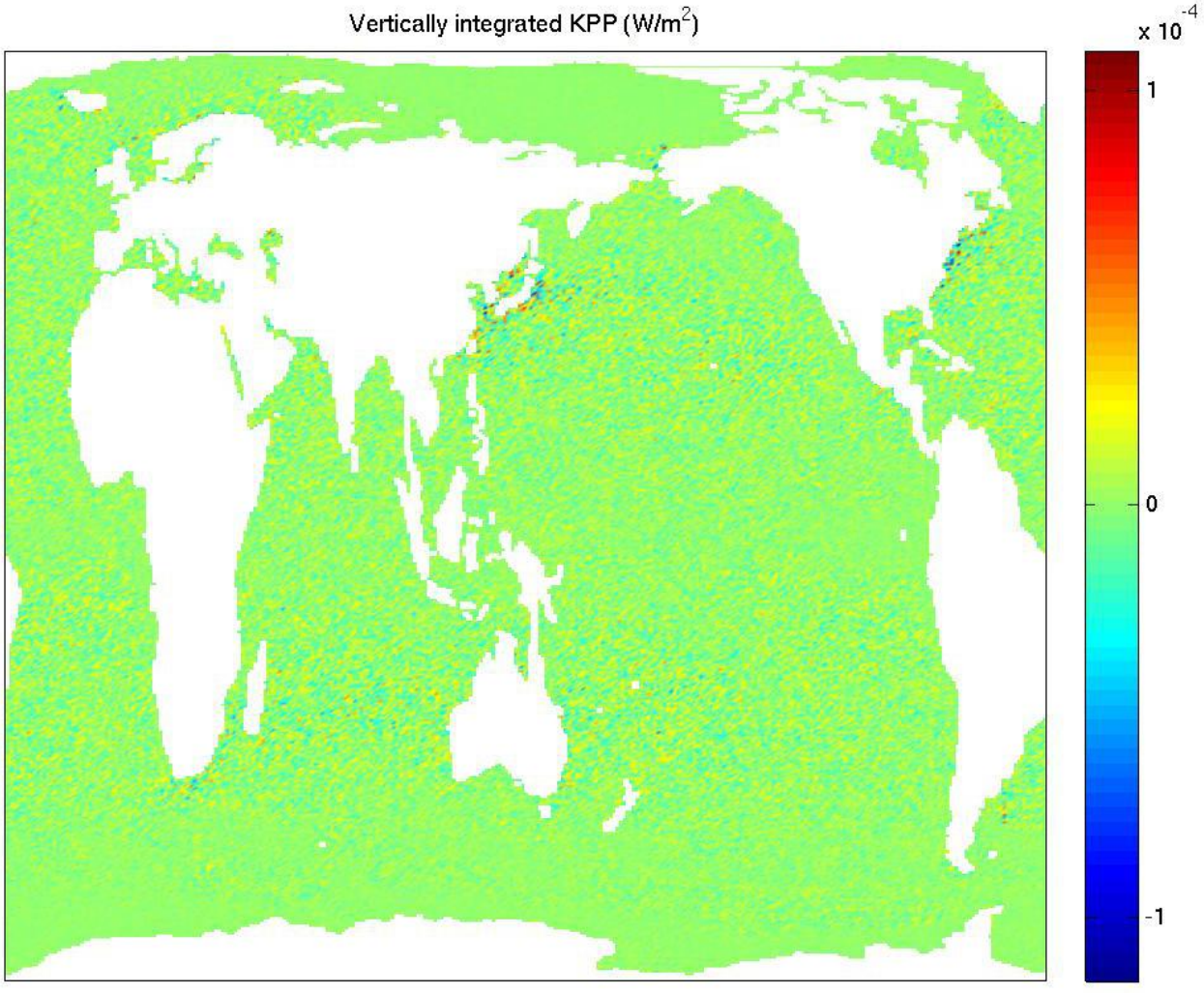

Figure C.4: Yearly vertically integrated KPP mixing term in W/m^2.

References

Aagaard, K., Coachman, L. K., and Carmack, E. (1981). On the halocline of the arctic ocean. *Deep Sea Research Part A. Oceanographic Research Papers*.

ACIA (2005). Arctic Climate Impacts Assessment scientific report. *Cambridge University Press*.

Ahrens, C. D. (2009). Meteorology today an introductin to weather, climate, and the environment 9^{th} edition. *Brooks/Cole cengage learning*.

AMAP (2013). Amap assessment 2013: Arctic ocean acidification. *Arctic Monitoring and Assessment Programme (AMAP)*.

Auclair, G. and Tremblay, B. (2018). The role of ocean heat transport in rapid sea ice declines in the community earth system model large ensemble. *Journal of Geophysical Research: Oceans*.

Beszczynska-Moller, A., Woodgate, R. A., Lee, C. M., Melling, H., and Karcher, M. (2011). A synthesis of exchanges through the main oceanic gateways to the arctic ocean. *Oceanography*.

Bonan, G. B., Oleson, K. W., Vertenstein, M., Levis, S., Zeng, X., Dai, Y., Dickinson, R. E., and Yang, Z.-L. (2002). The land surface climatology of the community land model coupled to the ncar community climate model*. *Journal of Climate*.

Briegleb, B. P., Bitz, C. M., Hunke, E. C., Lipscomb, W. H., Holland, M. M., Schramm, J. L., and Moritz, R. E. (2004). Scientific description of the sea ice component in the community climate system model, version three. *NCAR Tech. Note*.

Briegleb, B. P., Danabasoglu, G., and Large, W. G. (2010). An overflow parameterization for the ocean component of the community climate system model. *NCAR technical note*.

Briegleb, B. P. and Light, B. (2007). A delta-eddington multiple scattering parameterization for solar radiation in the sea ice component of the community climate system model. *NCAR Technical Note*.

Cavalieri, D. J., Crawford, J. P., Drinkwater, M. R., Eppler, D. T., Farmer, L. D., Jentz, R. R., and Wackerman, C. C. (1991). Aircraft active and passive microwave validation of sea ice concentration from the defense meteorological satellite program special sensor microwave imager. *Journal of Geophysical Research: Oceans*.

Collins, W. D., Bitz, C. M., Blackmon, M. L., Bonan, G. B., Bretherton, C. S., Carton, J. A., Chang, P., Doney, S. C., Hack, J. J., Henderson, T. B., Kiehl, J. T., and Large, W. G. (2006a). The community climate system model version 3 (ccsm3). *Journal of Climate*.

Collins, W. D., Rasch, P. J., Boville, B. A., Hack, J. J., Mccaa, J. R., Williamson, D. L., Kiehl, J. T., Briegleb, B., Bitz, C., jiann Lin, S., and Zhang, M. (2006b). The formulation and atmospheric simulation of the community atmosphere model version 3 (cam3). *Journal of Climate*.

Collins, W. D., Rasch, P. J., Boville, B. A., Hack, J. J., Mccaa, J. R., Williamson, D. L., Kiehl, J. T., Briegleb, B., Bitz, C., jiann Lin, S., Zhang, M., and Dai, Y. (2004). Description of the ncar community atmosphere model (cam3). *Technical Report NCAR*.

Cuny, J., Rhines, P. B., and Kwok, R. (2005). Davis strait volume, freshwater and heat fluxes. *Deep Sea Research Part I: Oceanographic Research Papers*.

Danabasoglu, G., Bates, S., Briegleb, B. P., Jayne, S., Jochum, M., Large, W. G., Peacock, S., and Yeager, S. (2012). The ccsm4 ocean component. *Journal of Climate*.

Dickinson, R. E., Oleson, K. W., Bonan, G., Hoffman, F., Thornton, P., Vertenstein, M., Yang, Z.-L., and Zeng, X. (2006). The Community Land Model and its climate statistics as a component of the Community Climate System Model. *Journal Of Climate*.

Dmitrenko, I. A., Kirillov, S. A., Tremblay, L. B., Bauch, D., Holemann, J. A., Krumpen, T., Kassens, H., Wegner, C., Heinemann, G., and Schroder, D. (2010). Impact of the arctic ocean atlantic water layer on siberian shelf hydrography. *Journal of Geophysical Research: Oceans*.

Dmitrenko, I. A., Polyakov, I. V., Kirillov, S. A., Timokhov, L. A., Frolov, I. E., Sokolov, V. T., Simmons, H. L., Ivanov, V. V., and Walsh, D. (2008). Toward a warmer arctic ocean:

Spreading of the early 21st century atlantic water warm anomaly along the eurasian basin margins. *Journal of Geophysical Research: Oceans*.

Feltham, D., Untersteiner, N., Wettlaufer, J., and Worster, M. G. (2006). Sea ice is a mushy layer. *Geophys. Res. Lett.*

Ferrari, R., McWilliams, J. C., Canuto, V. M., and Dubovikov, M. (2008). Parameterization of eddy fluxes near oceanic boundaries. *Journal of Climate*.

Ferreira, D. and Marshall, J. (2006). Formulation and implementation of a residual-mean ocean circulation model. *Ocean Modelling*.

Fetterer, F. K., Knowles, W., Meier, W., Savoie, M., and Windnagel, A. K. (2017). 2017, updated daily. sea ice index, version 3. *NSIDC: National Snow and Ice Data Center*.

Fissel, D. B., Marko, J. R., and Melling, H. (2004). Upward looking ice profiler sonar instruments for ice thickness and topography measurements. *MTS/IEEE techno-ocean '04*.

Ford, J. D. (2009). Vulnerability of inuit food systems to food insecurity as a consequence of climate change: a case study from igloolik, nunavut. *Regional Environmental Change*.

Ford, J. D., Smit, B., and Wandel, J. (2006). Vulnerability to climate change in the arctic: A case study from arctic bay, canada. *Global Environmental Change*.

Fox-Kemper, B., Danabasoglu, G., Ferrari, R., Griffies, S. M., Hallberg, R. W., Holland, M. M., Maltrud, M. E., Peacock, S., and Samuels, B. L. (2011). Parameterization of mixed layer eddies. iii: Implementation and impact in global ocean climate simulations. *Ocean Modelling*.

Fox-Kemper, B. and Ferrari, R. (2008). Parameterization of mixed layer eddies. part ii: Prognosis and impact. *Journal of Physical Oceanography*.

Fox-Kemper, B., Ferrari, R., and Hallberg, R. (2008). Parameterization of mixed layer eddies. part i: Theory and diagnosis. *Journal of Physical Oceanography*.

Gent, P. R., Danabasoglu, G., Donner, L. J., Holland, M. M., Hunke, E. C., Jayne, S. R., Lawrence, D. M., Neale, R. B., Rasch, P. J., Vertenstein, M., Worley, P. H., Yang, Z.-L., and Zhang, M. (2011). The community climate system model version 4. *Journal of Climate*.

Gent, P. R. and Mcwilliams, J. C. (1990). Isopycnal mixing in ocean circulation models. *Journal of Physical Oceanography*.

Golden, K. M., Ackley, S. F., and Lytle, V. I. (1998). The percolation phase transition in sea ice. *Science*.

Gorodetskaya, I. V., Tremblay, L.-B., Liepert, B., Cane, M. A., and Cullather, R. I. (2008). The influence of cloud and surface properties on the arctic ocean shortwave radiation budget in coupled models*. *Journal of Climate*.

Haas, C., Lobach, J., Hendricks, S., Rabenstein, L., and Pfaffling, A. (2009). Helicopter-borne measurements of sea ice thickness, using a small and lightweight, digital EM system. *Journal Of Applied Geophysics*.

Holland, M. M., Bailey, D. A., Briegleb, B. P., Light, B., and Hunke, E. (2011). Improved sea ice shortwave radiation physics in ccsm4: The impact of melt ponds and aerosols on arctic sea ice*. *Journal of Climate*.

Holland, M. M. and Bitz, C. M. (2003). Polar amplification of climate change in coupled models. *Climate Dynamics*.

Holland, M. M., Bitz, C. M., and Tremblay, B. (2006a). Future abrupt reductions in the summer Arctic sea ice. *Geophysical Research Letters*.

Holland, M. M., Bitz, C. M., and Tremblay, L.-B. (2006b). Future abrupt reductions in the summer Arctic sea ice. *Geophysical research letters*.

Holland, M. M., Finnis, J., and Serreze, M. C. (2006c). Simulated arctic ocean freshwater budgets in the twentieth and twenty-first centuries. *Journal of Climate*.

Holland, M. M., Serreze, M. C., and Stroeve, J. (2010). The sea ice mass budget of the Arctic and its future change as simulated by coupled climate models. *Climate Dynamics*.

Holliday, N. P., Hughes, S. L., Bacon, S., Beszczynska-Moller, A., Hansen, B., Lavin, A., Loeng, H., Mork, K. A., Osterhus, S., Sherwin, T., and Walczowski, W. (2008). Reversal of the 1960s to 1990s freshening trend in the northeast north atlantic and nordic seas. *Geophysical Research Letters*.

Hunke, E. C. and Dukowicz, J. K. (1997). An elastic-viscous-plastic model for sea ice dynamics. *Journal of Physical Oceanography*.

Hunke, E. C. and Lipscomb, W. H. (2010). Cice: The los alamos sea ice model. documentation and software user's manual. version 4.1. *T-3 Fluid Dynamics Group*.

IPCC (2007). Fourth assessment report of the intergovernmental panel on climate change. *Cambridge University Press*.

IPCC (2013). Fifth assessment report of the intergovernmental panel on climate change. *Cambridge University Press*.

Jahn, A., Sterling, K., Holland, M. M., Kay, J. E., Maslanik, J. A., Bitz, C. M., Bailey, D. A., Stroeve, J., Hunke, E. C., Lipscomb, W. H., and Pollak, D. A. (2012). Late-twentieth-century simulation of arctic sea ice and ocean properties in the ccsm4. *Journal of Climate*.

Jakobsson, M., Mayer, L., Coakley, B., Dowdeswell, J. A., Forbes, S., Fridman, B., Hodnesdal, H., Noormets, R., Pedersen, R., Rebesco, M., Schenke, H. W., Zarayskaya, Y., Accettella, D., Armstrong, A., Anderson, R. M., Bienhoff, P., Camerlenghi, A., Church, I., Edwards, M., Gardner, J. V., Hall, J. K., Hell, B., Hestvik, O., Kristoffersen, Y., Marcussen, C., Mohammad, R., Mosher, D., Nghiem, S. V., Pedrosa, M. T., Travaglini, P. G., and Weatherall, P. (2012). The international bathymetric chart of the arctic ocean (ibcao) version 3.0. *Geophysical Research Letters*.

Jayne, S. R. (2009). The impact of abyssal mixing parameterizations in an ocean general circulation model. *Journal of Physical Oceanography*.

Johannessen, O., Miles, M., Drange, H., Evensen, G., and Lisoeter, K. (2000). Arctic sea ice reduction - implications for the northern sea route. *Northern Sea Route User Conference*.

Johannessen, O. M., Shalina, E. V., and Miles, M. W. (1999). Satellite evidence for an Arctic sea ice cover in transformation. *Science*.

Kalnay, E., Kanamitsu, M., Kistler, R., Collins, W., Deaven, D., Gandin, L., Iredell, M., Saha, S., White, G., Woollen, J., Zhu, Y., Leetmaa, A., Reynolds, R., Chelliah, M., Ebisuzaki, W., Higgins, W., Janowiak, J., Mo, K. C., Ropelewski, C., Wang, J., Jenne, R., and Joseph, D. (1996). The ncep/ncar 40-year reanalysis project. *Bulletin of the American Meteorological Society*.

Kwok, R., Cunningham, G. F., Wensnahan, M., Rigor, I., Zwally, H. J., and Yi, D. (2008). Thinning and volume loss of the arctic ocean sea ice cover. *Journal of Geophysical Research: Oceans*.

Laidre, K., Heide-Jorgensen, M., Nyeland, J., Mosbech, A., and Boertmann, D. (2008). Latitudinal gradients in sea ice and primary production determine arctic seabird colony size in greenland. *Proceedings of the Royal Society B: Biological Sciences*.

Large, W. G., McWilliams, J. C., and Doney, S. C. (1994). Oceanic vertical mixing: A review and a model with a nonlocal boundary layer parameterization. *Reviews of Geophysics*.

Lawrence, D. M., Oleson, K. W., Flanner, M. G., Thornton, P. E., Swenson, S. C., Lawrence, P. J., Zeng, X. B., Yang, Z. L., Levis, S., Sakaguchi, K., Bonan, G., and Slater, A. G. (2011). Parameterization improvements and functional and structural advances in version 4 of the community land model. *Journal of advances in modeling earth systems*.

Lawrence, D. M., Slater, A. G., Tomas, R. A., Holland, M. M., and Deser, C. (2008). Accelerated arctic land warming and permafrost degradation during rapid sea ice loss. *Geophysical Research Letters*.

Laxon, S. W., Giles, K. A., Ridout, A. L., Wingham, D. J., Willatt, R., Cullen, R., Kwok, R., Schweiger, A., Zhang, J., Haas, C., Hendricks, S., Krishfield, R., Kurtz, N., Farrell,

S., and Davidson, M. (2013). CryoSat-2 estimates of Arctic sea ice thickness and volume. *Geophysical Research Letters*.

Lehner, F., Raible, C. C., Hofer, D., and Stocker, T. F. (2012). The freshwater balance of polar regions in transient simulations from 1500 to 2100 ad using a comprehensive coupled climate model. *Climate Dynamics*.

Lindsay, R. and Schweiger, A. (2015). Arctic sea ice thickness loss determined using subsurface, aircraft, and satellite observations. *Cryosphere*.

Lipscomb, W. H., Hunke, E. C., Maslowski, W., and Jakacki, J. (2007). Ridging, strength, and stability in high-resolution sea ice models. *Journal of Geophysical Research: Oceans*.

Markus, T., Cavalieri, D. J., and Comiso, J. (2012). Algorithm theoretical basis document sea ice products. *NASA Goddard Space Flight Center*.

Maykut and Perovich (1987). The role of shortwave radiation in the summer decay of a sea ice cover. *Journal of Geophysical Research - Oceans*.

Maykut, G. and Untersteiner, N. (1971). Some results from a time-dependent thermodynamic model of sea ice. *Geophysical research letters*.

Maykut, G. A. and McPhee, M. G. (1995). Solar heating of the Arctic mixed layer. *Journal of Geophysical Research*, 1002.

McLaughlin, F. A., Carmack, E. C., Williams, W. J., Zimmermann, S., Shimada, K., and Itoh, M. (2009). Joint effects of boundary currents and thermohaline intrusions on the warming of atlantic water in the canada basin, 1993?2007. *Journal of Geophysical Research: Oceans*.

McPhee, M. and Untersteiner, N. (1982). Using sea ice to measure vertical heat-flux in the ocean. *Journal of geophysical research-oceans and atmospheres*.

McPhee, M. G., Kikuchi, T., Morison, J. H., and Stanton, T. P. (2003). Ocean-to-ice heat flux at the north pole environmental observatory. *Geophysical Research Letters*.

Melia, N., Haines, K., and Hawkins, E. (2016). Sea ice decline and 21st century trans-arctic shipping routes. *Geophysical Research Letters*.

Neale, R., Richter, J., Conley, A., Park, S., Lauritzen, P., Gettelman, A., Williamson, D., Rasch, P., Vavrus, S., Taylor, M., Collins, W. D., Zhang, M., and Lin, S. (2010). Descrition of the ncar community atmosphere model (cam 4.0). *NCAR Technical Note*.

Noerdlinger, P. D. and Brower, K. R. (2007). The melting of floating ice raises the ocean level. *Geophysical Journal International*.

Norris, S., Rosentrater, L., and Eid, P. M. (2002). Polar Bears at Risk a WWF Status Report. *WWF International Arctic Programme*.

Notz, D. (2005). Thermodynamic and fluid-dynamical processes in sea ice. *Ph.D. thesis, Univ. of Cambridge, Cambridge, U. K.*

Notz, D. and Grae Worster, M. (2006). A one-dimensional enthalpy model of sea ice. *Annals of Glaciology*.

Notz, D. and Worster, M. G. (2009). Desalination processes of sea ice revisited. *Journal of Geophysical Research: Oceans*.

NSIDC (2013). All about sea ice. thermodynamics: Albedo. *http://nsidc.org/cryosphere/seaice/processes/albedo.html*.

Nummelin, A., Ilicak, M., Li, C., and Smedsrud, L. (2015). Consequences of future increased arctic runoff on arctic ocean stratification, circulation, and sea ice cover. *Journal of Geophysical Research: Oceans*.

Oleson, K. W., Dai, Y., Bonan, G., Bosilovich, M., Dickinson, R., Dirmeyer, P., Hoffman, F., Houser, P., Levis, S., Niu, G.-Y., Thornton, P., Vertenstein, M., Yang, Z.-L., and Zeng, X. (2004). Technical description of the community land model (clm). *Technical Report NCAR*.

Oleson, K. W., Niu, G. Y., Yang, Z. L., Lawrence, D. M., Thornton, P. E., Lawrence, P. J., Stoeckli, R., Dickinson, R. E., Bonan, G. B., Levis, S., Dai, A., and Qian, T. (2008).

Improvements to the Community Land Model and their impact on the hydrological cycle. *Journal Of Geopysical Research-BioGeoSciences.*

Overland, J. E. and Wang, M. (2013). When will the summer Arctic be nearly sea ice free? *Geophysical Research Lettrers.*

Parkinson, C. L. and Comiso, J. C. (2013). On the 2012 record low arctic sea ice cover: Combined impact of preconditioning and an august storm. *Geophysical Research Letters.*

Perovich, D., Tucker, W., and R., K. (1989). Oceanic heat-flux in the Fram strait measured by a drifting buoy. *Geophysical research letters.*

Perovich, D. K. and Elder, B. (2002). Estimates of ocean heat flux at sheba. *Geophysical Research Letters.*

Petrich, C. and Eicken, H. (2010). Growth, structure and properties of sea ice. *Sea Ice.*

Pfirman, S. and Tremblay, B. (2009). Polar bears' last stand. *New scientist.*

Polyakov, I. V., Beszczynska, A., Carmack, E. C., Dmitrenko, I. A., Fahrbach, E., Frolov, I. E., Gerdes, R., Hansen, E., Holfort, J., Ivanov, V. V., Johnson, M. A., Karcher, M., Kauker, F., Morison, J., Orvik, K. A., Schauer, U., Simmons, H. L., Skagseth, O., Sokolov, V. T., Steele, M., Timokhov, L. A., Walsh, D., and Walsh, J. E. (2005). One more step toward a warmer arctic. *Geophysical Research Letters.*

Pressley, A. (2010). Elementary differential geometry. *Springer-Verlag London.*

Rigor, I. G., Wallace, J. M., and Colony, R. L. (2002). Response of sea ice to the arctic oscillation. *Journal of Climate.*

Rudels, B., Marnela, M., and Eriksson, P. (2008). Constraints on estimating mass, heat and freshwater transports in the Arctic Ocean: An Example. *Arctic?Subarctic Ocean Fluxes.*

Schaefer, K., Lantuit, H., Romanovsky, V., and Schuur, E. A. G. (2012). *Policy Implications of Warming Permafrost.* United Nations Environment Programme Special Report.

Schauer, U. and Beszczynska-Moeller, A. (2009). Problems with estimation and interpretation of oceanic heat transport - conceptual remarks for the case of Fram Strait in the Arctic Ocean. *Ocean Science*.

Schauer, U., Beszczynska-Moller, A., Walczowski, W., Fahrbach, E., Piechura, J., and Hansen, E. (2008). ariation of Measured Heat Flow Through the Fram Strait Between 1997 and 2006. *Arctic?Subarctic Ocean Fluxes.*

Schweiger, A., Lindsay, R., Zhang, J., Steele, M., Stern, H., and Kwok, R. (2011). Uncertainty in modeled Arctic sea ice volume. *Journal of Geophysical Research - Oceans*.

Serreze, M. C., Barrett, A. P., Slater, A. G., Steele, M., Zhang, J., and Trenberth, K. E. (2007). The large-scale energy budget of the arctic. *Journal of Geophysical Research: Atmospheres*.

Serreze, M. C. and Barry, R. G. (2011). Processes and impacts of arctic amplification: A research synthesis. *Global and Planetary Change*.

Serreze, M. C., Maslanik, J. A., Scambos, T. A., Fetterer, F., Stroeve, J., Knowles, K., Fowler, C., Drobot, S., Barry, R. G., and Haran, T. M. (2003). A record minimum arctic sea ice extent and area in 2002. *Geophysical Research Letters*.

Shirtcliffe, T. G. L., Huppert, H. E., and Worster, M. G. (1991). Measurement of the solid fraction in the crystallization of a binary melt. *Journal of Crystal Growth*.

Shupe, M. D. and Intrieri, J. M. (2004). Cloud radiative forcing of the arctic surface: The influence of cloud properties, surface albedo, and solar zenith angle. *Journal of Climate*.

Skagseth, A., Furevik, T., Ingvaldsen, R., Loeng, H., Mork, K., Orvik, K., and Ozhigin, V. (2008). Volume and heat transports to the arctic ocean via the norwegian and barents seas. *Arctic-Subarctic Ocean Fluxes*.

Smedsrud, L., Ingvaldsen, R., Nilsen, J. E., and Skagseth, A. (2010). Heat in the barents sea: Transport, storage, and surface fluxes. *Ocean Science*.

Smith, R., Jones, P., Briegleb, B., Bryan, F., Danabasoglu, G., Dennis, J., Dukowicz, J., Eden, C., Fox-Kemper, B., Gent, P., Hecht, M., Jayne, S., Jochum, M., Large, W. G., Lindsay, K., Maltrud, M., Norton, N., Peacock, S., Vertenstein, M., and Yeager, S. (2010). The parallel ocean program (pop) reference manual. *Los Alamos National Laboratory technical note*.

Smith, R. D. and Gent, P. R. (2004a). Anisotropic gent–mcwilliams parameterization for ocean models. *Journal of Physical Oceanography*.

Smith, R. D. and Gent, P. R. (2004b). Reference manual for the parallel ocean program (pop) ocean component of the community climate system model (ccsm2.0 and 3.0). *LAUR-02-2484, Los Alamos Natl. Lab., Los Alamos, N. M.*

Smithson, P., Addison, K., and Atkinson, K. (2002). Fundamentals of the physical environment. *Psychology Press*.

Steele, M. (1992). Sea ice melting and floe geometry in a simple ice-ocean model. *Journal of Geophysical Research - Oceans*.

Steele, M. and Boyd, T. (1998). Retreat of the cold halocline layer in the arctic ocean. *Journal of Geophysical Research: Oceans*.

Stirling, I. and Derocher, A. E. (2012). Effects of climate warming on polar bears: a review of the evidence. *Global change biology*.

Stoeckli, R., Lawrence, D. M., Niu, G. Y., Oleson, K. W., Thornton, P. E., Yang, Z. L., Bonan, G. B., Denning, A. S., and Running, S. W. (2008). Use of FLUXNET in the community land model development. *Journal Of Geopysical Research-BioGeoSciences*.

Stroeve, J., Holland, M. M., Meier, W., Scambos, T., and Serreze, M. (2007). Arctic sea ice decline: Faster than forecast. *Geophysical Research Letters*.

Stroeve, J., Serreze, M., Drobot, S., Gearheard, S., Holland, M., Maslanik, J., Meier, W., and Scambos, T. (2008). Arctic sea ice extent plummets in 2007. *Eos, Transactions American Geophysical Union*.

Stroeve, J. C., Kattsov, V., Barrett, A., Serreze, M., Pavlova, T., Holland, M., and Meier, W. N. (2012). Trends in arctic sea ice extent from cmip5, cmip3 and observations. *Geophysical Research Letters.*

TheCircle (2012). Ice whales - where are they going? *The Circle, WWF magazine.*

Thomas, D. N. (2001, 20010, 2016). Sea Ice, first, second and third editions. *John Wiley & Sons, Lt.*

Thorndike, A. S., Rothrock, D. A., Maykut, G. A., and Colony, R. (1975). The thickness distribution of sea ice. *Journal of Geophysical Research.*

Timmermans, M.-L., Toole, J., Krishfield, R., and Winsor, P. (2008). Ice-tethered profiler observations of the doublediffusive ice-tethered profiler observations of the double-diffusive staircase in the canada basin thermocline. *J. Geophys. Res.*

Vallis, G. (2006). Atmospheric and oceanic fluid dynamics fundamentals and large-scale circulations. *Cambridge University Press.*

Vaughan, D. G., Comiso, J., Allison, I., Carrasco, J., Kaser, G., Kwok, R., Holland, D., and al. (2013). Climate change 2013: The physical science basis. contribution of working group i to the fifth assessment report of the intergovernmental panel on climate change, observations: Cryosphere. *Cambridge University Press.*

Wang, M. and Overland, J. E. (2012). A sea ice free summer Arctic within 30 years: An update from CMIP5 models. *Geophysical research letters.*

Wassmann, P., Duarte, C. M., Agusti, S., and Sejr, M. K. (2011). Footprints of climate change in the arctic marine ecosystem. *Global Change Biology.*

Wijffels, S. E. (2001). Chapter 6.2 ocean transport of fresh water. *Ocean Circulation and Climate.*

Williams, G. P. (1972). Friction term formulation and convective instability in a shallow atmosphere. *Journal of the Atmospheric Sciences.*

Winton, M. (2011). Do climate models underestimate the sensitivity of northern hemisphere sea ice cover? *Journal of Climate*.

Woodgate, R. A., Weingartner, T., and Lindsay, R. (2010). The 2007 bering strait oceanic heat flux and anomalous arctic sea ice retreat. *Geophysical Research Letters*.

Zhang, J. and Rothrock, D. A. (2003). Modeling global sea ice with a thickness and enthalpy distribution model in generalized curvilinear coordinates. *Monthly Weather Review*.

Zwally, . J., Schutz, B., Abdalati, W., Abshire, J., Bentley, C., Brenner, A., Bufton, J., Dezio, J., Hancock, D., Harding, D., Herring, T., Minster, B., Quinn, K., Palm, S., Spinhirne, J., and Thomas, R. (2002). ICESat's laser measurements of polar ice, atmosphere, ocean, and land. *Journal Of Geodynamics*.